POLITECNICO DI MILANO

Facoltà di Ingegneria dei Sistemi

Corso di Laurea in Ingegneria Fisica

Feasibility, Development and Characterization of a Photoacoustic Microscopy System for Biomedical Applications

Relatore: Chiar.mo Prof. Rinaldo CUBEDDU

Tesi di Laurea Specialistica di:

Luca FIERAMONTI

Matr. 733979

Anno Accademico 2009 - 2010

"Multa non quia difficilia sunt non audemus, sed quia non audemus sunt difficilia."

Lucius Annaeus Seneca

POLITECNICO DI MILANO - LUND UNIVERSITY

Abstract

II Faculty of Engineering
Department of Physics

Master of Science in Physics Engineering

by Luca Fieramonti

The present thesis is about the development and the characterization of a photoacoustic microscopy system to be used in biomedical applications, like cancer cells detection or imaging of superficial blood vessels.

Photoacoustic microscopy is an imaging technique which combines strong optical contrast and high ultrasonic resolution in a single modality. The need of making pictures of tumors deeply embedded into tissues, with a high spatial resolution, justifies the interest of the research community worldwide toward photoacoustic imaging technologies, which has considerably grown in the last decade.

In photoacoustic imaging modalities, light waves are converted into acoustic ones thanks to the absorption of the optical radiation by the target and its following conversion into heat. This process is called *photoacoustic effect*.

In the first part of this thesis work, the principal photoacoustic techniques, their functioning principles and their state-of-the-art features are described. After this, the theory that rules photon migration in turbid biological media and photoacoustic wave generation, propagation and revelation is presented.

The second part of the thesis, instead, is about the work carried out at Lund University in Sweden, which aims to develop a photoacoustic microscopy system by using a standard commercial ultrasonic scanner (Ultrasonix Sonix RP), equipped with a normal linear transducer (L14-5/38). This scanner has a very high potential of adaptability and programmability. The focus of the project is to maximize penetration depth, even if, in this case, resolution cannot be better than several hundreds of microns.

Finally, the principal characteristics of the developed system are described, evaluated and compared to other photoacoustic imaging systems.

Abstract: Versione Italiana

Questo lavoro di tesi riguarda lo sviluppo e la caratterizzazione di un sistema di microscopia fotoacustica per applicazioni in campo biomedicale, come, ad esempio, rivelazione di cellule tumorali o mappatura dei vasi sanguigni superficiali.

La microscopia fotoacustica è una tecnica di realizzazione di immagini che combina, in un'unica modalità, un forte contrasto, tipico delle tecniche ottiche, con un'alta risoluzione, tipica delle tecniche ad ultrasuoni. La necessità di realizzare immagini precise di tumori, situati in profondità nei tessuti, giustifica l'interesse della comunità scientifica mondiale per le tecniche fotoacustiche. Negli ultimi dieci anni, infatti, questo interesse è cresciuto notevolmente.

Nelle tecniche fotoacustiche, la luce laser, iniettata nei tessuti, viene trasformata in onde acustiche grazie all'assorbimento e alla conversione in calore della radiazione elettromagnetica da parte dell'oggetto da individuare. Tale processo è chiamato *effetto fotoacustico*.

Nella prima parte di questo lavoro di tesi, sono descritte le principali tecniche fotoacustiche, il loro funzionamento e il loro stato dell'arte. Segue poi la teoria che modellizza il trasporto dei fotoni all'interno di mezzi torbidi. Viene descritta, infine, la generazione, la propagazione e la rivelazione delle onde fotoacustiche.

La seconda parte della tesi, invece, riguarda il lavoro effettuato presso l'Università di Lund, in Svezia. La sua finalità consiste nello sviluppare un sistema di microscopia fotoacustica tramite l'uso di una macchina per la rivelazione di ultrasuoni disponibile commercialmente (Ultrasonix Sonix RP), equipaggiata con un normale trasduttore ultrasonico lineare (L14-5/38). La macchina utilizzata nel progetto, sebbene normalmente impiegata nella realizzazione di immagini ecografiche, può essere modificata opportunamente per ottenere immagini fotoacustiche, grazie alle sue elevate capacità di adattabilità e programmabilità.

In questo progetto di tesi, ci si è focalizzati principalmente sulla massimizzazione della profondità di penetrazione della tecnica, a scapito della risoluzione spaziale, che, in questo caso, non può scendere al di sotto di alcune centinaia di micron.

Il sistema sviluppato, infine, viene caratterizzato grazie all'uso di sistemi modello, che simulano i tessuti biologici, e le sue caratteristiche sono confrontate con quelle di altri sistemi fotoacustici per la realizzazione di immagini.

Contents

List of Figures

List of Tables

Abbreviations

2PM	**T**wo-**P**hoton **M**icroscopy
ANSI	**A**merican **N**ational **S**tandards **I**nstitute
CFM	**C**on**F**ocal **M**icroscopy
CPU	**C**entral **P**rocessing **U**nit
CT	**C**omputed **T**omography
DOT	**D**iffuse **O**ptical **T**omography
FWHM	**F**ull **W**idth at **H**alf **M**aximum
GUI	**G**raphical **U**ser **I**nterface
IR	**I**nfra**R**ed
NA	**N**umerical **A**perture
OCT	**O**ptical **C**oherence **T**omography
OD	**O**ptical **D**ensity
PAI	**P**hoto**A**coustic **I**maging
PAM	**P**hoto**A**coustic **M**icroscopy
PAT	**P**hoto**A**coustic **T**omography
PDF	**P**robability **D**ensity **F**unction
PDT	**P**hoto**D**ynamic **T**herapy
PRF	**P**ulse **R**epetition **F**requency
RESOLFT	**RE**versible **S**aturable **O**ptica**L** **F**luorescence **T**ransitions
RF	**R**adio **F**requency
RTE	**R**adiative **T**ransport **E**quation
SDK	**S**oftware **D**evelopment **K**it
SNR	**S**ignal to **N**oise **R**atio
TAT	**T**hermo**A**coustic **T**omography
US	**U**ltra**S**onography

To Stefania and my family

Part I

Chapter 1

Photoacoustic Imaging Techniques

1.1 Introduction

PhotoAcoustic Imaging (PAI) is a general name that refers to a collection of non-invasive imaging techniques, which are used to get pictures of biological tissues and their internal structures. They are based on the photoacoustic effect that converts optical energy into acoustic energy. This phenomenon appears whenever a tissue is exposed to a short-pulsed laser beam in the nanosecond time scale. As a consequence, some of the light is absorbed and partly converted into heat. Thanks to the thermoelastic expansion, this heat is then converted to mechanical stress. The pressure rise travels in the tissue like a broadband ultrasonic wave, with a frequency content of several tens of MHz [1]. This wave is generally called *photoacoustic wave*. If this wave is detected by an ultrasonic transducer, it is possible to use the information that it provides to form an image of the photoacoustic source.

PAI is a recent branch developed in the field of biological and medical imaging. During the last decade it has gained more and more interest from researchers worldwide [2], because of its unique features, like high spatial resolution combined with high penetration depth and high selectivity. Note also that it poses no hazard for health, because it uses only non ionizing radiation[1]. However, despite the huge improvements during the last couple of years, which consisted mainly in the achievement of very high frame rates for real time applications and the realization of images with very good resolutions, it is still

[1]It is important to care about the value of laser power that must respect the ANSI maximum exposure limit for human tissues. Moreover, generated photoacoustic waves also produce a mechanical stress to biological media. ANSI standards for radio frequency signals in tissues exist too [3].

in the pre-clinical phase of experimentation. Only a few papers have been published about clinical applications, and this happened during the same months in which this thesis work has been carried out [4].

To understand why PAI techniques are so promising, it is necessary to identify which problems one has to face while doing ballistic imaging[2] of tissues. These problems are consequences of diffraction and diffusion, that are the principal phenomena that spoil the image quality in this kind of techniques.

Diffraction is a wave phenomenon that limits the lateral spatial resolution of ballistic imaging techniques. Examples of these techniques are *ConFocal Microscopy* (CFM), *Two-Photon Microscopy* (2PM), and *Optical Coherence Tomography* (OCT). The scientific community is making a big effort to overcome this limit with the so called *super-resolution* techniques, such as *REversible Saturable OpticaL Fluorescence Transitions* (RESOLFT) and stochastic imaging modalities.

Diffusion, instead, is due to the scattering property of tissues, that is the ability of changing the propagation direction of photons without changing their energy. This phenomenon, in particular isotropic diffusion, limits the penetration of ballistic photons, which means that the majority of ballistic techniques cannot perform measurements beyond the *soft limit*. The soft limit is typically placed at a depth of 1 mm, that corresponds to one transport mean free path[3]. After this limit, the isotropic scattering prevails on the anisotropic scattering, which starts after one mean free path[4] (0.1 mm). In fact, it is still possible to make images using the scattered photons, but only with a poor spatial resolution [5]. One common technique of this kind is the *Diffuse Optical Tomography* (DOT). Imaging modalities that try to overcome this problem, like PAI techniques, are defined *super-depth* techniques.

Unlike optical techniques, *UltraSonography* (US) is able to give a good resolution at excellent depths. As a matter of fact, ultrasonic scattering is from two to three orders of magnitude weaker than the optical one. However, US detects only mechanical properties of tissues and is characterized by a weak contrast for early-stage tumors [6]. Since PAI techniques aim to localize precisely tumors deep inside the body, the contrast in detecting tumoral tissue is a very important parameter to be considered. This contrast comes from the different spectroscopic features that tumors have compared to normal tissue. That is why US is not able to detect them, because the mechanical properties are similar.

[2]The term *ballistic imaging* refers to the recollection of photons, among those injected in the tissue, that are not strongly affected by the scattering. These photons bring the maximum information about tissues properties.

[3]The transport mean free path is defined as $l'_t = 1/\mu'_t$, where $\mu'_t = \mu_a + \mu'_s$is the transport interaction coefficient.

[4]The mean free path is defined as $l_t = 1/\mu_t$, where $\mu_t = \mu_a + \mu_s$is the extinction coefficient.

PAI tries to solve all the problems listed above by combining the high contrast of optical absorption with the great spatial resolution of ultrasound for deep imaging in the optical quasi-diffusive or diffusive regime (3-30 mm). As a matter of fact, the contrast in PAI is given by the quantity of absorbed light, but the resolution comes from the ultrasonic detection.

Being speckle free is another advantage of PAI. Speckles are displayed like random intensity patterns produced by the interferences of a set of wavefronts. Indeed, some imaging techniques, like OCT and US, are strongly affected by this kind of artifacts, because they are based on the backscattering of a unique wavefront. As the reflecting surface is not perfectly flat, a lot of waves with different phases are generated. In PAI, initial pressure rises are positive from all absorbers at the same time. Consequently, prominent boundaries always build up in photoacoustic images and suppress the interior fluctuation [7].

In PAI, though, it results that both resolution and penetration depth are scalable with ultrasonic frequency. This means that, if we reveal higher ultrasonic frequencies of the photoacoustic signal, spatial resolution gets better, because the correspondent value decreases. At the same time, the maximum penetration depth decreases too, because higher ultrasonic frequencies are more attenuated than lower ones. As a result, there is a trade off between resolution and penetration depth. Note that this holds true only inside the tissue area that is actually reached by sufficient light power to generate photoacoustic waves. Its size can vary accordingly to the used wavelength of radiation.

By the way, supposing that we are using light in the near infrared part of the electromagnetic spectrum, which can well penetrate in tissues, it is usually verified that [8]:

$$Relative\ Spatial\ Resolution = \frac{Penetration\ Depth}{Resolution} > 100. \tag{1.1}$$

This is the definition of high-resolution imaging modalities and it means that PAI can be considered one of them. It has been demonstrated that a microscopy system based on the PAI concept can reach a relative spatial resolution of about 200 [8].

Table 1.1 presents a comparison of the aforementioned imaging techniques, summarizing their features. PAI, as shown, is the only one without evident weaknesses for the considered parameters. However, it usually lacks of structural information and must be used in combination with US [9]. Moreover, in order to obtain the features shown in Table 1.1 for PAI, it is assumed that the used wavelength is in the near IR spectrum, otherwise the penetration depth is strongly limited.

Technique name	Imaging contrast	Imaging depth	Axial resolution	Speckle artifacts	Scattering coefficient
CFM/2PM	Excellent	Poor ($\sim 0.5\ mm$)	Excellent ($\sim 1-2\ \mu m$)	None	Strong ($\sim 10\ mm^{-1}$)
OCT	Good	Poor ($\sim 1\ mm$)	Excellent ($\sim 10\ \mu m$)	Strong	Strong ($\sim 10\ mm^{-1}$)
DOT	Excellent	Good ($\sim 50\ mm$)	Poor ($\sim 5\ mm$)	None	Strong ($\sim 10\ mm^{-1}$)
US	Poor for early cancers	Excellent and scalable ($\sim 60\ mm$)	Excellent and scalable ($\sim 0.3\ mm$)	Strong	Weak ($\sim 0.03\ mm^{-1}$)
PAI	Excellent	Good and scalable ($\sim 3-50\ mm$)	Excellent and scalable ($\sim 15-250\ \mu m$)	None	Strong for light, weak for the photoacoustic wave

TABLE 1.1: Performances comparison of different common biomedical imaging techniques. Data for US refer to a 5 MHz working frequency.

It is possible to understand, from this overview, that PAI has all the prerequisites to become an important technique in the field of early tumor diagnostics for the human body, if complementarily used to the imaging modalities that are already developed. For this reason, the Biophotonics Group at the Division of Atomic Physics[5], in association with the Ultrasound Group at the Department of Electrical Measurements[6], both in Lund University, started a project about PAI in March 2010. They are big research groups: the former develops new biomedical uses of lasers, while the latter works on ultrasound properties and on their large applications.

The project is about the feasibility of a PAI system using a common commercial ultrasonic scanner for the detection of photoacoustic waves. In particular, the purpose is to develop and characterize a system to perform photoacoustic microscopy.

The present thesis is formed by a first theoretical part, which contains an overview of PAI techniques and the theory that describes the generation, propagation and detection of photoacoustic waves. The second part is an experimental one and describes the work done from the very beginning of the mentioned project.

[5]The visiting address of the Physics Department of Lund University is: Professorsgatan 1, 223 63 Lund, Sweden. The website is: www.atomic.physics.lu.se.

[6]The visiting address of the Electrical Measurements Department of Lund University is: Ole Römers väg 3, 223 63 Lund, Sweden. The website is: www.elmat.lth.se.

1.2 History and Description of Photoacoustic Imaging Techniques

The photoacoustic effect was observed, for the first time, in 1880 by Alexander Graham Bell[7], the scientist who is credited with the invention of the first practical telephone. He was trying to create the *photophone*, a device supposed to convert sound into an intensity modulation of sun light, then to propagate this light in free space, and eventually reconvert it again into audible sounds. He hoped to replace the telephone with this wireless device [10]. Figure 1.1 shows a diagram of Bell's photophone.

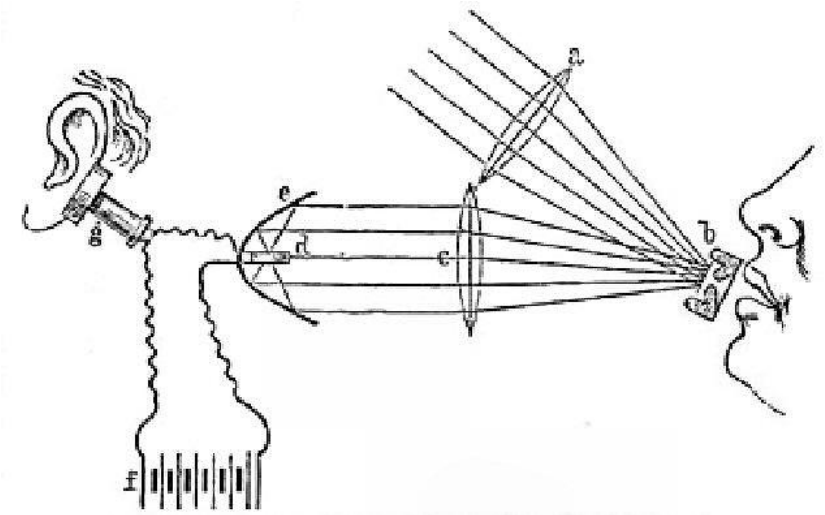

FIGURE 1.1: Diagram of a photophone with an electrical receiver. The picture comes from one of Bell's 1880 papers.

In the beginning, Bell tried to exploit the properties of selenium, an element that decreases its electrical resistance when exposed to light. If a piece of selenium is illuminated by an intermittent light while an electrical current flows through it, the current is modulated accordingly to the light variation. If this variable current drives a speaker, sounds are produced.

He soon discovered, however, that it was not necessary to use an electrical receiver to produce sounds. Providing that the receiver was a thin diaphragm, it was possible to create acoustic waves just by focusing, through a lens, the intensity-modulated light on the material. The difference between how Bell used the photoacoustic effect and how it is used by PAI is that Bell wanted to create audible sounds (with frequency from 20 Hz to 20 kHz), while PAI needs to generate ultrasonic waves (with frequency above 20 kHz) to increase the spatial resolution of imaging techniques.

[7]Alexander G. Bell was born on March 3, 1847 in Edinburgh, UK, and died for diabetes on August 2, 1922 in Beinn Bhreagh, Canada, at age 75.

In his article "On the production and reproduction of sound by light", published in 1880, he states that:

> It is a well known fact that the molecular disturbance, produced in a mass of iron by the magnetizing influence of an intermittent electrical current, can be observed as sound by placing the ear in close contact with the iron, and it occurred to us that the molecular disturbance produced in crystalline selenium by the action of an intermittent beam of light should be audible in a similar manner without the aid of a telephone or battery. [...]
>
> On the whole, we feel warranted in announcing as our conclusions that *sounds can be produced by the action of a variable light from substances of all kinds when in the form of thin diaphragms.* The reason why thin diaphragms of the various materials are more effective than masses of the same substances, appears to be that the molecular disturbance produced by light is chiefly a surface action, and that the vibration has to be transmitted through the mass of the substance in order to affect the ear[8].

Despite Bell's wishes, the photophone never gained success among the population because of its limitations and problems. Sun light is not always present and light is strongly attenuated while propagating in the atmosphere. A more reliable light source was needed, but lasers were not invented yet at that time. It is no coincidence that PAI was invented only after the advent of ultrasonic transducers, computers, and, most of all, lasers. As a matter of fact, they are the easiest way to control light delivery.

Pulsed laser light, indeed, is used in the majority of PAI techniques in order to illuminate the tissue. The succession of phenomena that occur after light exposure is shown in the following list:

1. *Light absorption* : The molecules, that absorb light, start vibrating.
2. *Temperature rise*: The vibration locally increases the temperature.
3. *Thermoelastic expansion*: Because of the thermoelastic effect, the heated area expands.
4. *Acoustic emission*: The surrounding tissue is correspondingly compressed and the pressure variation propagates away from the source.

[8] A.G. Bell, "On the production and reproduction of sound by light", *American Journal of Science*, Vol. 20, No. 118, 305-324, (1880).

As far as the photoacoustic wave leaves the source, we have to deal with a 3D ultrasonic object. If we measure the signal with ultrasonic transducers, it is possible to reconstruct the source position with different methods. The process is conceptually very similar to the triangulation of a thunder position [5].

Measuring the time delay between the lightning and the thunder, we can say that the thunder took place on the surface of a sphere, centred in the observer's position and with a radius equal to the time delay multiplied by the speed of sound. If three such measurements are available from three distinct observers, it is possible to determine exactly the place in which the lightning appeared, as shown in Figure 1.2.

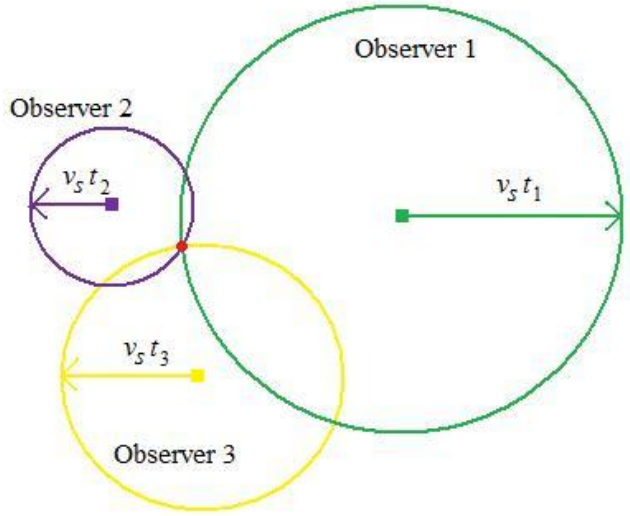

FIGURE 1.2: Triangulation of the position of an acoustic source by three different observers. v_s is the speed of sound. t_1, t_2, t_3 are the time delays that each observer measures from his position, respectively.

The actual reconstruction algorithm depends on which PAI modality is used and which kind of information we want to recover about the source. There are three main PAI techniques that are principally under research at the moment: *PhotoAcoustic Tomography* (PAT), *PhotoAcoustic Microscopy* (PAM), and *ThermoAcoustic Tomography* (TAT). In the following sections, these techniques will be presented and a description of how they work and their state-of-the-art will be given.

1.2.1 Photoacoustic Tomography

PAT is able to reconstruct the initial pressure distribution and, as a result, the distribution of internal absorbing objects, by measuring the photoacoustic signals at the tissue surface with as many unfocused ultrasonic transducers as possible. Detectors should

be ideally point transducers. The reconstruction process is done by a computer in the post-processing phase, through a back-projection algorithm. The detection surface should enclose the studied photoacoustic source.

In general, different measurement geometries need different reconstruction algorithms. The canonical geometries usually considered are planar, cylindrical, and spherical measuring surfaces. In all algorithms, acoustic properties of tissues are often assumed to be homogeneous and the speed of sound[9] v_s is considered constant at 1500 m/s.

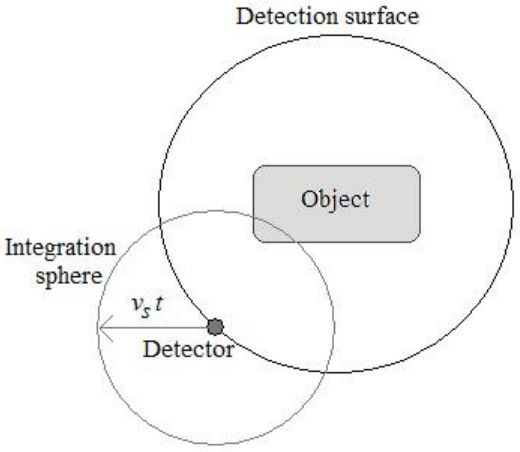

FIGURE 1.3: Sketch about tomographic image reconstruction. v_s is the speed of sound. t is the time delay between the generation of the photoacoustic wave and the measurement.

After a time t, the ultrasonic transducer measures the integral of the initial pressure distribution along a sphere centred in the detector, with a radius of $v_s \cdot t$. See Figure 1.3 in order to have a graphical sketch of the situation. This measurement corresponds to the spherical Radon transform, which is very different from the actual Radon transform. The latter one is used in *Computed Tomography* (CT) or other ballistic imaging techniques and it corresponds to the attenuation coefficient integration along the straight propagation direction.

At first, scientists had to invert this integral in every single detection geometry in order to calculate the initial pressure distribution [2]. This inversion is not trivial. Luckily, it results that a universal reconstruction formula exists for the three canonical geometries [11].

[9] 1500 m/s is the average value for the speed of sound in soft tissue.

The initial pressure, at time $t = 0$, can be calculated as:

$$p_0(\vec{r}) = \frac{2}{\Omega_0} \int \left[p(\vec{r}_0, t) - t \frac{\partial p(\vec{r}_0, t)}{\partial t} \right]_{t=\frac{|\vec{r}-\vec{r}_0|}{v_s}} d\Omega_0 \tag{1.2}$$

where $\vec{r}_0$ is the detector position, and Ω_0 is the solid angle subtended by the whole detection surface with respect to the reconstruction point inside of it. It is 2π for planar geometry and 4π for cylindrical and spherical geometries.

The first term in brackets, $p(\vec{r}_0, t)$, is the pressure measured at the detector position $\vec{r}_0$ as a function of time. If a proper delay is applied, accordingly to the distance between the source and the detector, it is possible to recover the source position. This is equivalent to the process of *beamforming* that will be explained more in details in Section 3.5. In addition, if we also include the high-frequency components in the integral, it is possible to obtain the exact solution for the pressure at time $t = 0$. The high-frequency components are represented by the first derivative of pressure over time. It is equal to a pure ramp filter in the frequency domain, which depresses the low-frequency signal [11].

When the initial pressure distribution is known, it is easy to make an image of the photoacoustic source, both in 2D or 3D. The stronger the signal reconstructed, the bigger the concentration of absorbing molecules. Moreover, by using different wavelengths, it is possible to see the spatial distribution of different chromophores. For example, we can image Oxy- and Deoxy-hemoglobin and we can calculate concentrations and oxygen saturation.

Thanks to these capabilities, it is possible to detect tumors through hypoxia and increased vascularization (angiogenesis), or to perform functional imaging to visualize brain activation. At the moment, this has been done only in rats, with a resolution of 60 μm for the structural information. It is also possible to accomplish molecular imaging, using a dye to label particular targets, like cancer cells. It has been demonstrated that, relaxing the resolution to 312 μm, the sensitivity becomes very high and could be of 4 $fmol/voxel$[10], which corresponds to 40 nM [12].

High temporal resolution in PAT is needed if one wants to survey neuro-vascular responses. At the state-of-the-art it is of 1 $frame/s$, but it is not high enough for the mentioned purpose yet [13].

[10] A voxel is a three-dimensional pixel.

1.2.2 Photoacoustic Microscopy

Unlike PAT, which uses powerful mathematics to reconstruct the image, PAM needs only physics to detect the features of the photoacoustic source. As a matter of fact, PAM employs an acoustic lens to project, on the image plane, the already focused signals, that can be immediately used to form the image using a normal ultrasonic transducer. Usually, the ultrasonic lens is a physical one, made by a material properly shaped in order to focus ultrasonic waves.

Ultrasonic detection with an acoustic lens is similar to image reconstruction in PAT with a limited detection surface. The lateral resolution is determined by the focal diameter of the ultrasonic transducer at the central frequency. The axial resolution, however, is inversely proportional to the ultrasonic transducer bandwidth. As a consequence, if one is interested in having a high spatial resolution, it is necessary to give the transducer a high central frequency, a large *Numerical Aperture*[11] (NA), and a wide bandwidth [5].

If a linear transducer array is used, though, it is possible to reconstruct the image with a synthetic aperture. In this case no physical lens is required, but the signals are electronically delayed for each transducer element. This is the already mentioned *beamforming* process, explained in Section 3.5, also called *delay-and-sum* algorithm.

If we have only a point ultrasonic detector, the photoacoustic wave is recorded like a spike in the *Radio Frequency* (RF) signal. Knowing the speed of sound, it is possible to calculate at which depth the wave was generated. As a result, we obtain only a one-dimensional reconstructed vertical line, which is called *A-scan*. The lateral resolution depends on the focus position. If the transducer is then scanned on the tissue surface along a line, a *B-scan* is obtained. This is a two-dimensional reconstructed slice of the studied tissue. If more B-scan images are collected, it is possible to make 3D pictures of the target.

Zhang et al. have recently implemented a system called dark-field confocal PAM [14]. An overview of this system is presented in Figure 1.4. In this setup, 6.5 ns laser pulses are sent, through optical fibers, to a conical lens in order to give the beam a doughnut shape. A 560 nm wavelength is usually used for hemoglobin imaging. The ring-shape of the beam is supposed to avoid strong photoacoustic signals from the tissue surface. As a matter of fact, the ultrasonic transducer is placed exactly above the dark spot of the illumination pattern.

[11] Numerical aperture is a dimensionless parameter for lenses, which characterizes the angle range over which the system accepts (or emits) acoustic waves or light. It is defined, in acoustics, as NA$= \sin\theta$, where θ is the semi-aperture angle of the lens subtended at the focus. Note that NA$\approx 1/(2 \cdot f\#)$, where $f\#$ is the f-number of the detector.

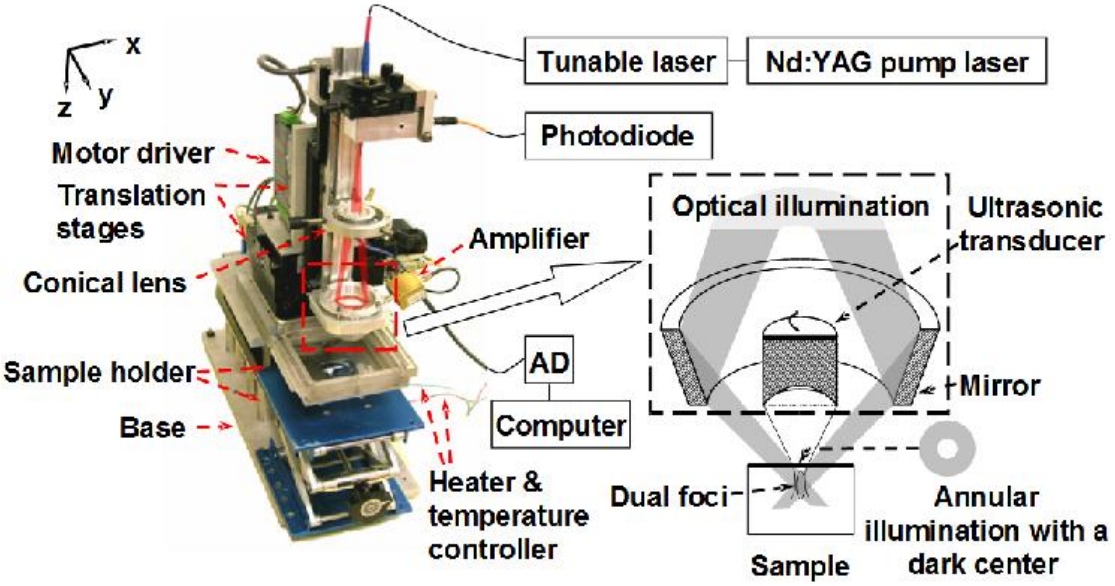

FIGURE 1.4: Dark-field confocal PAM system. All the components are shown in the figure. Note the ring-shaped illumination pattern.

The studied sample is placed under a water tank with a bottom constituted by a thin polymeric film, that is transparent for acoustic waves. A coupling gel is usually placed between the tissue and the film. The central frequency of the transducer is quite high, because it is of 50 MHz. In addition, it has a NA of 0.44, and a nominal bandwidth of 35 MHz.

This system is characterized by an axial resolution of $\sim$15 μm and a lateral resolution of $\sim$45 μm. The setup has been demonstrated to reach about a 3 mm depth in biological tissue [15].

With this system it is possible to see hemodynamics in small animals in vivo. It is like pulsed oxymetry, but here we have resolution on every single vessel. It is also possible to reveal melanomas. The contrast[12], with respect to normal surrounding tissue, has been demonstrated to be $\sim$10 for blood and $\sim$70 for melanomas [15].

PAM is useful for molecular imaging too. It is possible to use nanoshells that absorb light in the near-infrared range, properly targeted to stick to tumors. PAM also allows us to see the cancer evolution during *PhotoDynamic Therapy* (PDT).

To speed up the measure, one can use an array of detectors. A rate of 50 $frames/s$ has been shown, using a laser *Pulse Repetition Frequency* (PRF) of 1 kHz. With appropriate changes to the setup, researchers have reached a rate of 249 B-scan/s in order to make 3D images with an acceptable measuring rate of 0.5 Hz [16]. In this case, however,

[12]The contrast is defined as $C = \frac{I-I_b}{I_b}$, where I is the signal intensity and I_b is the background intensity.

the PRF is of 1.5 kHz. Note that, in both cases, the PRF is too high regarding the safety limit for human applications[13]. As a result, these solutions can be used only for experiments on animals.

If we want to increase the penetration depth, it is necessary to reduce the transducer central frequency. In order to reach a depth of 30 mm, researchers have used a detector centred to 5 MHz. Note that, as a consequence, resolution gets worse. They have obtained an axial resolution of 144 μm and a lateral one of 560 μm [17].

1.2.3 Thermoacoustic Tomography

The last PAI modality that will be presented is TAT. This technique allows a deeper penetration depth of tissues. To achieve this result, it is necessary to change the illuminating wavelength, because *InfraRed* (IR) light can penetrate no more than 3-5 cm in biological media. As a result, a RF (100-1000 MHz) or a microwave (1-100 GHz) source is employed and it permits to reach very big penetration depths.

RF absorption in tissues is most affected by two properties: conductivity and dipolar relaxation of water molecules. Under the RF excitation, these molecules start to spin. A small increase in concentration of ionic water in tissue can produce a large increase in RF absorption.

There are evidences that the ionic water content in tumors is increased due to a more dense concentration of blood and proteins. Such increases are the result of angiogenesis within rapidly growing tumors. The use of RF sources, with frequencies in the vicinity of 400-500 MHz, is particularly suitable for measuring these effects in the breast [18].

As a result, TAT could be used beside, or even replace, the x-ray mammography, usually used to detect breast cancer.

It has been demonstrated that TAT can reach a penetration depth in fat of about 9 cm, providing that 3 GHz microwave pulses, with a duration of 500 ns and an energy of 5 mJ, are sent through the studied tissue [19].

1.3 Applications of PAI

The principal feature, that makes PAI so interesting, is its scalability. This means that it is possible to make images with the same contrast agents on very different scales,

[13] Usually, if the laser hits the tissue for more than 10 s, the PRF limit for human applications is around 30 Hz [8].

from cells and organelles to entire organs. The ability of imaging biological systems at multiple length scales is important, because it could accelerate the translation of microscopic laboratory discoveries to macroscopic clinical practice.

There are a lot of applications that can apply PAI technologies, even if some of them have not been studied in details yet. They can be divided in pre-clinical and clinical applications.

Pre-Clinical Applications

Among this group, we can find the imaging of non-fluorescent pigments, such as blood cells, melanin, water, and lipids. Then, there is the study of angiogenesis, microcirculation physiology and pathology.

With PAI techniques it is also possible to control the drug response during screening therapies. Applications in brain functions studies are also possible, as well as biomarker characterization and gene activity analysis through reporter genes [20].

Clinical Applications

PAI modalities could be used in the clinical practice mainly for melanoma screening and breast or prostate cancer detection. They could also be helpful in surveying the early response in chemotherapy and improve the dosimetry in thermal therapy. PAI can be applied to endoscopy too: as a matter of fact, an endoscopic probe for the gastrointestinal tract and colon imaging has been recently developed [21].

In addition, PAI could make guided needle biopsy easier. Currently, the needle is guided by ultrasounds. The problem is that the needle is usually tilted with respect to the horizontal plane. Since the needle is made of metal, it reflects the ultrasonic waves away from the transducer. As a result, it is possible to detect the needle only when it moves, because of changes in the speckle pattern. Photoacoustic waves, instead, are emitted in every direction, so the needle is visible even if it doesn't move.

Moreover, with PAI techniques, blood flow, oxygenation, and tissue metabolism imaging is possible, as well as neonatal and adult brain mapping [20].

Chapter 2

Generation of Photoacoustic Waves

2.1 Introduction

Biological tissues can be referred to as turbid media. This means that they are characterized by strong optical scattering and weak optical absorption, at least in the 400-1350 nm spectral range [22]. Many models have been created to describe photon migration in tissues. The most famous and used ones are the Monte Carlo method and the *Radiative Transport Equation* (RTE). The former is a very accurate numerical simulation of photon propagation, but it takes a long time to get the solution, because it calculates the path of every single injected photon. The RTE, instead, is an analytical method. As this equation is very difficult to solve, it is often approximated to a diffusion equation, which has solutions that are more computationally efficient, even if less accurate, than those provided by Monte Carlo simulations and by RTE [23].

As photoacoustic waves are generated by the absorption of light, after it has been injected into the tissue, it is necessary to consider one of these propagation methods. In this way, it is possible to model the photon migration from the light spot, that illuminates the tissue surface, to the absorbers embedded in the studied sample. As a matter of fact, this could be helpful in evaluating the light intensity profile as a function of depth and to choose the illumination pattern that suites the desired PAI modality.

After the photon propagation in biological media has been described, it is important to model the initial photoacoustic pressure generation, due firstly to the absorption and conversion of radiative energy into heat and secondly to the thermoelastic expansion. This allows us to calculate the sensitivity of PAI techniques, making it possible to

evaluate the magnitude increase of the photoacoustic signal with respect to an increase in the used optical power.

In the present chapter, after the definition of some important optical quantities, these two mathematical descriptions, namely the RTE with its diffusion approximation and the initial pressure generation, are described in details.

2.2 Definitions of Optical Quantities

Before looking at the RTE theory, it is necessary to define some common optical parameters and quantities.

The absorption properties of a biological medium are described by the *absorption coefficient* μ_a. It is defined as the probability of photon absorption in the medium per unit path length. In tissues, it has a representative value of 0.1 cm^{-1}. Its reciprocal is called *mean absorption length*, because it corresponds to the mean path length that the photon has to travel before it encounters an absorption event. In formulae, if we indicate the absorption cross section with σ_a, which indicates the absorbing capability of a single absorber, and with N_a the number density of the absorbers in the medium, the absorption coefficient can be considered as the total cross-sectional area for absorption per unit volume:

$$\mu_a = N_a \sigma_a. \tag{2.1}$$

The scattering properties, instead, are described by the *scattering coefficient* μ_s, defined correspondingly as the probability of photon scattering per unit path length. Its representative value in tissues is 100 cm^{-1}. The reciprocal of μ_s is called *scattering mean free path*. Again, if we call σ_s the scattering cross section for a single scatterer, which is its scattering capability, and N_s the number density of scatterers in the medium, the scattering coefficient can be considered as the total cross-sectional area for scattering per unit volume:

$$\mu_s = N_s \sigma_s. \tag{2.2}$$

With these two parameters, it is possible to define the *extinction coefficient* μ_t, also called *total interaction coefficient*, as:

$$\mu_t = \mu_a + \mu_s. \tag{2.3}$$

Its reciprocal $l_t = 1/\mu_t$ is the *mean free path* between interaction events.

It has been observed that there are two kinds of scattering: one is due to light scattering from particles that are smaller than the wavelength of the radiation; the other is due to particles comparable or bigger than the wavelength. In the former case, Rayleigh theory is applied and the photon has the same probability to be scattered forward or backward. In the second case, Mie theory is the best model and the photon is scattered mainly forward. A description of the two models can be found in Ref. [24]. The problem, when considering biological tissues, is that there are a lot of different organelles and structures that can scatter the light and their size varies from less than 10 nm for membranes to more than 10 μm for cells. As a result, none of the two scattering models can properly describe the phenomenon. It is usually convenient, indeed, to define a generic probability function $p(\theta)$ that must be adapted to the specific experimental situation. $p(\theta)$ represents the probability for a photon to be scattered with an angle θ from its direction of propagation. Then, it is possible to define an *anisotropy coefficient* g as the mean value of the cosine of the scattering angle:

$$g = \langle \cos(\theta) \rangle = \frac{\int_{4\pi} p(\theta) \cos(\theta)\, d\Omega}{\int_{4\pi} p(\theta)\, d\Omega}, \tag{2.4}$$

where $d\Omega$ is the infinitesimal solid angle.

Coefficient g assumes values between -1 and 1. A value of zero indicates isotropic scattering, while a value close to unity means that the scattering is predominantly in the forward direction. Experimentally, g takes values between 0.7 and 0.9 for the majority of biological tissues [25].

In order to take into account the anisotropy, while evaluating the scattering property of a tissue, another scattering coefficient is defined. It is called *reduced* (or *transport*) *scattering coefficient* and it is equal to:

$$\mu_s' = \mu_s(1 - g). \tag{2.5}$$

As a result, if the anisotropy is very high and the photons are scattered mainly in the forward direction, even if the scattering events are very frequent, we can see their effects only after a bigger distance than the scattering mean free path.

Consequently, a *reduced* (or *transport*) *interaction coefficient* μ_t' is defined as:

$$\mu_t' = \mu_a + \mu_s', \tag{2.6}$$

and its reciprocal $l'_t = 1/\mu'_t$ is referred to as the *transport mean free path.*

Finally, other two parameters are often used: *diffusion coefficient* D and *effective attenuation coefficient* μ_{eff}. They are defined as follows:

$$D = \frac{1}{3(\mu_a + \mu'_s)}, \tag{2.7}$$

$$\mu_{eff} = \sqrt{\frac{\mu_a}{D}} = \sqrt{3\mu_a(\mu_a + \mu'_s)}. \tag{2.8}$$

To describe light propagation in tissues, many optical quantities are used. The first one is the *spectral radiance* L_ν, which is defined as the energy that flows per unit normal area[1], per unit solid angle, per unit time, and per unit frequency interval. With this quantity, it is possible to define the *radiance* L as the spectral radiance integrated over a narrow frequency range $[\,\nu,\, \nu + \Delta\nu\,]$:

$$L(\vec{r}, \hat{s}, t) = L_\nu(\vec{r}, \hat{s}, t)\Delta\nu \qquad (W\ m^{-2}\ sr^{-1}). \tag{2.9}$$

In this relation, $\vec{r}$ is the position, $\hat{s}$ is the unit direction vector, t is time, and, enclosed in brackets on the right, the physical units of the radiance are shown. As we will see, radiance is the dependent variable of the RTE.

If radiance is integrated on the whole 4π solid angle, the *fluence rate* Φ is obtained:

$$\Phi(\vec{r}, t) = \int_{4\pi} L(\vec{r}, \hat{s}, t)\, d\Omega \qquad (W\ m^{-2}). \tag{2.10}$$

It represents the energy flow per unit area and per unit time, regardless of the flow direction. It is the intensity of the radiation.

If fluence rate is integrated in time, we obtain the *fluence* F:

$$F(\vec{r}) = \int_{-\infty}^{+\infty} \Phi(\vec{r}, t)\, dt \qquad (J\ m^{-2}). \tag{2.11}$$

To take into account also the direction of the energy flow, it is possible to define the *current density* (or *energy flux*) $\vec{J}$ as:

$$\vec{J}(\vec{r}, t) = \int_{4\pi} \hat{s} L(\vec{r}, \hat{s}, t)\, d\Omega \qquad (W\ m^{-2}). \tag{2.12}$$

[1]The normal area is perpendicular to the flow direction.

It represents the net[2] energy flow per unit area and per unit time. This equation is the vector counterpart of Eq. 2.10.

Since we need to consider how much light is absorbed, two other quantities are important for our purposes. The first one is the *specific absorption rate* A_p, that is defined as the optical energy absorbed by the medium per unit volume and per unit time. Its expression is:

$$A_p(\vec{r}, t) = \mu_a \Phi(\vec{r}, t) \qquad (W\ m^{-3}). \tag{2.13}$$

The second one is the integral of A_p over time and it is called *specific absorption* A_e:

$$A_e(\vec{r}) = \int_{-\infty}^{+\infty} A_p(\vec{r}, t)\, dt \qquad (J\ m^{-3}). \tag{2.14}$$

2.3 Radiative Transport Equation Theory

Initially, the RTE theory was developed for the propagation of beams of non-interactive particles through media, like neutron beams in nuclear reactors. As a result, within this model, light is treated like an ensemble of photons, ignoring its wave description. During their propagation, photons can be converted into other forms of energy, if they hit an absorbing centre, otherwise they proceed freely, unless a scattering centre on their path changes their travelling direction [25]. Note that, in this model, only elastic scattering events are considered. In addition, all the optical properties (like μ_a, μ_s', g, and the refractive index n) are considered to be invariant in time, but variant in space.

The RTE is derived heuristically from the principle of energy conservation and from some considerations about how the number of photons changes in an infinitesimal cylindrical volume. Refer to Figure 2.1 to see the considered volume element.

The cylinder is oriented in the direction of photon propagation $\hat{s}$. This means that its bases, with area dA, are orthogonal to $\hat{s}$. The length of the cylinder is called ds. The infinitesimal solid angle $d\Omega$ is considered in order to evaluate the changes in photon energy. Another differential solid angle $d\Omega'$, centred around unit vector $\hat{s}'$, is defined too.

If we indicate the speed of light in the medium with v_l, it is possible to see that the propagating energy per unit volume per unit solid angle can be obtained by taking the

[2] $\vec{J}$ points to the direction of the prevalent flow, as flows in opposite directions partially cancel each other.

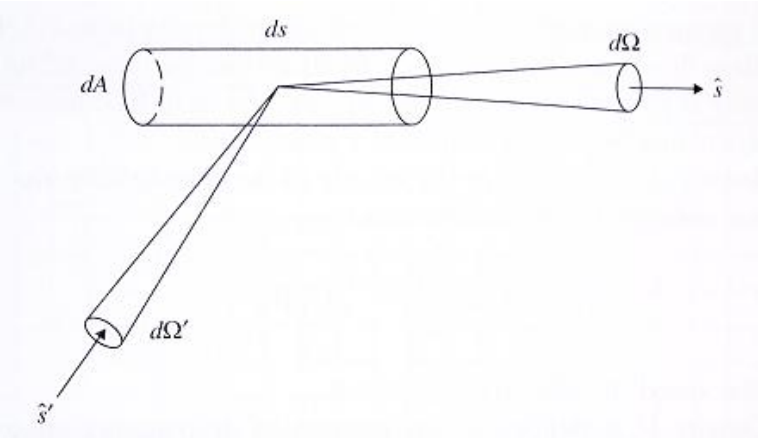

FIGURE 2.1: Sketch of the infinitesimal cylindrical volume used to deduce the RTE.

ratio between the radiance and the speed of light L/v_l. As a result, we can write the energy variation in the considered volume element, within the infinitesimal solid angle per unit time, as:

$$dP = \frac{\partial L(\vec{r}, \hat{s}, t)/v_l}{\partial t}\, ds\, dA\, d\Omega = \frac{\partial L(\vec{r}, \hat{s}, t)/v_l}{\partial t}\, dV d\Omega, \tag{2.15}$$

where $dV = ds\, dA$ is the volume of the infinitesimal cylinder. We indicate the found quantity with dP, because it is the energy variation in time, which is usually referred to as a power.

This net variation dP is actually given by the algebraic sum of terms that account for the increase and decrease of energy inside the cylinder for different reasons. As a matter of fact, it is possible to write:

$$dP = -dP_{div} - dP_{ext} + dP_{sca} + dP_{src}, \tag{2.16}$$

where dP_{div} is the divergence term, dP_{ext} is the extinction term, dP_{sca} is the scattering term, and dP_{src} is the source term. The signs take into account the actual positive or negative effect that the term brings to the total energy variation.

It is now necessary to find an expression for each of all these terms.

Divergence Term

This term arises from the photon propagation scheme around the direction $\hat{s}$. If the local beam is not collimated, the divergence is not zero. In this case, it is possible to

evaluate the magnitude of the divergence of $L(\vec{r}, \hat{s}, t)$ along the propagation direction.

As a result, the energy that is diverging out from the infinitesimal volume, or the infinitesimal solid angle, per unit time is:

$$dP_{div} = \hat{s} \cdot \nabla L(\vec{r}, \hat{s}, t)\, d\Omega\, dV. \tag{2.17}$$

Note that this term does not depend on the scattering properties of the medium, but only on the propagation features of the beam. In addition, it is positive if there is divergence and it is negative if there is convergence.

Extinction Term

The light that propagates along $\hat{s}$, inside the infinitesimal cylinder, can be absorbed or, otherwise, scattered towards different directions. The quantity $(\mu_t\, ds)$ is the probability that the photon undergoes extinction in the medium.

As a result, the energy loss per unit time in the infinitesimal volume within the solid angle element, due to both absorption and scattering, is:

$$dP_{ext} = (\mu_t\, ds)\, [L(\vec{r}, \hat{s}, t)\, dA\, d\Omega] = \mu_t\, L(\vec{r}, \hat{s}, t)\, dV\, d\Omega. \tag{2.18}$$

Again, if there is loss, the term is positive.

Scattering Term

Photons that come from a generic direction $\hat{s}'$, passing through the cylinder, can be scattered along the $\hat{s}$ direction, with a probability of $(\mu_s\, ds)P(\hat{s}', \hat{s})$. This would increase the total energy in the volume element.

The quantity $(\mu_s\, ds)$ represents the probability that the photon is actually scattered, while the function $P(\hat{s}', \hat{s})$ is a *Probability Density Function* (PDF) and it is the probability for the photon, propagating along $\hat{s}'$, to be scattered in the $\hat{s}$ direction. Usually, this PDF depends only on the angle between the scattered and incident directions. So we can write $P(\hat{s}', \hat{s}) = P(\hat{s}' \cdot \hat{s})$.

As a result, if we integrate the product of the radiance and the global probability on the whole solid angle, it is possible to obtain the energy increase per unit time due to the scattering.

In formulae, this is equal to:

$$\begin{aligned} dP_{sca} &= (\mu_s\, ds) \left[\int_{4\pi} L(\vec{r}, \hat{s}', t) P(\hat{s}' \cdot \hat{s})\, d\Omega' \right] dA\, d\Omega \\ &= \mu_s \left[\int_{4\pi} L(\vec{r}, \hat{s}', t) P(\hat{s}' \cdot \hat{s})\, d\Omega' \right] dV\, d\Omega. \end{aligned} \tag{2.19}$$

Source Term

Photons can be created, at least in theory, directly inside the considered volume and this would increase the energy content too. If there is a light source, the energy that it produces in the volume element within the infinitesimal solid angle per unit time can be expressed by:

$$dP_{src} = S(\vec{r}, \hat{s}, t)\, dV\, d\Omega. \tag{2.20}$$

$S(\vec{r}, \hat{s}, t)$ is a power per unit volume per unit solid angle ($\left[W\ m^{-3}\ sr^{-1}\right]$).

Final Form of the RTE

Now that we have found all the contributions to the energy variation in the studied infinitesimal cylinder, we can merge them altogether in order to achieve the final form of the RTE.

Substituting Eqs. 2.15 and 2.17-2.20 into Eq. 2.16, we get:

$$\begin{aligned} \frac{\partial L(\vec{r}, \hat{s}, t)/v_l}{\partial t} = &- \hat{s} \cdot \nabla L(\vec{r}, \hat{s}, t) - \mu_t\, L(\vec{r}, \hat{s}, t) \\ &+ \mu_s \int_{4\pi} L(\vec{r}, \hat{s}', t) P(\hat{s}' \cdot \hat{s})\, d\Omega' + S(\vec{r}, \hat{s}, t), \end{aligned} \tag{2.21}$$

which is the radiative transport equation [23].

2.4 Diffusion Theory

The RTE has six degrees of freedom: three spatial coordinates (x, y, z) for identifying vector $\vec{r}$, two angular coordinates (θ, ϕ) for determining unit vector $\hat{s}$, and one temporal

coordinate (t). As a result, it is computationally intense to find its solution, which results in very long calculation times.

In order to simplify the RTE, some approximations are assumed:

1. Biological tissues are considered high-albedo scattering media. This means that $\mu_s \gg \mu_a$ and that the radiance can be considered isotropic after a little propagation of the beam.
2. The fractional change in the current density of photons $\vec{J}(\vec{r},t)$ is assumed to be very small within a transport mean free path l_t'.

These two approximations are at the base of the diffusion theory. As a matter of fact, with the first approximation, we can think the radiance to be mainly isotropic with only a small superimposed anisotropic perturbation part.

Analytically, this is equivalent to the radiance expansion in spherical harmonics truncated to first order. This corresponds to:

$$L(\vec{r},\hat{s},t) \approx \sum_{n=0}^{1} \sum_{m=-n}^{n} L_{n,m}(\vec{r},t)\, Y_{n,m}(\hat{s}), \tag{2.22}$$

where $L_{n,m}$ are the expansion coefficients. The term for $n = 0$ and $m = 0$ refers to the isotropic scattering, while the terms for $n = 1$ and $m = -1, 0, 1$ refer to the anisotropic part.

Performing the substitutions of the actual spherical harmonics and calculating the fluence rate and the current density with the radiance obtained, it is possible to see that[3]:

$$L_{0,0}(\vec{r},t)Y_{0,0}(\hat{s}) = \frac{\Phi(\vec{r},t)}{4\pi}, \tag{2.23}$$

$$\sum_{m=-1}^{1} L_{1,m}(\vec{r},t)Y_{1,m}(\hat{s}) = \frac{3}{4\pi}\vec{J}(\vec{r},t)\cdot\hat{s}, \tag{2.24}$$

where Eq. 2.23 is the isotropic term and Eq. 2.24 represents the anisotropic terms. Note that the anisotropic term is proportional to the projection of $\vec{J}(\vec{r},t)$ on the propagation direction $\hat{s}$.

[3]The reader, who is interested in all the mathematical passages, can find them in Ref. [23].

Consequently, in the diffusion approximation, the radiance can be expressed by:

$$L(\vec{r}, \hat{s}, t) = \frac{\Phi(\vec{r}, t)}{4\pi} + \frac{3}{4\pi}\vec{J}(\vec{r}, t) \cdot \hat{s}. \tag{2.25}$$

In addition, the source can be considered isotropic[4] too, because $\mu_s \gg \mu_a$. As a result, it does not depend on $\hat{s}$. We can write it as:

$$S(\vec{r}, \hat{s}, t) = \frac{S(\vec{r}, t)}{4\pi}. \tag{2.26}$$

Now it is possible to substitute Eq. 2.25 and Eq. 2.26 into the RTE (Eq. 2.21). If we take also the integral on the whole solid angle of the equation, we get:

$$\frac{\partial \Phi(\vec{r}, t)}{v_l \, \partial t} + \mu_a \Phi(\vec{r}, t) + \nabla \cdot \vec{J}(\vec{r}, t) = S(\vec{r}, t). \tag{2.27}$$

It is possible to note that, in this equation, $\hat{s}$ is not present anymore. However, it depends on two different quantities, namely $\Phi(\vec{r}, t)$ and $\vec{J}(\vec{s}, t)$. If the second approximation of the diffusion theory is assumed, nevertheless, it is possible to relate the current density to the fluence rate through the Fick's law:

$$\vec{J}(\vec{r}, t) = -D\nabla\Phi(\vec{r}, t). \tag{2.28}$$

Note that this equation can only be used in the following case:

$$\left(\frac{l_t'}{v_l}\right)\left(\frac{1}{|\vec{J}(\vec{r}, t)|}\left|\frac{\partial \vec{J}(\vec{r}, t)}{\partial t}\right|\right) \ll 1, \tag{2.29}$$

which is the analytical expression of the already mentioned second approximation. Indeed, the first term in brackets is the time for the photons to travel a space equal to l_t', while the second one is the fractional variation in the current density per unit time.

Fick's law is widely used to describe free diffusion in very different contexts, but it cannot be applied if the propagation is subjected to external driving forces.

[4]The source is considered isotropic even if it comes from a collimated laser beam, because, due to high scattering, photons lose memory of their original direction soon. However, diffusion theory can be inaccurate if we are interested in calculating the fluence rate close to the surface. In this case some corrections must be introduced [26].

Finally, if we substitute Eq. 2.28 into Eq. 2.27, it is possible to find the *diffusion equation*:

$$\frac{\partial \Phi(\vec{r},t)}{v_l\,\partial t} + \mu_a \Phi(\vec{r},t) - \nabla \cdot [D \nabla \Phi(\vec{r},t)] = S(\vec{r},t), \tag{2.30}$$

which, actually, is the one used to calculate the photon distribution in turbid media like tissues. It has, indeed, only four degrees of freedom instead of six, because $\hat{s}$ is not present in the equation.

This equation can now be solved in particular cases by choosing proper sources.

Time-Dependent Point Source

With Eq 2.30, it is possible to find the impulse response of an infinite homogeneous scattering medium.

We can consider, indeed, an infinitely short-pulsed point source $S(\vec{r},t) = \delta(\vec{r},t)$. If we solve the diffusion equation with this source, for $t > 0$, we obtain:

$$\Phi(\vec{r},t) = \frac{v_l}{(4\pi D v_l t)^{3/2}} \exp\left(-\frac{r^2}{4Dv_l t} - \mu_a v_l t\right), \tag{2.31}$$

which is usually referred to as *Green function*. Note that this solution breaks causality, because it gives a non-zero fluence rate value for every $t > 0$. It does not consider the finite propagation speed of photons.

After the impulse response has been found, it is possible to find the response to an arbitrary light source distribution just by taking the convolution of the Green function (Eq. 2.31) with the specific source used.

Time-Independent Point Source

If the source does not depend on time, neither does the fluency rate. As a result, the partial time derivative in Eq. 2.30 goes to zero. The diffusion equation, in this case, can be rewritten as:

$$\Phi(\vec{r}) - \frac{1}{\mu_{eff}^2} \nabla^2 \Phi(\vec{r}) = \frac{S(\vec{r})}{\mu_a}. \tag{2.32}$$

Here we choose a time-independent point source $S(\vec{r}) = \delta(\vec{r})$, obtaining the following solution for Eq. 2.32:

$$\Phi(\vec{r}) = \frac{1}{4\pi D\, r} \exp(-\mu_{eff}\, r). \tag{2.33}$$

This equation can be used to evaluate the fluence rate distribution in space inside a scattering medium, when the spot light on the surface is very small [23].

2.5 Initial Photoacoustic Pressure Generation

Laser heating is a phenomenon that can be used in very different contexts and the response of tissues can be different depending on the duration of laser excitation. In particular, two relaxation times must be considered:

1. *Thermal relaxation time* is expressed by:

$$\tau_{th} = \frac{d_c^2}{4\,\alpha_{th}}, \tag{2.34}$$

   where d_c is the characteristic dimension of the heated zone of interest and α_{th} is the thermal diffusivity[5]. This parameter describes the thermal diffusion and can be derived in the heat conduction theory [25].

   If the laser excitation is shorter than τ_{th}, the heating process is said to be in *thermal confinement*. This means that, during illumination, thermal conduction is negligible, because heat cannot propagate outside the illuminated region of interest.

2. *Stress relaxation time* is expressed by:

$$\tau_{st} = \frac{d_c}{v_s}. \tag{2.35}$$

   This parameter describes the pressure propagation, since pressure waves travel at the speed of sound v_s in tissues.

   If the laser excitation is shorter than τ_{st}, the heating process is said to be in *stress confinement*. This means that, during illumination, stress propagation is negligible, because the pressure rise cannot reach the boundaries of the illuminated region of interest.

[5] Physical dimensions of the thermal diffusivity α_{th} are $[m^2/s]$. Its value in tissues is similar to the one assumed in water, which is of $1.4 \cdot 10^{-7} m^2/s$.

In the following discussion, we will assume that the pulse width τ_p is less than both τ_{th} and τ_{st}. As a matter of fact, this condition simplifies the mathematical model for initial pressure generation and propagation. Nevertheless, it is reasonable, because τ_p is often chosen in the nanosecond scale for photoacoustic applications, while τ_{th} and τ_{st} are in the second/microsecond scales respectively, if $d_c \approx 1\ mm$ [6].

In order to find the expression of the initial photoacoustic pressure due to laser light absorption, we can start writing the fractional volume expansion formula:

$$\frac{dV}{V} = -\kappa p + \beta T, \tag{2.36}$$

where V is volume, p is change in pressure, T is change in temperature, κ is the isothermal compressibility[6], and β is the thermal volume expanding coefficient[7].

The isothermal compressibility has the following expression:

$$\kappa = \frac{c_p}{\rho\, v_s^2\, c_v}, \tag{2.37}$$

where c_v and c_p are specific heat capacities[8] at constant volume and pressure respectively, and ρ is the mass density[9].

As said, it is usually possible to assume that laser excitation is in both thermal and stress confinement. In this case, regarding Eq. 2.36, we can neglect the fractional volume expansion immediately after the laser pulse. As a result, the initial photoacoustic pressure rise, in this case, is:

$$p_0 = \frac{\beta T}{\kappa}. \tag{2.38}$$

It is known, from thermodynamics, that the relation between temperature variation and internal energy variation ΔE is:

$$\Delta E = m\, c_v\, T, \tag{2.39}$$

where m is mass.

[6]Isothermal compressibility assumes a value of $\kappa \approxeq 5 \cdot 10^{-10}$ Pa^{-1} in water and soft tissue.

[7]Expanding coefficient assumes a value of $\beta \approxeq 4 \cdot 10^{-4}$ K^{-1} in tissue.

[8]In tissue, c_v and c_p are $\sim$4000 $J\,kg^{-1}\,\mathrm{K}^{-1}$. Note that, in condensed matter, they assume roughly the same value, while they can be different in gases and vapors.

[9]For water and soft tissue, $\rho \approxeq 1000\ kg/m^3$.

We can also assume that ΔE depends on the energy delivered by light as follows:

$$\Delta E = \eta_{th} A_e V, \tag{2.40}$$

where η_{th} is the percentage of specific optical absorption (A_e) that is actually converted into heat.

If we unite Eq. 2.39 and Eq. 2.40, we can find that:

$$T = \frac{\eta_{th} A_e V}{m\, c_v} = \frac{\eta_{th} A_e}{\rho\, c_v}. \tag{2.41}$$

Now, if we substitute this expression into Eq. 2.38, we obtain:

$$p_0 = \frac{\beta}{\kappa\, \rho\, c_v} \eta_{th} A_e. \tag{2.42}$$

The dimensionless parameter:

$$\Gamma = \frac{\beta}{\kappa\, \rho\, c_v} = \frac{\beta v_s^2}{c_p}, \tag{2.43}$$

is defined as *Grüneisen parameter*. At body temperature, this parameter is equal to $\Gamma(37℃) = 0.20$. As a result, Eq. 2.42 becomes:

$$p_0 = \Gamma\, \eta_{th} A_e = \Gamma\, \eta_{th}\, \mu_a F. \tag{2.44}$$

With this result, it is possible to estimate the intrinsic sensitivity of PAI techniques, that expresses how much the pressure signal amplitude improves, if fluence F of the laser radiation is increased of a given amount.

Indeed, if we excite the tissue, characterized by a $\mu_a \simeq 0.1\ cm^{-1}$, with a fluence of $F = 20\ mJ/cm^2$, which corresponds in general to the exposure limit to laser light for tissues in photoacoustic applications[10], we find that:

$$A_e = 0.1\ cm^{-1} * 20\ mJ/cm^2 = 2\ mJ/cm^3.$$

Note that, since $1\ J/m^3 = 1$ Pa $= 10^{-5}$ bar, specific optical absorption is also equal, in this case, to $A_e = 20\ m$bar.

[10] For more details on the maximum permissible exposure to laser light for tissues see Section 4.2.1.

We can further find that:

$$T = \frac{A_e}{\rho\, c_v} = \frac{2\ mJ/cm^3}{1\ g/cm^3 * 4\ J/g/\mathrm{K}} = 0.5\ m\mathrm{K},$$
$$p_0 = \Gamma A_e = 0.20 * 20\ m\mathrm{bar} = 4\ m\mathrm{bar},$$

where it is assumed that $\eta_{th} = 1$. This result also shows that, for each millikelvin temperature rise, 8 $m$bar are produced as pressure rise [6].

Note that the generated photoacoustic pressure is very small, if compared to pressure rises usually created by transducers in US. Even if those values can vary greatly, the compression peak can be of 50 bar (5 MPa) for normal US or about 1 bar (100 kPa) for continuos wave Doppler US [27]. This means that PAI signals are at least three orders of magnitude weaker. Since they can still be detected, this makes us sure that no mechanical damage will be caused to tissues. As a result, it is only necessary to care about the maximum exposure limit for laser light.

Chapter 3

Propagation and Revelation of Photoacoustic Waves

3.1 Introduction

In the previous chapter, we have seen that a target, embedded in a tissue, generates an initial pressure distribution thanks to the thermoelastic expansion after it has been heated by laser radiation. However, this pressure starts immediately to travel away from the target as an acoustic wave, bringing information about acoustic and geometrical features of its source. It is important to understand how this propagation can be mathematically modelled.

As a matter of fact, many PAI techniques rely on this propagation model to retrieve the initial pressure distribution from the measurements. This approach consists in solving the inverse propagation problem, as it is done in PAT.

In this chapter, indeed, the general photoacoustic equation is derived and its solution for an arbitrary heating distribution function is provided too. Moreover, graphs of the solution for particular source geometries are shown.

As already mentioned, the present thesis is about using, for photoacoustic applications, a common commercial ultrasonic scanner which usually deals with standard US. As a result, after the description of some properties that ultrasound signals show, the differences between ultrasonic and photoacoustic waves are presented. Indeed, beside being differently generated, these waves also have distinct behaviours, that must be taken into account in order to reconstruct properly the image.

As a consequence, a specific detection and elaboration method for the signals in PAM is described. Actually, it is extensively used in the development of the PAM system within the project.

3.2 General Propagation Equation for Photoacoustic Waves

3.2.1 Simplifying Hypotheses

Before considering photoacoustic waves propagation into tissues, it is important to state all the hypotheses that are assumed in order to simplify the model [28]. They are shown in the following list:

1. Soft tissue is modelled as an *inviscid fluid*. This means that its viscosity is assumed to be very small. This hypothesis is useful in order to exclude the presence of transverse waves in the photoacoustic signal. Since a heat source usually generates only longitudinal waves, whose speed in soft tissue is anyway a thousand times bigger than that of shear waves, this approximation can be considered valid.

2. Acoustic absorption in tissues is neglected, because it is complex to take into account this phenomenon in the model. However, this approximation is not accurate, because photoacoustic signals have a very high frequency content and they can travel significant distances before reaching the detector. As a matter of fact, acoustic absorption is about 1 dB cm^{-1} Mhz^{-1}, so it is proportional to frequency and distance.

3. It is not only assumed that the condition for thermal confinement is verified, but also that thermal relaxation time is much greater than the stress one, i.e., $\tau_{th} \gg \tau_{st} = d_c/v_s$. This means that thermal conductivity can be neglected during the elaboration of the model. This approximation is usually valid for biological media.

4. The tissue is assumed to be homogeneous and isotropic, which means that its mechanical properties, like density and speed of sound, do not depend on direction and they assume the same values in the whole medium. This hypothesis, though, is quite coarse and, despite the fact that it usually works pretty well, it can limit sometimes the image resolution when big heterogeneities are present.

5. Pressure and density variations are assumed to be small with respect to their equilibrium values. Moreover, displacement velocities of particles are supposed to

be much slower than the speed of sound. This assumptions are reasonable and they allow us to start from linearized thermal expansion and motion equations.

3.2.2 Photoacoustic Equation

In order to find the photoacoustic equation, we begin from the thermal expansion equation:

$$\nabla \cdot \vec{\xi}(\vec{r}, t) = -\kappa p(\vec{r}, t) + \beta T(\vec{r}, t), \tag{3.1}$$

that is exactly equivalent to Eq. 2.36 in Section 2.5, where $\vec{\xi}$ is the medium displacement.

We also need to consider the equation of motion, called linear inviscid force equation, expressed by:

$$\rho \frac{\partial^2}{\partial t^2} \vec{\xi}(\vec{r}, t) = -\nabla p(\vec{r}, t). \tag{3.2}$$

This equation is, in fact, a particular form of Newton's second law, since the left-hand member is the mass density times the acceleration, while the right-hand member represents the applied force per unit volume.

At this point, if we take the divergence of Eq. 3.2:

$$\rho \frac{\partial^2}{\partial t^2} \left[\nabla \cdot \vec{\xi}(\vec{r}, t) \right] = -\nabla^2 p(\vec{r}, t) \tag{3.3}$$

and we substitute Eq. 3.1 into Eq. 3.3, we obtain:

$$\left(\nabla^2 - \kappa \rho \frac{\partial^2}{\partial t^2} \right) p(\vec{r}, t) = -\beta \rho \frac{\partial^2 T(\vec{r}, t)}{\partial t^2}. \tag{3.4}$$

Knowing that the speed of sound can be written as $v_s = 1/\sqrt{\kappa \rho}$, it is possible to rewrite Eq. 3.4 as:

$$\left(\nabla^2 - \frac{1}{v_s^2} \frac{\partial^2}{\partial t^2} \right) p(\vec{r}, t) = -\frac{\beta}{\kappa v_s^2} \frac{\partial^2 T(\vec{r}, t)}{\partial t^2}. \tag{3.5}$$

This is the *general photoacoustic equation*. The left-hand member describes wave propagation, while the right-hand one represents the source term.

As we have assumed that we are in thermal confinement, we can use the following thermal equation:

$$\rho\, c_v \frac{\partial T(\vec{r},t)}{\partial t} = H(\vec{r},t), \tag{3.6}$$

that exactly corresponds to Eq. 2.39 in Section 2.5, just derived in time and divided by the volume. As a matter of fact, $H(\vec{r},t)$ is the heating function, defined as the thermal energy converted from light per unit volume and per unit time. Note that the heating function is related to the specific absorption rate A_p and to the fluence rate Φ by $H = \eta_{th} A_p = \eta_{th}\, \mu_a \Phi$.

As a result, if we substitute Eq. 3.6 into Eq. 3.5, we get:

$$\left(\nabla^2 - \frac{1}{v_s^2}\frac{\partial^2}{\partial t^2}\right) p(\vec{r},t) = -\frac{\beta}{c_p}\frac{\partial H(\vec{r},t)}{\partial t}. \tag{3.7}$$

It is important to note that the source term now depends on the first derivative of H. This means that the photoacoustic wave is generated only if the heating function varies in time. This is the reason why, in PAI techniques, only pulsed or modulated light sources are employed [6].

3.2.3 General Solution

The common way to solve the general photoacoustic equation is by using the Green function approach, which applies the Green's theorem to reduce integrals on the volume of interest in integrals on a surface that encloses this volume.

The *Green's function* $G(\vec{r},t;\vec{r}\,',t')$ is defined, in this context, as the response of photoacoustic equation to a spatial and temporal impulse source. This means that it satisfies the following equation:

$$\left(\nabla^2 - \frac{1}{v_s^2}\frac{\partial^2}{\partial t^2}\right) G(\vec{r},t;\vec{r}\,',t') = -\delta(\vec{r}-\vec{r}\,')\delta(t-t'), \tag{3.8}$$

where $\vec{r}\,'$ is the position of the photoacoustic source and t' is the time of pulse emission. If we solve this equation in infinite space, we find that:

$$G(\vec{r},t;\vec{r}\,',t') = \frac{\delta\left(t - t' - \frac{|\vec{r}-\vec{r}\,'|}{v_s}\right)}{4\pi|\vec{r}-\vec{r}\,'|}, \tag{3.9}$$

which is the analytical expression of an impulse diverging spherical wave.

It is worth noting that the Green's function represents the response to a point photoacoustic source that is subjected to a step heating function, rather than an impulse heating function. This comes from the fact that the source term in the photoacoustic equation (Eq. 3.7) depends on the time derivative of the heating function. As a result, if this time derivative has to be equal to a time impulse, the heating function must be a step function. This is equivalent to say that the temperature rise must be a ramp.

At this point, if we apply the Green's function approach, we find that the general solution for Eq. 3.7 is:

$$p(\vec{r},t) = \int_{-\infty}^{t} dt' \int_{V'} d\vec{r}\,' G(\vec{r},t;\vec{r}\,',t') \frac{\beta}{c_p} \frac{\partial H(\vec{r}\,',t')}{\partial t'}, \tag{3.10}$$

that can be seen as the convolution of the impulse response with an arbitrary source function. Substituting further Eq. 3.9 into Eq. 3.10, it yields:

$$p(\vec{r},t) = \frac{\beta}{4\pi c_p} \int_{V'} d\vec{r}\,' \frac{1}{|\vec{r}-\vec{r}\,'|} \left[\frac{\partial H(\vec{r}\,',t')}{\partial t'}\right]_{t'=t-|\vec{r}-\vec{r}\,'|/v_s}. \tag{3.11}$$

This is the general forward solution for the photoacoustic equation. By choosing a proper geometry and a heating function, both suiting the actual used system, it is possible to find the photoacoustic pressure distribution generated in the tissue for every $t > 0$.

In Figure 3.1, the graphs of the solution for specific target geometries, that undergo delta-pulse excitations, are shown.

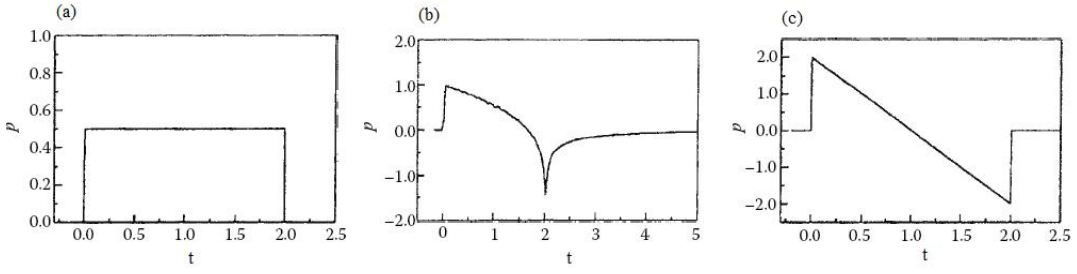

FIGURE 3.1: Graphs of photoacoustic pressure signals generated in specific geometries:(a) Slab; (b) Cylinder; (c) Sphere. On the y-axis there is pressure in arbitrary units, while on the x-axis there is normalized time.

These geometries are slab, cylinder, and sphere. Note that, for the slab, it is only shown the pressure that corresponds to the wave travelling along the positive propagation direction. There is an identical wave that propagates in the opposite direction.

Physically, what happens can be inferred from the graphs. In the slab case, after the delta heating excitation pulse, an initial pressure is generated inside the target. This pressure is then divided in two equal parts that travel in opposite directions as planar compression waves.

In the sphere case, similarly, the initial pressure is divided in two equal parts, but they start traveling like spherical compression waves. One wave is a diverging spherical one and travels outward the sphere. The other one, instead, is a converging spherical wave, that travels inward. When it reaches the center of the sphere, it turns into a diverging rarefaction wave. This is the reason why, in the sphere graph, half signal is positive in pressure and half is negative, while in the slab graph the signal is only positive [6].

The cylinder case resembles the spherical one, even if it has a different form, because of the different symmetry.

3.3 Ultrasonic Wave Properties

The term *acoustic wave* describes a pressure oscillation that is transmitted through a solid, a liquid, or a gas. Depending on the frequency that characterizes this oscillation, acoustic waves can be divided into three groups: infrasounds, audible sounds, and ultrasounds.

Infrasounds have frequencies lower than 20 Hz; audible sounds are in the range between 20 Hz and 20 kHz; ultrasounds have frequencies higher than 20 kHz. Among ultrasounds, there is a particular frequency window, from 1 MHz to 20 MHz, in which acoustic waves are called *diagnostic ultrasounds*. As a matter of fact, US uses this kind of wave to take images of structures and organs inside the human body.

One important parameter is defined for dealing with ultrasounds. It is the *acoustic impedance*, which is defined as the product between mass density and speed of sound:

$$Z = \rho\, v_s. \tag{3.12}$$

It is measured in Rayls ($1\ rayl = 1\ kg\, m^{-2}\, s^{-1}$). The values of impedance and speed of sound for some biological tissues and common media are shown in Table 3.1.

Note that, inside the body, the speed of sound can change greatly, from 1450 to 1570 m/s. As a result, its average value is often assumed to be 1540 m/s.

The wave amplitude p is expressed in terms of pressure and it is measured in Pascals.

Material	Speed of Sound (m/s)	Acoustic Impedance (MRayl)
Air	343	0.0004
Water	1490	1.48
Fat	1450	1.38
Myocardium	1550	1.62
Blood	1550	1.61
Liver	1570	1.65
Skull Bone	3360	6.00
Alluminum	6420	17.00

TABLE 3.1: Values of impedance and speed of sound for tissues and common media.

The wave intensity is usually considered too, and it is defined as:

$$I = \frac{p^2}{2\rho\, v_s}. \tag{3.13}$$

If the ultrasonic wave, while travelling into the tissue, meets a discontinuity in the impedance, it can be reflected with the following intensity reflectivity coefficient for normal incidence:

$$R = \left(\frac{Z_2 - Z_1}{Z_2 + Z_1}\right)^2, \tag{3.14}$$

where Z_1 is the acoustic impedance of the medium in which the wave is travelling (medium 1) and Z_2 is the acoustic impedance of the medium that the wave encounters (medium 2).

If the ultrasonic wave has an incidence angle θ_i, it can be reflected and refracted, following a sort of "acoustic Snell's laws":

$$\theta_i = \theta_r, \tag{3.15}$$

$$\frac{\sin\theta_t}{\sin\theta_i} = \frac{v_{s2}}{v_{s1}}, \tag{3.16}$$

where θ_r is the reflection angle, θ_t is the transmission angle, v_{s1} and v_{s2} are the sound speeds in medium 1 and 2, respectively.

3.4 Comparison Between Ultrasonic and Photoacoustic Waves

Photoacoustic signals can be treated like normal ultrasonic waves, but it is necessary to keep in mind the principal differences that exist between them.

First of all, because of light absorption and thermoelastic expansion, photoacoustic waves carry no net momentum, if we neglect the very small momentum that characterizes light[1]. Consequently, for every compression in the photoacoustic signal, in general, there must be a correspondent rarefaction. This is true in the case of cylindrical and spherical symmetry. In the case of a slab, the null net momentum is obtained by summing the two identical compression waves that leave the slab in opposite directions [29].

This fact is not true anymore when ultrasounds are produced in US. Since they are generated in the transducer, which is outside the tissue, these waves carry a non-zero net momentum through the medium.

Secondly, photoacoustic waves are broadband signals. Their bandwidth can be of several tens of MHz, depending also on the light pulse duration [8]. In addition, the frequency content varies accordingly to the dimensions of photoacoustic sources [30]. This means that targets in the millimeter scale can generate waves with a frequency up to 3 MHz, while in the scale of tens or hundreds of microns they can reach 25 MHz.

In US, instead, the frequency content of ultrasonic waves is due principally to the characteristics of the transducer that transmits the pulse. As a consequence, once the ultrasonic scanner has been chosen, the waves are always generated and detected with the same frequency.

Finally, a substantial difference between these two kinds of waves consists in the fact that, in order to bring information about the target, they travel different distances into the tissue. This happens because they share the same detection point, but the generation point is different. In US it coincides with the detection one, while in PAI it is located and distributed inside the tissue. This means that, if we are using standard ultrasonic waves, the signal, generated on the tissue surface, must reaches areas with a different acoustic impedance. After that, it is reflected by the separation surface and the echo is recollected by the transducer. As a result, we have to wait until the signal has completed its roundtrip.

[1] The momentum that light carries at $\lambda = 1064\ nm$ is $\mathrm{p} \approxeq 6.2 \cdot 10^{-28}\ kg\, m\, s^{-1}$.

In PAI, however, all targets, which are located inside the tissue volume irradiated by the laser, generate photoacoustic signals at the same time and they have to travel only one way from the source to the detector.

This fact must be taken into account to create proper reconstruction methods for each imaging modality.

Note also that US reconstructs acoustical reflectivity, while PAI techniques reconstruct optical absorption distribution.

3.5 Revelation and Elaboration of Photoacoustic Waves

Photoacoustic waves, like normal ultrasonic signals, can be detected by ultrasonic transducers. These devices are able to convert electrical energy into ultrasonic energy and vice versa. They can have different shapes and features, but all of them are based on the *piezoelectric effect*.

A piezoelectric element is able to change its physical dimensions when it is surrounded by an electrical field. This is due to a spatial rearrangement of the dipoles which constitute the material. Reversely, if a mechanical stress, like a compression, is applied to it, a net charge appears at its edges. As a result, if we send RF electrical signals to the piezoelectric element, ultrasonic waves of the same frequency are created. Then, with the same device, it is possible to reconvert the ultrasounds into electrical signals.

Quartz and tourmaline are natural piezoelectric materials, but ferroelectric ceramic materials, like lead zirconate titanate, are usually employed thanks to their superior performances.

Usually, arrays of piezoelectric elements are used to make ultrasonic images. They can be arranged in different shapes, forming linear, curved-linear, planar, and ring-shaped transducers.

Important parameters of a transducer, as shown in Figure 3.2, are pitch, which is the distance between the centers of two adjacent elements, and kerf, that is the space that separates two adjacent elements.

Moreover, also the center frequency ν_0 and the bandwidth $\Delta\nu$ of the transducer must be considered. As a matter of fact, every detector possesses a quality factor, defined as $Q = \nu_0/\Delta\nu$.

After the transducer has collected photoacoustic waves, it is possible to create different kinds of images. The simplest one is called *A-mode*, where A stands for amplitude.

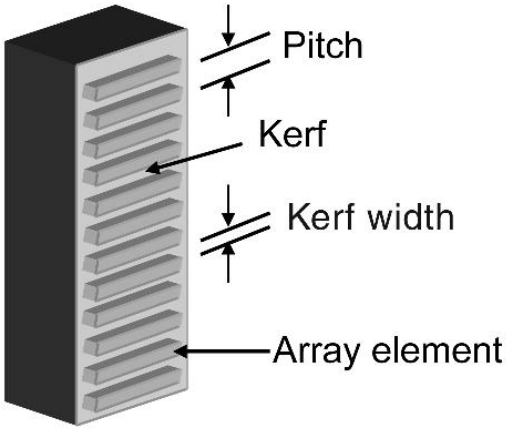

FIGURE 3.2: Representation of a linear ultrasonic transducer.

A-mode images consist in the graphic representation of the electrical signals that each array element measures versus time[2], after filtering and amplification. These images only consist in the RF signals displayed on the monitor.

The second type of images is called *B-mode*, where B stands for brightness. B-mode images are made by arranging the A-mode images, taken with all array elements, one next to the other in a gray scale, which depends on the RF signal intensity. In this way, it is possible to create a two-dimensional image, that corresponds to the slice of tissue just under the transducer.

These two image modalities are both used to analyse photoacoustic signals in the present thesis.

Usually, in order to perform B-mode images, it is useful to focus the signal. This can be done with acoustic lenses made of rubber or polymeric materials. However, when linear transducers are used, it exists an elaboration process that can synthetically focus acoustic signals. It is called *beamforming* or *delay-and-sum* algorithm.

The beamforming process is singularly applied to all scanlines that build up the image. A scanline is a line in depth, orthogonal to the transducer surface, which can scan the tissue beneath. Depending on the focus position and width, it is necessary to use a certain subset of detector elements in order to create it. See Figure 3.3 for clarification. Usually, 32 elements are used for this purpose, when the total number of elements is among 128 and 256. The bigger the number of elements in a scanline, the bigger the NA of the transducer, the better the lateral resolution, and the deeper the focus position. Note, however, that there is a trade off between the number of elements in a scanline

[2]Here time can be considered equivalent to space, since they are proportional. In fact: $x = v_s t$.

and the number of scanlines that form the image. This will be clear in Section 5.2, where an actual code for beamforming is explained.

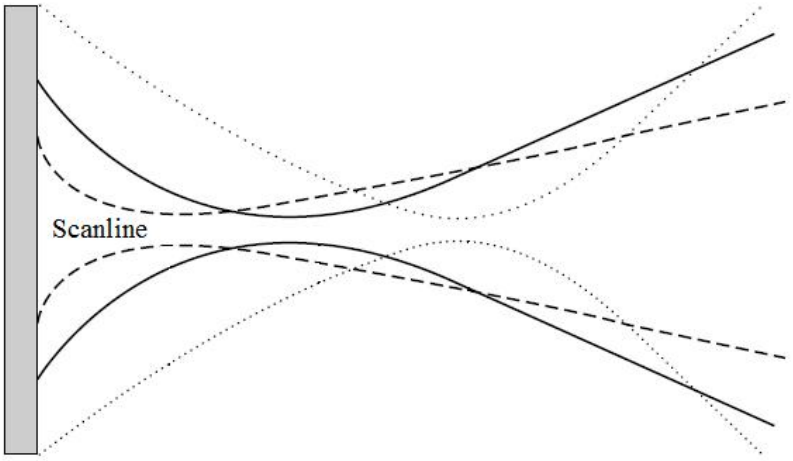

FIGURE 3.3: Scanlines of an ultrasonic transducer. Note that the bigger the aperture of the scanline, the smaller the beam waist at the focus and the deeper the focus position.

The beamforming, as the name suggests, is able to place the focus in a particular position of the depth axis. This can be done by choosing appropriate delays for the signals that each scanline element measures.

Consider a point source P of photoacoustic waves. As shown in Figure 3.4, it emits a signal that travels away like a spherical wave. As a result, this wave hits firstly the element that is tangent to the sphere. The other elements see the same signal, but only after a time $\Delta t_i = \Delta R_i / v_s$, where ΔR_i is the additional space that the signal has to travel to reach the i-th element [6].

If we call x_i the distance between the i-th element and the central one, it is possible to calculate ΔR_i as:

$$\Delta R_i = \left[\sqrt{R^2 + x_i^2} - R \right], \tag{3.17}$$

where R is the sphere radius, which is the distance between P and the central element.

When the signals from every element have been delayed, they can be summed to obtain the first scanline of the image. However, before doing this, apodization is commonly performed. It consists only in applying a Hanning window to the elements that form the scanline.

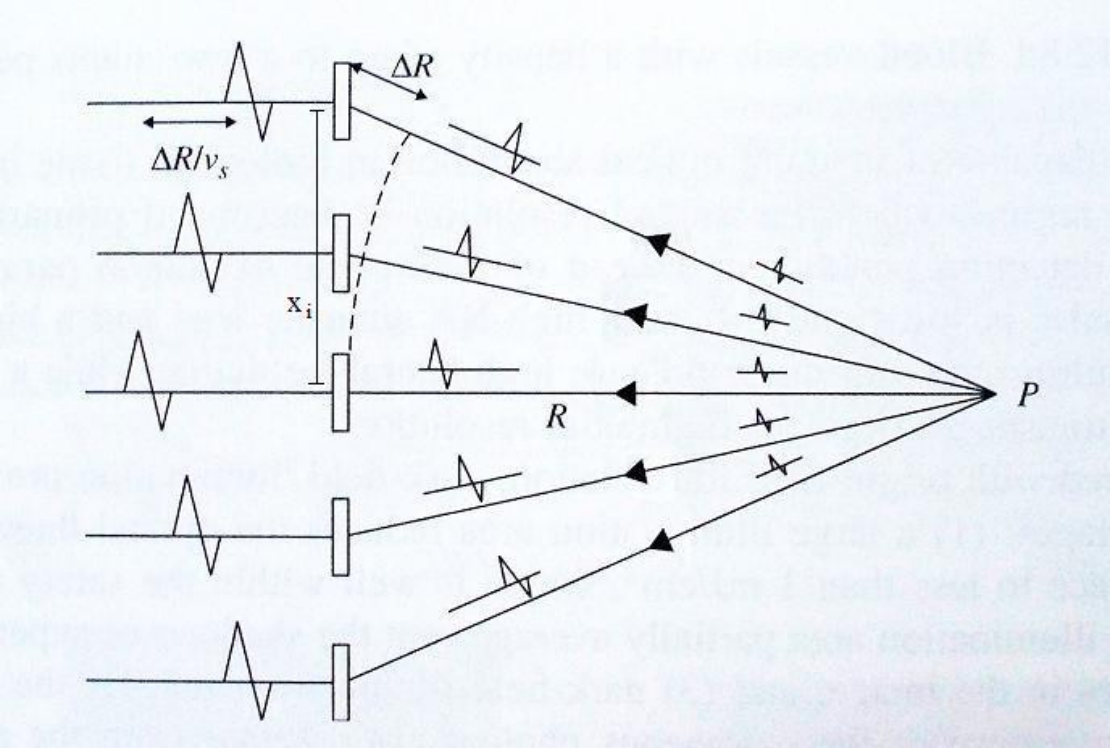

FIGURE 3.4: Signal detection from a point photoacoustic source.

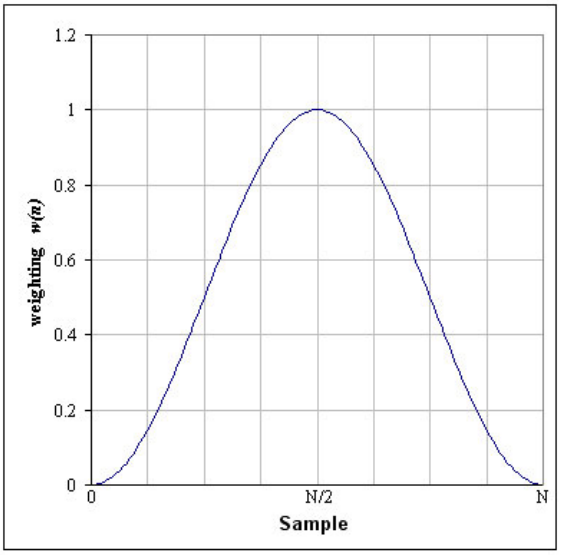

FIGURE 3.5: Representation of the Hanning window.

The Hanning window is shown in Figure 3.5, and its mathematical expression is:

$$W(n_i) = 0.5 \left[1 - \cos \left(\frac{2\pi n_i}{N} \right) \right], \tag{3.18}$$

where N is the total number of elements and n_i is the actual i-th element considered.

This allows us to give a bigger weight to central elements and a smaller one to elements that are distant from the center. This is done because far elements see better the signals that are generated from sources placed on their own axis and these signals can create strong artifacts.

As a result, the final expression of the elaborated and focused signal for the first scanline considered is:

$$S(t) = \sum_i W(n_i) S_i(t + \Delta t_i). \tag{3.19}$$

This procedure is then repeated, translating the scanline of one element, until all array elements have been considered. At this point, the image is made just by placing all the scanlines side by side. This is the procedure that is used within the project in order to elaborate the photoacoustic signals.

Part II

Chapter 4

Experimental Setup

4.1 Introduction

The present thesis, as mentioned in the beginning of Chapter 1, is a survey about the feasibility of a photoacoustic microscopy system, using a common commercial ultrasound scanner in order to recollect the acoustic data. All the work has been carried out at Lund University from March 2010 (actual start of the entire project) to September 2010. As a consequence, this work had to face all the problems and issues that arise when a brand new project starts from scratch, without previous knowledge of the subject.

Firstly, it was necessary to define the setup and to choose the most suitable components for both optical and acoustic parts. Secondly, the problem of triggering these two parts was considered. As a matter of fact, this was a non-trivial issue, due to the use of a common ultrasonic scanner for photoacoustic applications. As explained later in Section 4.4.1, the main deal was to take into account that photoacoustic waves travel only one time, from the source in the tissue to the ultrasonic transducer, while in ordinary echography signals travel back and forth from the transducer to the target.

After these steps, proper phantoms were chosen to characterize the system and to simulate tissue's optical and acoustic properties.

In the following Sections, all these aspects will be thoroughly described.

4.2 Optical Components

4.2.1 Laser

The laser source, used for photoacoustic wave generation, is a Quanta-Ray Nd:YAG laser, model DCR-2A(10). It emits light at $\lambda = 1064\ nm$, even if it can be changed, because the laser is equipped with a second, third and fourth harmonic generator (model HG-2). In particular, the green second harmonic (532 nm) is useful in order to reveal the capillary structure of tissues, because this wavelength is strongly absorbed by blood.

This laser works in Q-switching mode and it delivers 10 ns long light pulses, with a repetition frequency of 10 Hz. The beam profile is doughnut shaped, because of the disposition of the internal lamp that excites the active material. Though, this is not a big deal for photoacoustic generation, because the scattering uniforms the photon distribution as far as the light reaches the tissues. On the other hand, this homogeneous illumination could be a problem during data analysis, because it leads to a high background noise. In this case, as a matter of fact, also structures, which are not exactly below the transducer, can emit photoacoustic waves. They can be seen by the receiver as a diffused signal, because they are not focused. As a consequence, before applying the photoacoustic system to real tissues, it is important to evaluate the photon distribution in order to reduce the background signal [31].

With this laser, a wide range of values for the output power is available[1] thanks to an optical amplifier. Within the project, only a power of about 10 $mJ/pulse$ is used[2], because PAI techniques must respect the standard of the *American National Standards Institute* (ANSI) in order to be non-invasive. This standard sets the maximum allowable fluence to 20 mJ/cm^2 for pulsed lasers [32].

4.2.2 Optical Trigger Detector

In order to synchronise the data acquisition with the laser pulses, it is necessary to use an optical trigger detector. In the project an EG&G Princeton Applied Research, model 1301, is used.

It is able to generate an output signal of 3.5 V on 50 Ω. This is exactly what the ultrasonic scanner needs to be triggered.

A small amount of the whole laser light is delivered to the photodetector through a plastic fiber ($diameter = 600\ \mu m$), which is about 2 m long.

[1] Nominally the laser can reach 1.2 $J/pulse$.

[2] The spot size of the laser is approximately of 1 cm^2, so the laser fluence is about 10 mJ/cm^2.

4.2.3 Power Meter

In order to measure the optical output power of the laser, a Coherent Power Meter, model 120, is used. It measures the average output power. Knowing the laser *Pulse Repetition Frequency* (PRF), it is easy to find the average energy associated to one pulse. If the PRF is 10 Hz, as already mentioned, it is possible to calculate the average energy per pulse, by dividing the average power by 10 $pulse/sec$.

4.2.4 Other Optical Components

In order to build up the experimental setup, other optical components are used. In particular, a pair of metallic mirrors deflects the beam towards the sample. When green light is needed, these mirrors are substituted with two dichroic mirrors that reflect the green, but let the infrared light pass through them. To get rid of the remaining infrared light, a glass Schott BG 39 filter is also used and placed just after the two mirrors.

A beamsplitter is also used to send part of the laser light to the photodetector. It is just a thin piece of glass, so only 4% of the total light is reflected.

In addition, a set of neutral density filters is available to reduce the optical power when needed.

4.3 Ultrasonic Components

The commercial ultrasonic scanner, which is used in the project to analyse the acoustic data, is the Sonix RP system by Ultrasonix Medical Corporation, Canada. It is a software driven, ergonomic, diagnostic medical device, that uses state of the art technologies to acquire, process, and display ultrasound data [33]. The system, as shown in Figure 4.1, could be divided into four different parts: LCD display, console, ultrasound module, and transducers.

This scanner has a very high potential for adaptability and programmability. Indeed, it can be run in two different modalities. The first one is the *Clinic Mode*, in which standard ultrasonic B-mode images are shown on the screen. In this case, it is possible to choose the value of common parameters, like gain compensation, and to perform measurements on the images only through the console, without any research capabilities. The second one, instead, is the *Research Mode*, in which special parameters and customized imaging modes can be accessed from the Windows XP operative system, which is installed on the machine.

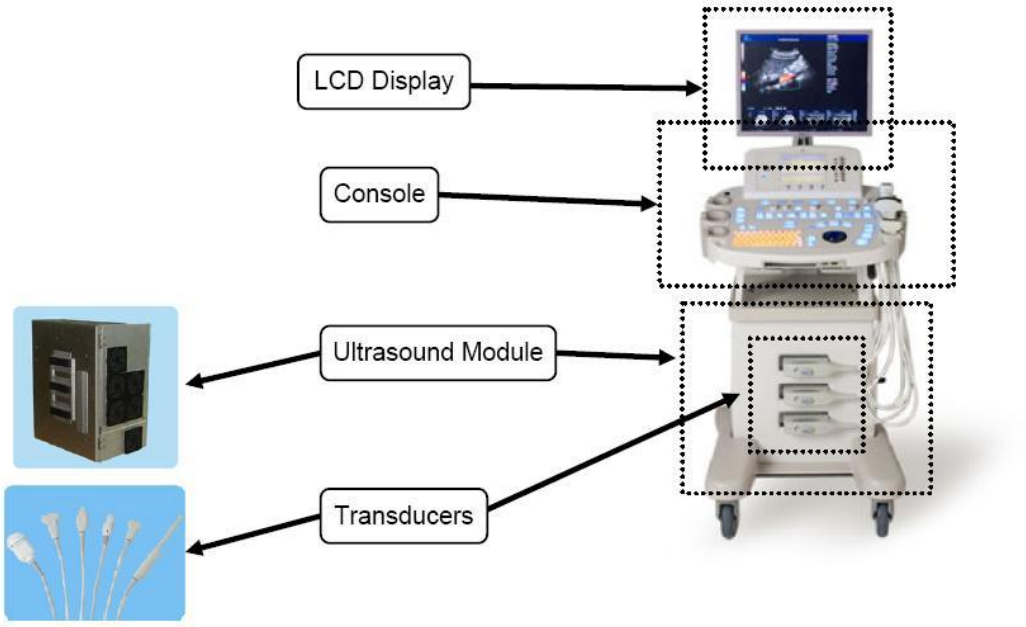

FIGURE 4.1: Overview of the Sonix RP system.

In the following sections, the different parts of the Sonix RP system will be described.

4.3.1 LCD Display

The monitor is an EIZO liquid crystal display. It is necessary to show the ultrasonic images when the *Clinic Mode* is activated, otherwise it shows the Windows XP Operative System, when the machine is run in the *Research Mode*. In order to switch from one mode to the other one, the button *"research"* must be pressed on the console.

4.3.2 Console

The console incorporates the controls necessary to interact with the scanner. They consist of a keyboard, a trackball, an array of push buttons, sliders, switches, and a little touchscreen for choosing the transducer and displaying information.

4.3.3 Ultrasound Module

The ultrasound module is the heart of the whole system. All boards and electronics are encased in it. These electronics consist mainly of 256 transmit channels, 32 receive channels, a cine buffer of 128 MB for data storage, and the *Central Processing Unit* (CPU)

of the computer.

4.3.4 Transducers

The Sonix RP scanner is able to support a wide variety of transducers. Within the project, the linear L14-5/38 (Ultrasonix) transducer is used. It is 38 mm long, with a nominal frequency bandwidth[3] of 5-14 MHz and an actual center frequency of 5 MHz. It consists of 128 piezoelectric elements, with a pitch[4] of 0.3048 mm.

This transducer is usually used for vascular, thyroid, breast, musculoskeletal, testicular, and superficial abdominal echography.

For the development of the PAM system, it is necessary to hold it perpendicularly above the sample, without moving it while a frame is captured. As shown in Figure 4.2, this is done by a suitable holder.

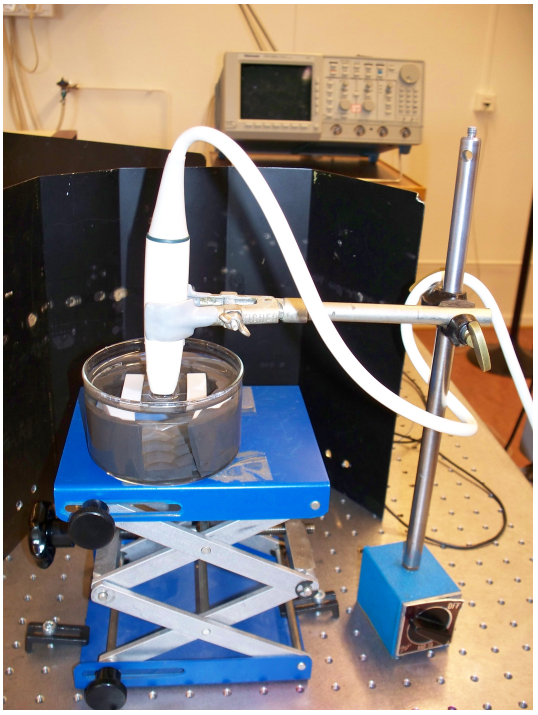

FIGURE 4.2: Transducer position above the sample.

[3]Actually, the Sonix RP scanner cannot deal with signals with more than 10 MHz frequency content. To know the real bandwidth of L14-5/38, if it is used in listening mode for photoacoustic applications, see Ref. [30].

[4]The pitch is the center-to-center distance between two adjacent piezoelectric elements. The smaller the pitch, the bigger the central frequency of the transducer, the better the system resolution[34].

4.4 General Setup

It is now possible to consider the general setup, in order to understand how the optical and acoustic components are bounded together. A simple sketch of the system is shown in Figure 4.3.

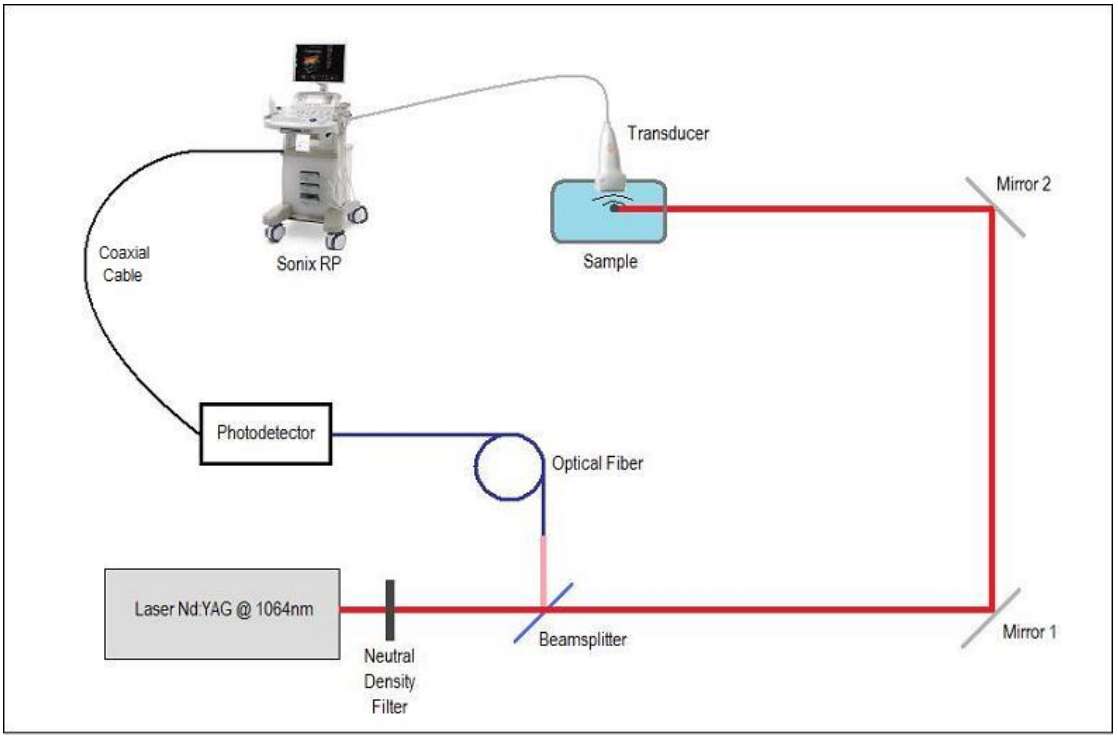

FIGURE 4.3: General setup of the photoacoustic microscopy system.

First of all, the infrared light ($\lambda = 1064\ nm$) is emitted from the laser and passes through a neutral density attenuator, which is characterized by an *Optical Density*[5] (OD) of 2.0, that corresponds to a transmittance of 1%. This filter is only used in the first experiments, in which the absorbing target in the sample is surrounded by water. In this case, as a matter of fact, the beam energy of 10 $mJ/pulse$ hits directly the target, without the attenuation caused by scattering and absorption of real tissues. In order to simulate this attenuation, according to the Diffusion Theory[6], it seems reasonable to use a reduction factor of 100 in the infrared light intensity, for a depth in the centimetre scale and typical μ_{eff} values for tissues[7]. The filter is needed because 10 $mJ/pulse$ is the minimum energy that the laser can emit, so it is not possible to reduce it in other ways.

[5] Optical density, or absorbance, is defined as $OD = -\log_{10}(I/I_0)$, where I is the transmitted intensity and I_0 is the incident one.

[6] As explained in Section 2.4, Eq. 2.33, the fluence rate (or intensity) for a time-indipendent point source, $S(x) = \delta(x)$, at depth x, is $\Phi(x) = (1/(4\pi Dx))\exp(-\mu_{eff} \cdot x)$.

[7] For the estimation, the following values are used: $\mu_{eff} = 3.55\ cm^{-1}$, $D = 0.05\ cm$, x =1-1.5 cm.

After the filter, a beamsplitter reflects a 4% of the laser intensity onto a fiber connected to the photodetector. As a result, the optical signal is converted in an electrical one, that is sent to the Sonix RP for triggering the data acquisition through a coaxial cable and *Bayonet Neill-Concelman* (BNC) connectors.

The main part of the beam passes through the beamsplitter and, thanks to two mirrors, it is reflected towards the sample. The generated photoacoustic waves are measured with the ultrasonic transducer, which is held above the emitting target, just below the water surface. Eventually, the light reaches a beam terminator, not shown in Figure 4.3, situated beyond the sample.

At this point, the Sonix RP recollects the raw data at each trigger impulse, for every single piezoelectric element, saving them in a particular file with ".rf" extension. These files can be opened by a customized Matlab routine, in order to make the images.

4.4.1 Triggering the Sonix RP Scanner

In order to let the whole system work properly, the trickiest part is about triggering the Sonix RP with the laser pulses. As explained in Section 3.4, there is a substantial difference between ultrasonic waves generated in US and in PAI.

In US, the waves are directly generated from the transducer. They travel into the tissue until they reach a portion with different acoustic impedance. At the separation surface they are backscattered towards the transducer. Measuring the time interval t between the sent signal and the echos that come back from the tissue, the ultrasonic scanner is able to calculate the distance d through the following simple formula:

$$d = \frac{1}{2} \cdot v_s \cdot t \tag{4.1}$$

where v_s is the speed of sound. Note that, due to the round trip, it is necessary to put a factor of 1/2.

If the signal travels only one way from the source (located in the tissue) to the transducer, like in PAI, the factor of 1/2 should be removed. As a consequence, if a common ultrasonic scanner is used, the final image is scaled and the target is displayed much nearer to the surface than its actual position.

Even if this problem seems simple to be solved, for example just by scaling the depth-axis dimension of the image, one must take into account that the signals need to be focused. As described in Section 3.5, the beamforming process needs to deal with right distances in order to apply the delay-and-sum algorithm correctly

So, instead of taking into account the scaling factor in all successive steps of data elaboration, it is convenient to change the way Sonix RP calculate the distances from echo signals. In order to do it, we need to write a customized executable for the machine.

As a matter of fact, the Sonix RP scanner has a special *Software Development Kit* (SDK), called Texo, that gives the user low-level control on data recollection. In order to write Win32 applications using Texo SDK, other two programs are needed. They are *Microsoft Visual C++ 2008 Express* and *Windows SDK for Windows Server 2008 and .NET Framework 3.5* [35].

The C++ code for using Sonix RP as a scanner in PAM, written within the project, is shown in Appendix A. It has been developed starting from the *"Texo Demonstration Program"* by Ultrasonix Medical Corporation, edited by Antony de Souza-Daw, which shows how to use Texo class and parameters.

First of all, it is necessary to put the transducer in a *listening* mode. To do it, the ultrasonic wave transmission must be turned off by setting a value of zero for the transmission power (line 90 in the code) and by choosing the *"zero pulse shape"* (line 255). As a result, when a trigger signal arrives, the scanner emits a null wave and interprets the coming echos as reflections of the null wave. Then, it measures distances in the standard way. It must be noted that the delay between the arrival of the trigger signal and the actual activation of the electric channels, that perform the measurement, is about 10 μs. This is a limit of the Sonix RP scanner, because in the image there is a black band of insensitivity for the first 1.5 *cm* just below the transducer[8]. This must be taken into account when realizing images.

In order to allow the scanner to be externally triggered, the corresponding instruction must be written in the beginning of the script. As shown in line 93 in Appendix A, the function `tex.setSyncSignals(int input, int output, int output2)` is used to record one scanline per trigger pulse. However, in this case, Sonix RP automatically applies an algorithm to focus the signals in each scanline. In order to avoid it, as we are interested in recording raw data without focusing them, it is useful to put a mask on all 128 elements of the transducer (line 269), in order to turn them off except for one. Then, at each trigger signal, the mask is shifted of one element per pulse (line 288 in the **for** loop).

As a result, to recollect one frame made of 128 vertical lines, one should wait 12.8 s, as the PRF of the laser is 10 Hz. So the system temporal resolution, in this case, is not very high. It is 0.08 $frames/sec$.

[8]The speed of sound used in the code, indeed, is 1540 m/s.

After all these steps, it is possible to take care of the 1/2 scaling factor problem. To solve it, one must change the formula, which the executable uses in order to make images. Unfortunately, this part of the code is not accessible, because it is embedded in a library ("Texo.dll" file) that Texo calls within the code. On the other hand, it is possible to set a parameter that directly enters in this formula. It is the speed of sound. As a result, instead of getting rid of the 1/2 factor in the formula, it is possible to multiply the speed of sound by a 2 factor (line 256). This leads exactly to the same result, as shown below.

$$c' = 2 \cdot c \tag{4.2}$$

$$d = \frac{1}{2} \cdot c' \cdot t = \frac{1}{2} \cdot 2 \cdot c \cdot t = c \cdot t \tag{4.3}$$

With these few considerations, it is possible to obtain rough RF data, that are stored in a particular format, with ".rf" extension. The created file contains a sequence of general information about the image, called header, followed by the values sampled by all piezoelectric elements, grouped in frames [36].

4.5 Phantoms

Phantoms are "ad hoc" designed objects that are scanned, in the field of medical imaging, to test, analyse, and calibrate the performance of the device. They are easier to be used than real tissues, and they do not expose the living subject to direct risk that could arise from wrong evaluations of the laser power or from unseen hazardous conditions. They can also be used as reference systems with defined values for the parameters of interest, since properties of real tissues can vary from one sample to the other.

These objects do not need to be identical to tissues in all their aspects. They must be similar only for the features that matter for the specific imaging technique.

For the present project aim, both optical and acoustic properties must be taken into account. Although, they will be considered separately. Indeed, the first phantoms used are only optical tissue-like samples, whilst the latter also possess acoustic tissue characteristics.

First of all, we have to choose a target that will simulate the inclusion or the inhomogeneity we want to image in tissues. It must absorb the light at the wavelength of the used laser. In the project, graphite rods with a diameter of 0.7 mm and 0.5 mm are employed as targets, because of their high absorbency for infrared light. Also a little glass capillary full of bovine blood is used as a target. Though, in this case, infrared

light will not be absorbed anymore. Green light, instead, must be sent into the phantom for generating photoacoustic waves.

Secondly, we need to surround the target with something that is able to transmit ultrasonic waves, but that does not absorb the light itself. The first choice consists in using water, because it is an excellent ultrasound transmitting medium and it has a relatively low absorption coefficient for the Nd:YAG radiation, as shown in Figure 4.4. It is only 0.4 cm^{-1}, that is even less than all other components of biological tissues. As a matter of fact, its peak of absorbency is located at a wavelength of 3000 nm.

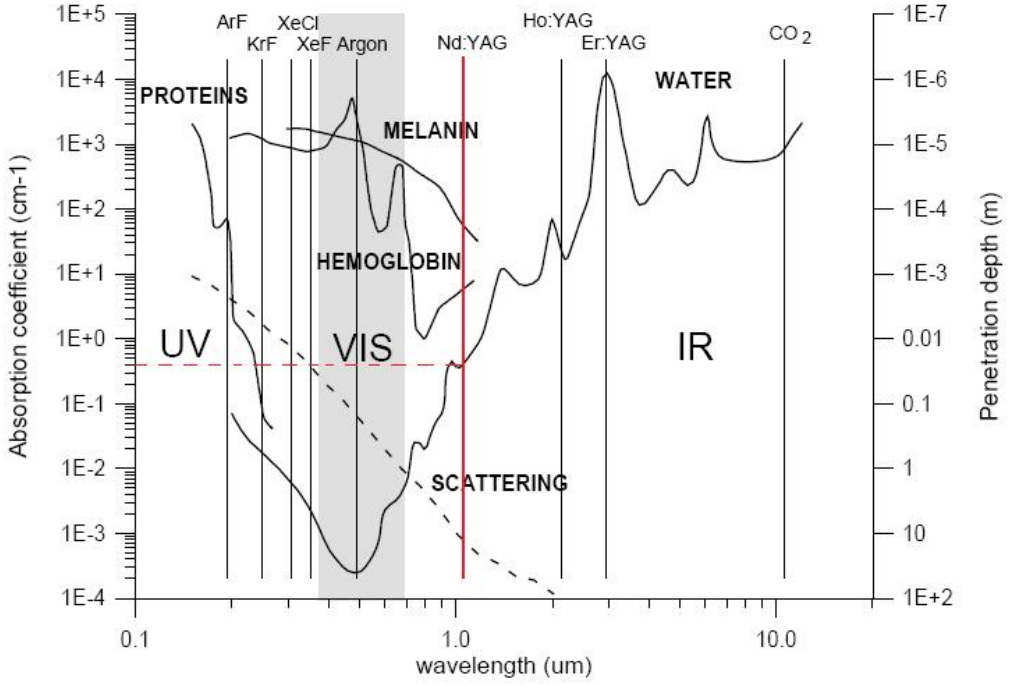

FIGURE 4.4: Absorption spectra of tissue principal constituents.

The problem is that water is very different from tissues from an optical point of view. That is why a mixture of water, intralipid, and black ink is also used in the experiments. Intralipid is a fat emulsion used as a component of intravenous nutrition in hospitals for patients that are unable to assume food directly. This emulsion is composed of soy bean oil, egg phospholipids, and glycerin. It is suitable to make optical phantoms, because it is a highly scattering suspension with low absorption [37]. In order to change the absorption characteristics of the phantom, instead, normal black ink is used.

For the project, a 200 mg/ml Fresenius Kabi (Uppsala, SE) Intralipid©, and Pelikan fount India (1:100) ink are used. The used quantities for each component are shown in Table 4.1.

Component	Quantity
Water	1000 ml
Intralipid	41.7 ml
Ink	3.1 ml

TABLE 4.1: Quantities of components used in the experiments to make liquid phantoms.

With this recipe, the liquid phantom has the following values for principal optical parameters[9]: $\mu_a = 0.7\ cm^{-1}$, $\mu_s' = 5.8\ cm^{-1}$, $\mu_{eff} = 3.6\ cm^{-1}$. In this case, as in real tissues, laser light is principally scattered after entering the phantom, so it is possible to test the sensitivity of the technique as a function of depth.

Lastly, in order to take into account also acoustical properties of tissues, some other phantoms are made with ex-vivo animal biological material. In particular, beef flesh is used in the project for this purpose.

Note that, in this case, it is necessary to use the ultrasonic coupling gel between phantom and transducer surfaces to avoid the big interface reflection. Otherwise the piece of meat to be imaged could just be immersed in water.

[9]Measurements refer to a wavelength of 975 nm.

Chapter 5

Experimental Characterization of the System

5.1 Introduction

When a new system is built up, it is important to test and characterize it, in order to understand its limitations and advantages. Indeed, this characterization constitutes the main endeavour of this thesis work.

Before doing this, though, it is necessary to create a software capable of processing raw photoacoustic data, enabling the user to display them on the computer. For this purpose, the software Matlab® was used in order to write algorithms and to customize a *Graphical User Interface* (GUI) already written to analyse RF raw data.

Once the elaboration process is defined, it is possible to proceed with a set of experiments to see how the system behaves in different imaging conditions. They can also help in evaluating some important performance parameters, like *Signal to Noise Ratio* (SNR), sensitivity, selectivity, and axial and lateral resolutions.

5.2 Data Elaboration Software

As mentioned in Section 4.4.1, data are stored by Sonix RP in particular ".rf" files. These files have a specific structure that must be changed in order to make proper images. As a consequence, Ultrasonix Medical Corporation released[1] a Matlab GUI,

[1]The Ultrasonix Medical Corporation website is http://research.ultrasonix.com/.

which is designed to get the most common ultrasonic information out from stored data. Its name is *"GraphicUnit_export"*. A screenshot of this GUI is shown in Figure 5.1.

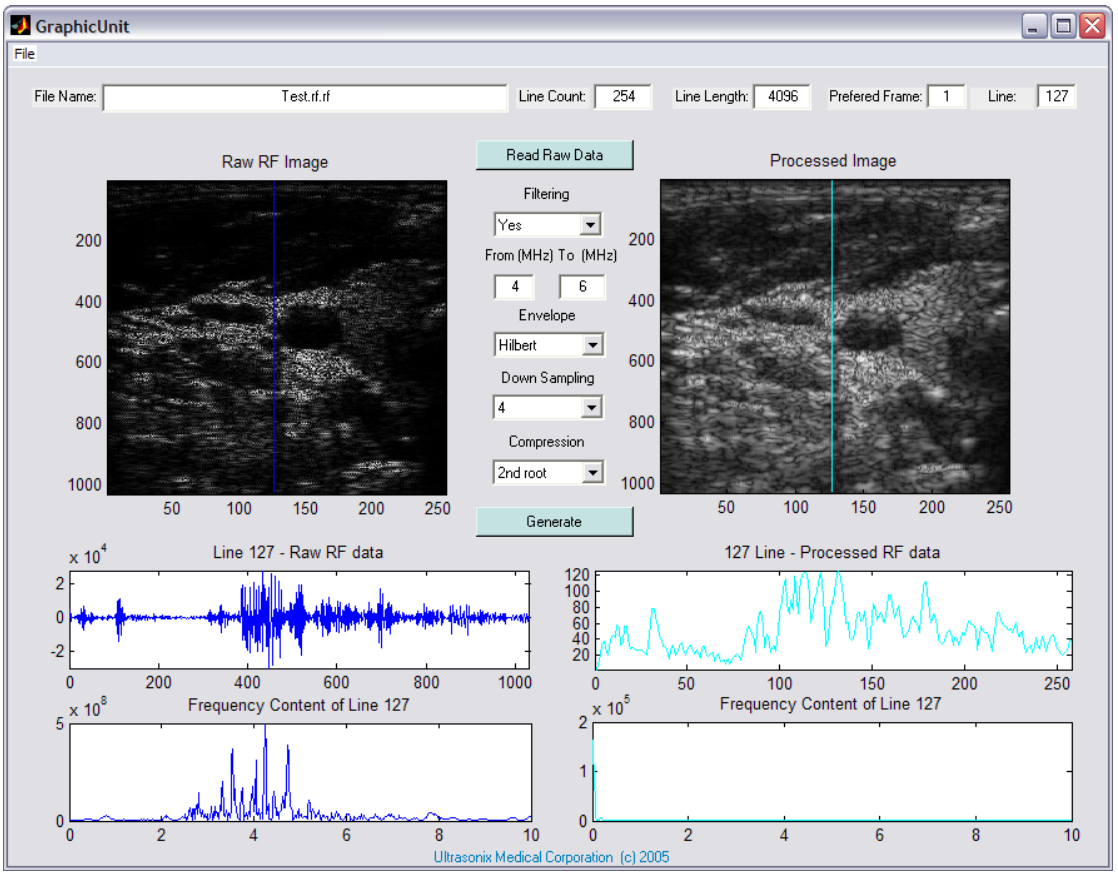

FIGURE 5.1: "GraphicUnit_export" interface screenshot.

In the upper part of this GUI there are some boxes: the first one is to choose which file will be opened; the second and third ones display the width and the depth of the image in pixels, respectively; the last two boxes, instead, can be used to select the shown frame and the highlighted line.

Under these boxes, two B-mode images are presented: the left one contains the raw RF data directly taken from the ".rf" file and displayed as they are; the right one, instead, is the elaborated image. This arrangement is helpful to understand if the elaboration is successful in improving the image. Between them, a set of parameters can be chosen to operate the most common elaboration actions on ultrasonic images. It is possible to filter signals in frequency and to perform envelope detection before imaging. Two kinds of envelopes are available: Hilbert and absolute. The Hilbert one applies the Hilbert transform that is generally used in signal processing to derive the analytic representation of a signal. Due to its properties, indeed, it can also be used in making amplitude envelope filters [38]. On the other hand, the absolute one takes only the absolute value of the RF signal.

In addition, it is also possible to apply down sampling and compression algorithms. Down sampling is the process in which the sampling rate is reduced. The integer factor of downsampling is used to find the new sampling rate, that is just the original rate divided by that factor. As a result, the data size decreases. Compression, instead, is a way to change the displayed range of signal values. It can be a logarithmic or an n-root compression. This could be helpful, because received acoustic signals can have amplitudes that vary over many orders of magnitude.

Just below the two principal images, there are four small graphs. The upper ones are A-mode images that show the RF signal of the highlighted line in the correspondent B-mode image. They can be used to evaluate the SNR associated to the ultrasonic or photoacoustic echos. The other two graphs display the spectrum of the highlighted line, that is its frequency content.

However, in order to make this GUI suitable for photoacoustic applications, some changes are introduced. First of all, the units of the vertical axes of the two B-mode images are converted from pixels to millimetres. In this way, it is easier to see where the target is located under the transducer. For this aim, it is useful to know that the sampling rate of the transducer is 20 MHz. Knowing the speed of sound (1540 m/s in tissues), it is possible to calculate how many micrometres are associated to one pixel. That is :

$$\frac{Speed\ of\ sound}{Sampling\ rate} = \frac{1540\ m/s}{20\ Mpixel/s} = 77\ \mu m/pixel$$

The units of the horizontal axes are changed as well. In this case, as every pixel is a piezoelectric element, the converting factor is just the distance in micrometres between adjacent elements (given by transducer specifications) per pixel, that is 304.8 $\mu m/pixel$ in our case.

In the four small graphs, placed at the bottom, the units of the vertical axes are not changed, because they are arbitrary units. They are just the amplitudes of acoustic signals received by the transducer after gain compensation, analog to digital conversion, and, in the right two graphs, also beamforming, apodization and all elaboration processes.

Beside these small modifications, a specific code for signal focusing, written within the project, is implemented in the GUI. It is based on the delay-and-sum algorithm described in Section 3.5. As the source code for the GUI is very long and built up by several different functions, in Appendix B only this focusing function, called *"beamforming"*, is shown.

In order to describe the code, it is necessary to say that every scanline of the final image is made by beamforming, apodizing, and summing 32 columns of the original image matrix. As a consequence, firstly, a submatrix of 32 columns is extracted from the matrix, say columns from 1 to 32 (in the code, see line 34). Secondly, the delays for each element of the matrix, calculated according to Eq. 3.17 in Section 3.5, are applied for the desired focus depth. This consists in shifting the elements of a column in an upper position (line 35). The bigger the distance from the central column, the bigger the delay, the bigger the displacement of the elements. Thirdly, apodization is made by multiplying the signal matrix with an apodization matrix, which contains, on each row, an hanning vector (line 37). This vector is created by the function `hanning(Num_of_elements)` and it gives a unitary value to the central element of the row and smaller ones while approaching the edges of the vector (line 20). Lastly, all elements in each row of the obtain matrix are summed to yield a single column vector (line 38). This is the first scanline of the final image. The whole process is then repeated for another submatrix, one column shifted with respect to the previous one, for example choosing columns from 2 to 33, and so on.

At the end of this process, the elaborated image has a smaller width, because 32 elements are lost in the average procedure. In addition, this algorithm allows only fixed focusing at a specific depth. As a consequence, it is necessary to adjust this depth for every image, depending on the target position.

Finally, also the *zoom* function is added to all images, to give the user a better evaluation of target dimensions or of the fine structure of signals.

5.3 Experiments

5.3.1 Single Graphite Rod in Water

The very first experiments are performed with a single graphite rod with a diameter of 0.7 mm. This rod is surrounded by water and it is fixed, with two erasers, at a distance of 2.5 cm from the transducer. A round glass bowl, coated inside by black rubber, is used to contain the sample. The erasers and the rubber are employed to avoid artifacts from specular reflections of the photoacustic waves on the glass walls. As a matter of fact, rubber is able to damp the ultrasonic waves.

Infrared laser light pulses ($\lambda = 1064\ nm$, pulse length = 10 ns, repetition rate = 10 Hz, and average energy = 0.1 $mJ/pulse$) are sent laterally to the sample and they hit the rod.

Point-Like Source Configuration

In order to simulate a point-like photoacoustic source, the transducer is orthogonally positioned above the rod. A photo of the sample, with a superimposed sketch of the laser light and the transducer position, is provided in Figure 5.2.

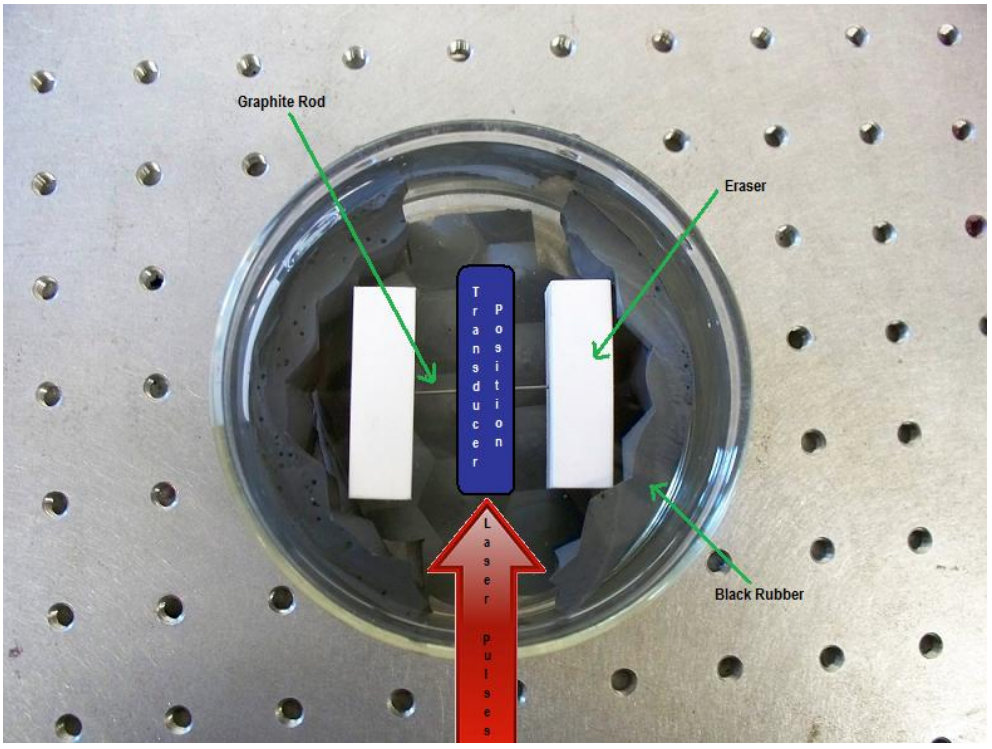

FIGURE 5.2: Photo of the first sample, with explanation of components. The transducer position and the incoming laser light are also shown.

This first phantom is very simple and it has been used a lot to understand how the Sonix RP scanner works. Moreover, it is useful to see how changes in the code improve the final image and the GUI behaviour. The corresponding images are not shown in this thesis, but they led to the optimum setup of parameters in the Texo code presented in Appendix A.

After all the settings and the elaboration processes are chosen, it is possible to obtain the image shown in Figure 5.3. On the left side, raw data are presented, with the characteristic curved shape due to different paths that the signal has to travel before reaching the specific transducer element. Note that the signal is stronger on the right side of the curve, because that is the direction from which the laser light comes. As a result, the rod's face directly exposed to light expands greater than the opposite one.

The black insensitivity band, due to a 10 μs lag between the trigger pulse and the channel activation, as described in Section 4.4.1, is evident in the image. The edge of this band,

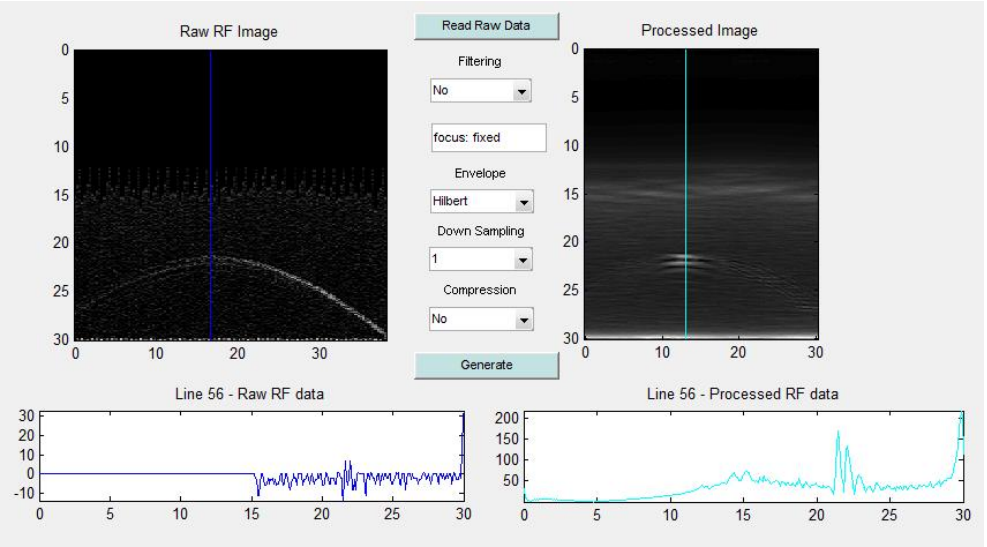

FIGURE 5.3: Photoacoustic images obtained from the single graphite rod in point-like source configuration.

around 15 mm, is comb-shaped, because the channels are electronically multiplexed to make the image. As a matter of fact, for some channels, the electrical delay is slightly bigger.

On the right side of the same figure, there is the beamformed image, with the focused signal. The bright spot appears at 22 mm, instead of the actual position of 25 mm, because the electronic circuits in the Sonix RP scanner start to collect data 2 μs after the trigger signal arrival. However, it is possible to directly compensate this problem by shifting the axes position. In all successive figures, this solution is implemented. For practical reasons, it is not feasible to delay the laser light by 2 μs, because it would need about 600 m of fiber optic.

The rod, in the elaborated image, is represented by two parallel lines that correspond to its upper and lower surfaces. They can be separately seen because the axial resolution is less than 700 μm. Indeed, it should be around 300 μm, as can be inferred by looking at the *Full Width at Half Maximum* (FWHM) of the corresponding peaks in the RF line signal. When the axial dimension of the target is comparable to the resolution, not only the two surfaces are displayed like a single bright spot (see Figure 5.7), but the RF signal changes also its features [30]. In Figure 5.4, two closeups, one of the rod and one of the two RF peaks respectively, are shown.

However, lateral resolution is quite poor, because it is at least 4 mm, as it is possible to infer from Figure 5.4. This is principally caused by the finite transducer aperture, that prevents from focusing with more than 32 elements per scanline, in order to maintain a reasonable number of scanlines per image. As a matter of fact, an infinite aperture

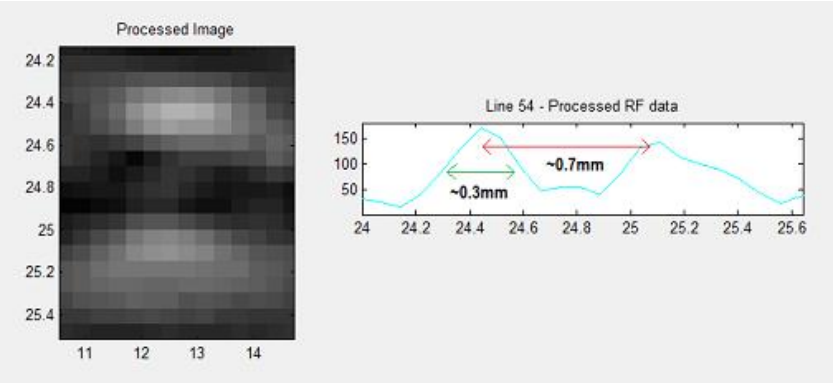

FIGURE 5.4: Closeups of single rod's signals. On the left there is the zoom of the B-mode image, while, on the right, there is the zoom of the RF signal.

would allow a perfect reconstruction of the rod. As a matter of fact, one can see without blurring only those parts of the target interfaces that can be tangentially touched by spheres, which are centred at the detector positions [39]. A possible solution consists in translating the transducer, but this is outside the scope of this research work.

Parallel Configuration

The second experiment is meant to show how the signal changes if the photoacoustic source is not a single emitting point. To accomplish this purpose, a parallel configuration is used. This means that, with respect to the previous case, the transducer is rotated by 90 degrees. As a result, it is positioned above the rod, exactly in the same direction.

In order to detect the acoustic wave, in this case, it is necessary to align perfectly the transducer with the rod. As a matter of fact, the ultrasonic detector has a quite narrow field of view and it is not able to reveal signals coming from the sides, which only contribute to the background signal. As a result, before performing the experiment, the common echography modality for the Sonix RP scanner is used, in order to place the transducer in the right position.

The result of the trial is shown in Figure 5.5. In the elaborated image it is possible to see the rod in its length, even though two spots are brighter because the doughnut-shaped laser beam hits the rod directly and it causes a stronger emission from these points.

In order to see the whole rod, the target illumination should be homogeneous. To achieve this result, a little quantity of intralipid can be poured in water and the phantom can be settled to let the laser beam pass just over the graphite rod. As a consequence, the target is now only hit by the light that is scattered because of the intralipid. To perform this measurement, the neutral density filter is removed from the setup, as the scattered

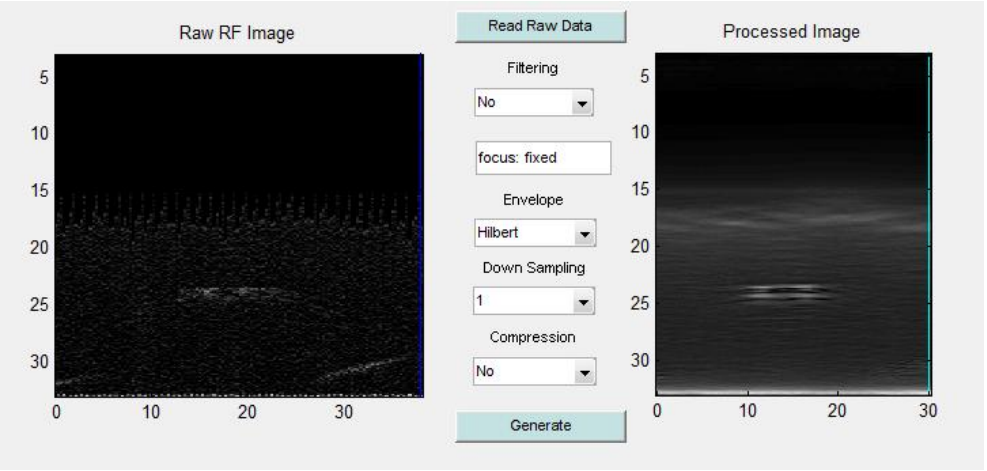

FIGURE 5.5: Photoacoustic images obtained from the single graphite rod in parallel configuration.

light is only a little fraction of the total intensity and more power is needed to generate the photoacoustic wave.

The corresponding signal, collected with the transducer, is shown in Figure 5.6. It is possible to see that the rod expansion generates a sort of planar wave front, that hits all elements of the transducer surface at the same time. This is reasonable, because the photoacoustic wave, generated from the rod, should have the same cylindrical symmetry.

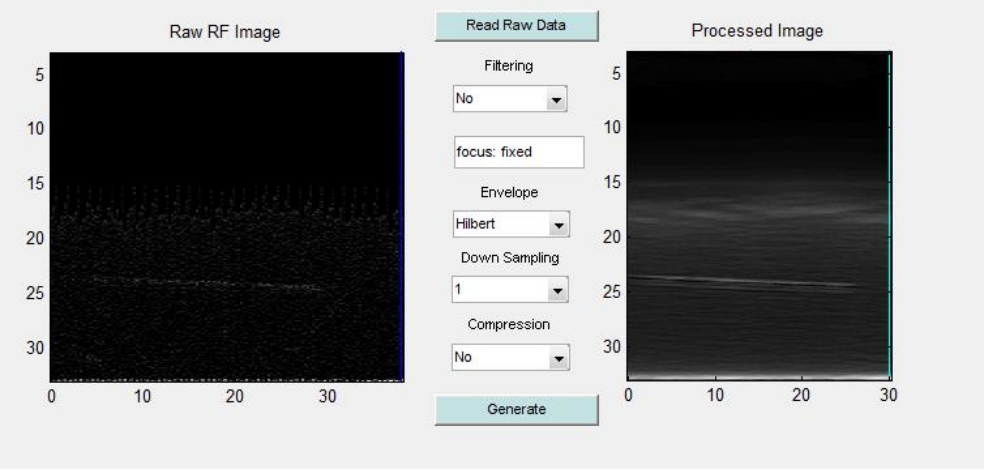

FIGURE 5.6: Photoacoustic images obtained from the single graphite rod in parallel configuration with homogeneous illumination, accomplished by the use of intralipid.

Again, both rod surfaces are visible in the image, even if the upper one is much more intense than the lower one.

Signal From a Thinner Rod

Using a thinner rod as a target allows us to understand how the signal changes, if the dimension of the photoacoustic source can be compared with the system resolution.

In the following experiment, a graphite rod with a diameter of 0.5 mm is used. In order to get the difference between this case and the one involving the thicker rod, the point-like source configuration is assumed.

The measurement result is shown in Figure 5.7. It is possible to see that now, after the elaboration, the rod is displayed like a single bright spot and it is no longer possible to distinguish its two surfaces exactly.

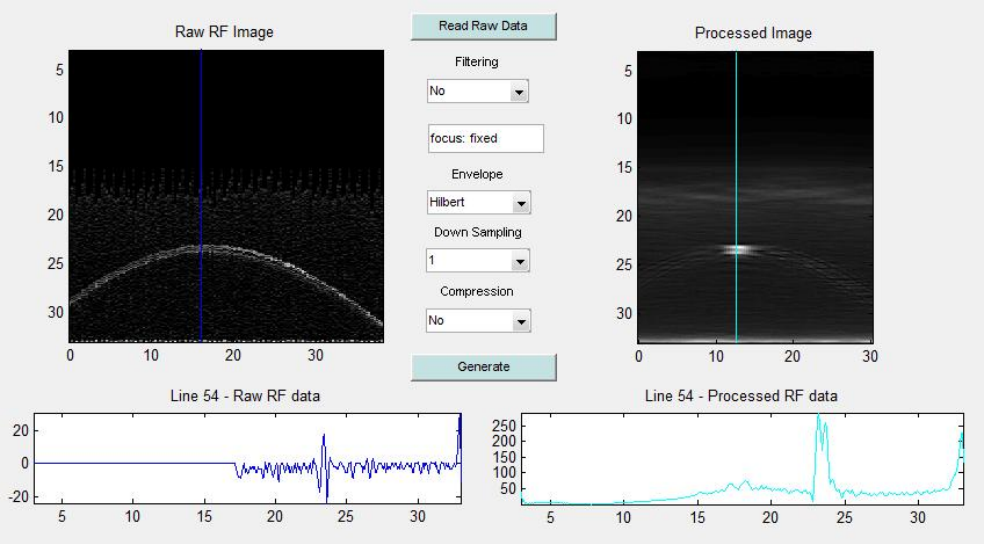

FIGURE 5.7: Photoacoustic images of a rod with a diameter of 0.5 mm.

In the RF signal, in this case, there is only one big peak with two spikes on its top. These spikes are visible because the resolution, as mentioned before, is estimated to be around 300 μm.

5.3.2 Two Graphite Rods in Water

In order to further test the lateral resolution of the system, another phantom is created. It is made of two graphite rods with a diameter of 0.5 mm. They are always held by two erasers and they are arranged in order to form a cross, as shown in Figure 5.8. In this way, one can place the transducer just above the point where the rods overlap each other and then move it away from the centre, until the rods are displayed like two individual spots.

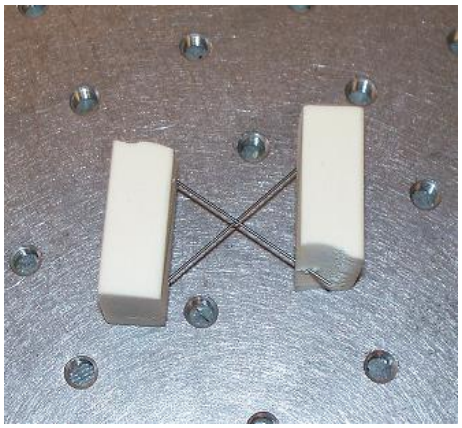

FIGURE 5.8: Photo of a phantom consisting of a cross formed by two graphite rods.

The actual position of the rods is measured with the standard echography modality of the Sonix RP scanner. To allow a uniform illumination, some droplets of intralipid are poured in water and the laser power is increased as well by removing the neutral density filter. Indeed, scattering is needed because, otherwise, the first rod hides the second one with its shadow, if the collimated laser light is directly delivered to the phantom.

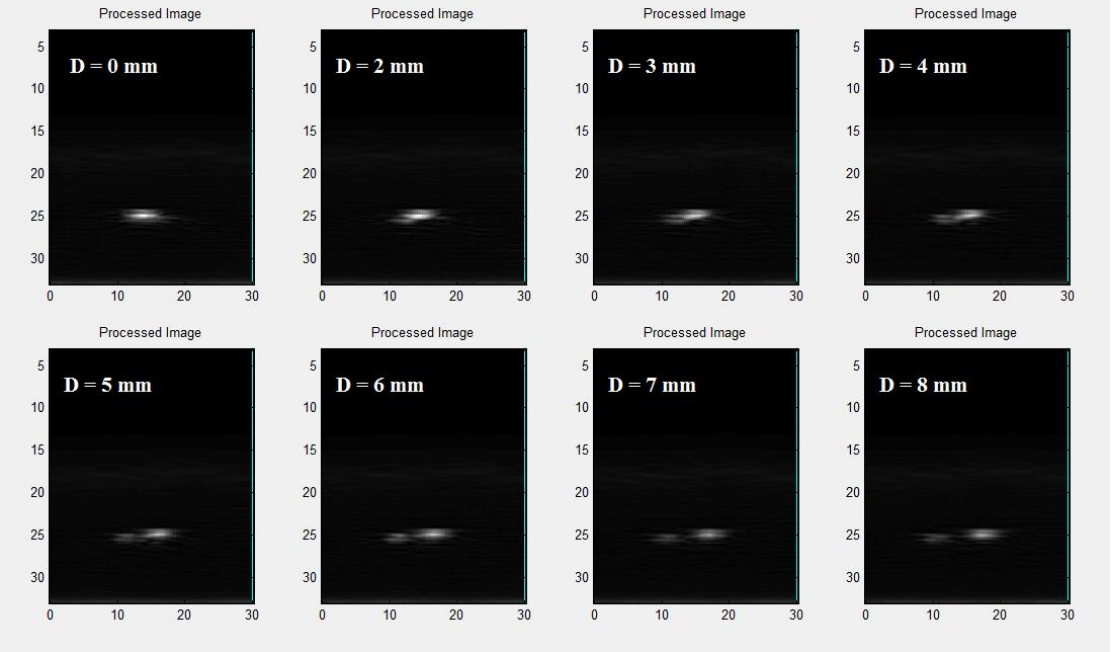

FIGURE 5.9: Elaborated images of two graphite rods in water. The actual displacement between the rods is indicated for each image and it is measured with the standard ultrasonic modality.

In Figure 5.9, many processed images of the two rods, with the corresponding distance between them, are shown. It is possible to see that they can be individually resolved

only after their relative distance has reached, at least, 4-5 *mm*. This is coherent with the results of the very first experiment.

5.3.3 Optical Tissue-Like Phantoms

So far, only the general behaviour of the Sonix RP scanner in photoacoustic applications and its resolution have been investigated with simple phantoms, which are very different from real tissues. Conversely, the next few experiments are performed involving phantoms that share some properties with the same biological media which the system is supposed to deal with, after the first phase of development and characterization, described in the present thesis.

The first phantom of this kind, used to test SNR, sensitivity and selectivity of the imaging setup, has only optical tissue-like features. It consists of a target, properly chosen in function of the used wavelength, embedded in the liquid mixture, which is made up by water, intralipid and ink, as described in Section 4.5. See Table 4.1 to know the exact quantities of the involved components.

The bowl used to hold the liquid is shown in Figure 5.10. It is a rectangular plastic container, in which two small erasers are glued to the surface from which the laser light enters. A millimetre scale is drawn on the erasers, in order to precisely know the distance between the target and the surface.

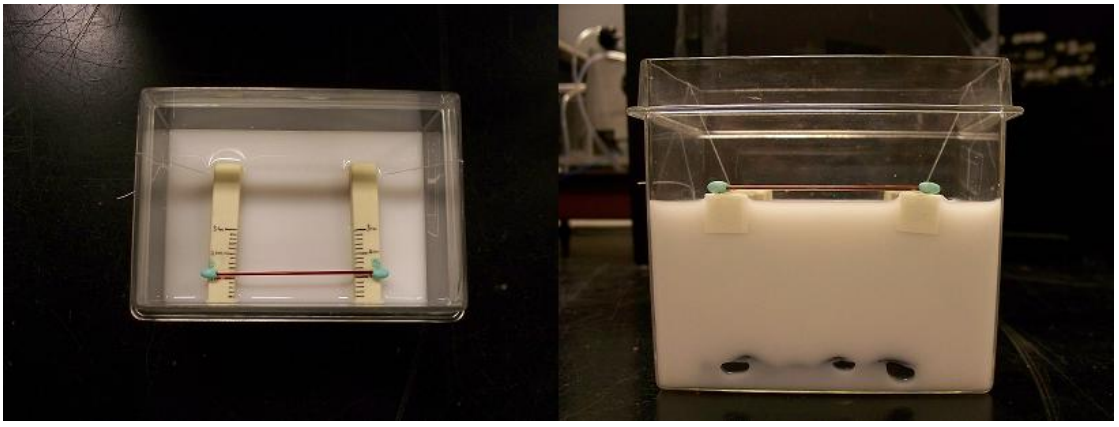

FIGURE 5.10: Top view (left) and lateral view (right) of the second bowl used to contain the liquid phantom. The graded erasers, the liquid mixture, the black rubber on the bottom and the blood-filled capillary used in the experiments can be seen.

Two kinds of targets are used for different purposes with this phantom: a graphite rod and a blood-filled capillary. The former is employed to study the system sensitivity as a function of depth by evaluating the SNR, while the second is useful to characterize the technique selectivity by switching the excitation wavelength.

Note that, from now on, the neutral density filter is definitively removed, because we deal with phantoms that have similar optical properties to tissues. As a result, the laser energy, sent to the sample, is always of 10 $mJ/pulse$.

First Target: Graphite Rod

The first experiment, performed with a graphite rod with a diameter of 0.7 mm as a target, is made to test the maximum penetration depth that can be reached in tissues, if the laser power is kept below the threshold required by the ANSI standards.

The trial consists in placing the rod at 1.1 cm from the lateral surface of the bowl and moving it deeper and deeper with steps of 2 mm each, until the signal disappears or the SNR is too low.

The transducer is orthogonally placed with respect to the rod and this also explains why the rod is placed at 1.1 cm. As a matter of fact, if the transducer is held in contact with the lateral wall of the container, it cannot reveal the target unless it is at least 1 cm away from the surface. This is due to the shape of the detector. It is not possible to tilt it toward the surface to see closer, because the plastic wall emits itself photoacoustic waves that spoil the image.

The measurement results are shown in Figure 5.11. The illuminated surface corresponds to the right edge of the images. The signal and the noise amplitudes can be inferred by the RF data placed under each picture.

In order to calculate the SNR, expressed in decibels, the following formula is used:

$$SNR|_{dB} = 20 \log_{10} \left(\frac{Y_s}{Y_n} \right) \tag{5.1}$$

where Y_s is the signal amplitude, measured as the mean value of the two peaks in the RF signal, and Y_n is the average value of the background signal, which can be seen as a noise that is superimposed to the whole image, because it is present even if no laser light is delivered. Note that Y_n, evaluated from the elaborated RF signals, is a constant value that corresponds to 40 a.u. for every measurement.

SNR values, for each measurement, are shown in Table 5.1. Looking at it and surveying the images, one can infer that the maximum depth is about 2 cm, as the signal starts to fade after 19 mm.

Observe that, at $D = 13$ mm, the SNR is about 3.4 times bigger than its value for $D = 21$ mm. The fact that the SNR at $D = 11$ mm is lower than the one at $D = 13$ mm

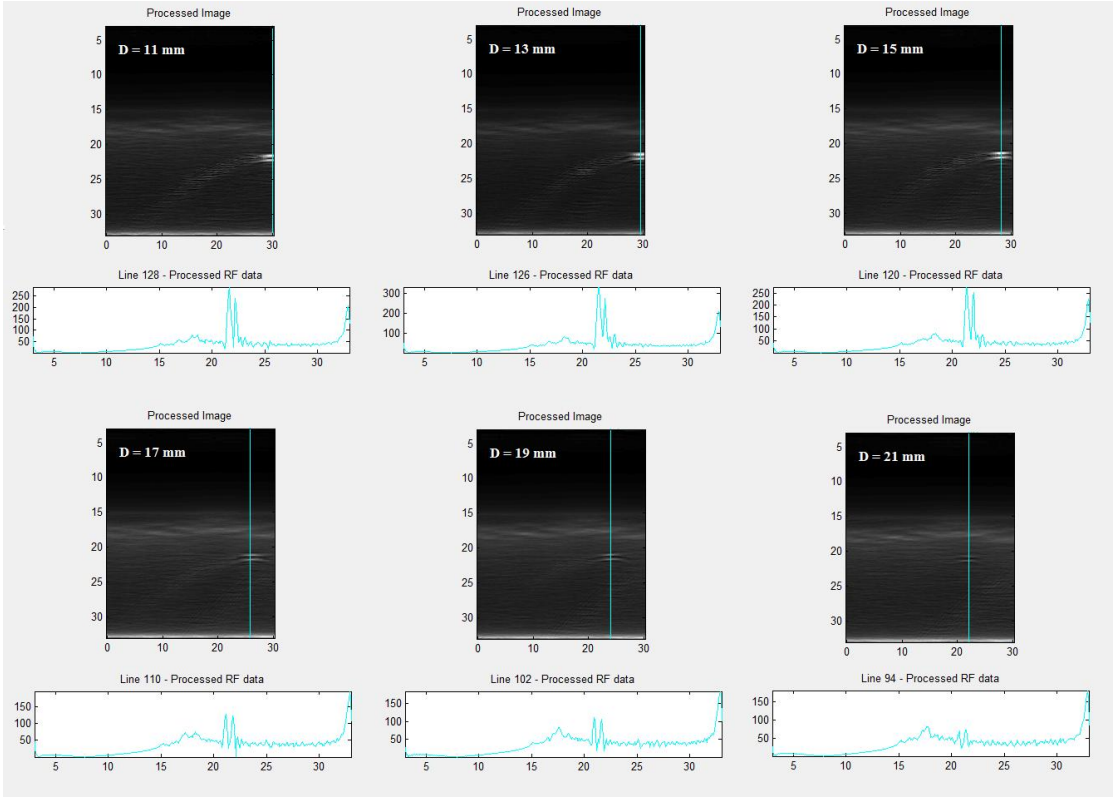

FIGURE 5.11: Pictures of a graphite rod in intralipid. The distance D from the illuminated surface of the container is indicated in every image. Note how the signal amplitude decreases as the distance becomes bigger.

D	Y_s(a.u.)	$SNR\|_{dB}$
11 mm	265	16.4 dB
13 mm	295	17.4 dB
15 mm	260	16.3 dB
17 mm	125	9.9 dB
19 mm	108	8.6 dB
21 mm	72	5.1 dB

TABLE 5.1: SNR associated to different target depths in liquid phantoms. D is the distance between the target and the illuminated surface, while Y_s is the mean value measured for the signal at that depth.

can be explained by noting that the bright spot position is in the very edge of the corresponding image. As a consequence, part of the signal is lost, because it is not seen by the transducer.

Second Target: Blood-Filled Capillary

The second target, used within this liquid phantom, is a glass capillary filled by bovine blood. Its internal diameter is about 0.5 mm, while the external one is about 1.5 mm.

Its edges are sealed with blue soft rubber (see Figure 5.10). It is useful to test the system selectivity, that is its capability to separately image objects, which absorb at different wavelengths. As a matter of fact, blood is able to absorb green light, whilst only a negligible amount of infrared light is absorbed.

In order to be sure that the target is exposed to a sufficient radiant energy for generating photoacoustic waves, it is positioned at 12 mm from the illuminated surface. Two images are then taken, the first one by using light at 1064 nm and the other one with light at 532 nm. Before starting each experiment, the laser power is measured to be sure that it corresponds to 10 $mJ/pulse$ for both wavelengths. The results are shown in Figure 5.12.

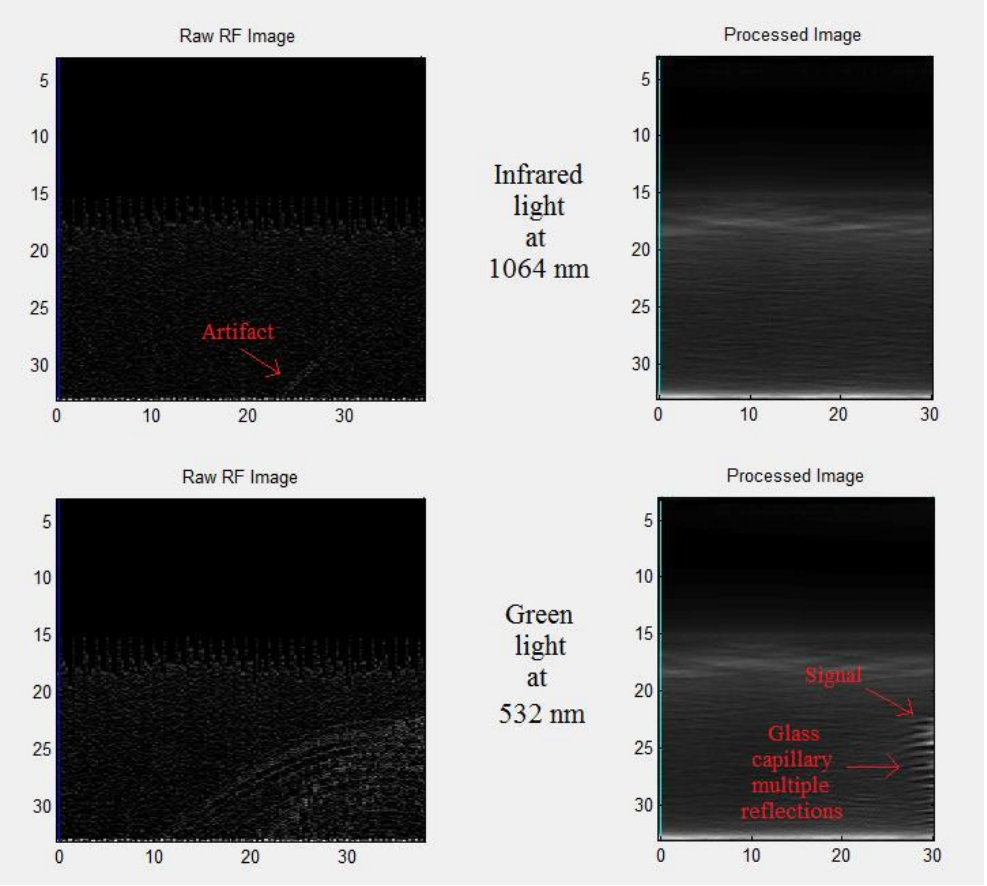

FIGURE 5.12: Raw and processed images of the blood-filled capillary in intralipid. The two images on top are obtained shedding infrared light, while the other ones are obtained with green light. The illuminated side corresponds to the right edge of the images.

As can be seen, with the infrared light, the signal from the blood is not present. In fact, in the raw image, there is a very small signal that comes from the plastic walls of the container, but it disappears when the beamforming process is applied. This is because it comes from outside the tissue placed under the transducer and cannot be focused. On the contrary, with the green light, the blood emits strong photoacoustic waves that can

be seen in the very right edge of the corresponding image. The associated SNR, in this case, is 11.5 dB.

Note that a lot of artifacts are generated by the glass which the capillary is made of. This phenomenon is due to the multiple reflections that take place at the glass interfaces. The photoacoustic waves, generated inside the capillary, indeed, are continuously reflected back and forth from its walls. As a matter of fact, the same artifacts are present in the standard echography modality, that is used to measure the actual vertical position of the capillary, which is 23 mm in the present experiment. As can be seen, this is the position from which the signal starts to be present in the photoacoustic image. Figure 5.13 shows the presence of artifacts, due to the multiple reflections, in the standard ultrasonic image.

FIGURE 5.13: Ultrasound images of the blood-filled capillary in intralipid. Note the presence of artifacts under the capillary.

5.3.4 Experiments with Animal Tissues

After having investigated the behaviour of the PAM system with phantoms that share similar optical properties with human tissues, it is now possible to use animal tissues, that also have the same acoustic features.

Animal Tissue with Graphite Rod

The first experiment with real tissues is made in order to understand the differences between normal ultrasonography and photoacoustic imaging. In particular, it is possible

to show how different the contrast can be, for a target embedded in biological media for these two imaging systems.

The first used sample is shown in Figure 5.14. It is made of a piece of porcine meat, in which a graphite rod with a diameter of 0.5 mm is inserted.

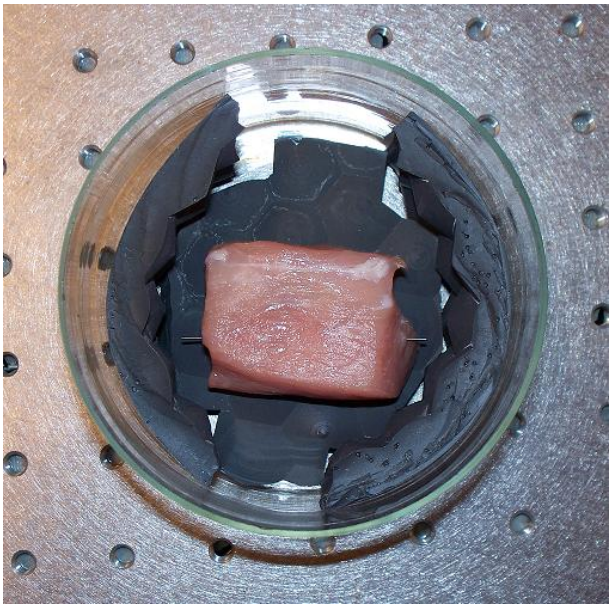

FIGURE 5.14: Photo of the sample made with a piece of porcine meat. The edges of the graphite rod are visible.

The width, the depth, and the height of the parallelepiped are approximately 40 mm, 30 mm, and 15 mm respectively. The rod is inserted at one third of the depth and at 5 mm from the upper surface. As a result, it is possible to perform two measurements: the first one is done with a distance of about 10 mm between the rod and the illuminated meat surface; the second one is performed by shedding light on the opposite side, obtaining a distance of 20 mm.

Infrared light with $\lambda = 1064$ nm and energy of 18 $mJ/pulse$ is used. The laser power increase is due to some fluctuations in the exciting lamp intensity, but it can be used, as far as the energy value is below the ANSI limit.

Before starting the experiment, a normal ultrasonic image of the sample is taken. As shown in Figure 5.15, the ultrasonic scanner is not able to distinguish the graphite rod from the surrounding tissue. This means that the contrast between the inclusion and the normal tissue can be very low, even in case of very different materials from the optical point of view. This comes from the fact that, from an acoustic point of view, graphite and soft tissue share similar properties, like density and compressibility.

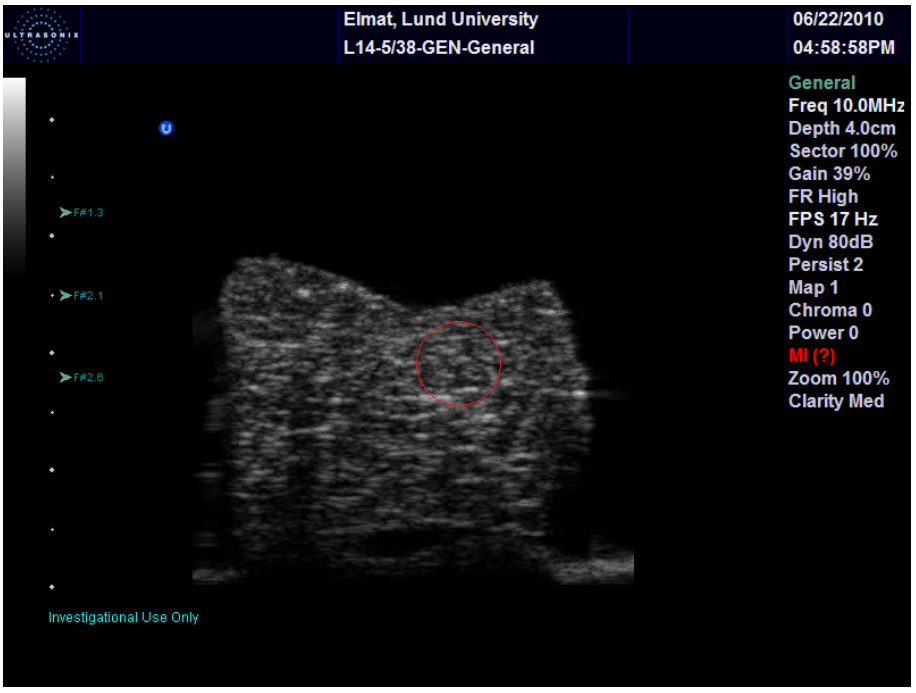

FIGURE 5.15: Ultrasonic image of a piece of porcine meat with a graphite rod inside. The position of the rod is shown by the red circle, even if the contrast is too low to reveal it.

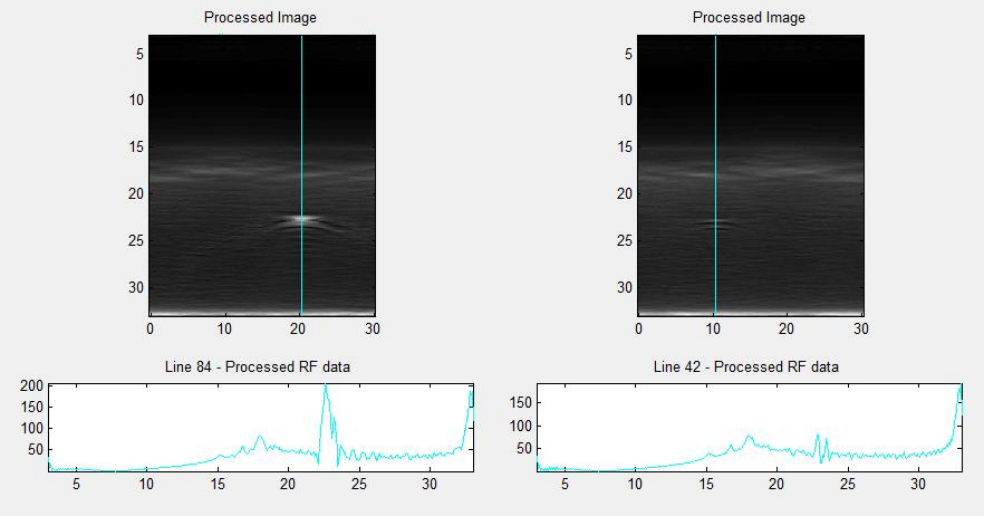

FIGURE 5.16: Processed photoacoustic images of a piece of porcine meat with a graphite rod inside. The left one corresponds to a distance of 10 *mm* between the rod and the illuminated surface, which corresponds to the right edge of the image. In the right one, instead, the distance is 20 *mm*.

The two photoacoustic images, instead, permit an easy localization of the inclusion. They can be seen in Figure 5.16. When the distance is 10 mm, the signal is quite strong and the SNR is 14 dB. In the second case, when the distance is 20 mm, the signal is still present, but it is very low and the SNR is 6 dB. This result confirms that the maximum depth for the target is about 2 cm for IR light. As the images testify, now the contrast is high enough to localize the target in the tissue.

Animal Tissue with Different Targets

The last performed experiment is made to test PAM selectivity, when biological tissues are used. The following components are employed to make the phantom: a glass capillary filled with blood, a small piece of Schott BG 39 filter, and some pieces of porcine meat, with width, depth, and height of 20 mm, 55 mm, and 8 mm respectively.

The blood capillary is identical to the one described in Section 5.3.3. It has an internal diameter of about 0.5 mm and an external one of about 1.5 mm. It is again filled with beef blood and sealed with soft blue rubber. It is used to test the photoacoustic emission that follows the absorption of green light at $\lambda = 532$ nm.

Since a material that does not absorb green light is needed, in order to measure the photoacoustic generation coming from the solely IR light absorption, a small piece of IR cutoff filter is used. It is of the same kind of the one, used to block the IR beam in the setup. It has the shape of an isosceles triangle with a base of 20 mm and a height of about 3 mm.

FIGURE 5.17: Photo of the blood capillary, of the filter fragment and of the porcine meat (on the left). Photo of the phantom made with them (on the right).

The phantom is assembled in the following way: at first, one piece of meat is overlaid on another; then, the blood capillary and the fragment of filter are placed at 5 mm and

10 *mm* from one edge of the meat, respectively; finally, another piece of meat is laid to surround them by tissue.

The components and the complete structure are shown in Figure 5.17. Note that, in order to increase the thickness of animal tissue, to be crossed by the photoacoustic waves before being detected, an additional layer of porcine meat, not shown in Figure 5.17, is added on top of the phantom. Then, everything is placed in water, using the usual bowl coated inside with black rubber.

At this point, two images of the sample are taken with the standard echography modality of the Sonix RP scanner. They are shown in Figure 5.18. The structure made by the four meat layers and the two targets can be seen very clearly.

Note that the blood capillary is placed at a depth of 24.3 *mm* from the transducer, while the filter fragment is at a depth of 25.4 *mm*. It is also possible to note that the thickness of the meat layer, above the targets, is of 18.7 *mm*.

Finally, two measurements are performed: in the first one, the sample is illuminated by IR light, while in the second one green light is used. The associated photoacoustic signals are collected and elaborated. The results are shown in Figure 5.19.

Looking at the processed image performed with IR light, it is possible to note that, on the right edge of the figure, there is a strong signal that abruptly stops after 5 *mm*. This corresponds to the IR laser light absorption by the water that surrounds the meat. This happens because the neutral density filter is not present in the setup and, consequently, the power is now high enough to let us see this weak absorption. As a matter of fact, the signal is made by two parallel lines, which correspond to a vertical section of the doughnut-shaped laser beam. At least, this phenomenon allows us to see where the meat surface is placed.

If we look deeper in the tissue, we can see two other signals, each of them made by two parallel surfaces. From their relative positions, it is possible to infer that the right one corresponds to the capillary surfaces, while the left one corresponds to the filter surfaces. Note that the filter signal is much stronger than the capillary one. Their SNR, indeed, are 13.2 dB and 8.7 dB, respectively. However, the signal associated to the capillary is unexpected, since the blood should not absorb the IR light. Looking at it closer, though, we can understand that it is not the blood that emits photoacoustic waves, otherwise the signal would be a single bright spot. It seams, instead, that the capillary glass walls absorb the laser light. Probably, this is also caused by some water that has filled the interstices between the capillary and the tissue. Otherwise, the signal could come from multiple reflections of the filter signal between the capillary glass walls. Indeed, these two targets are very close to each other.

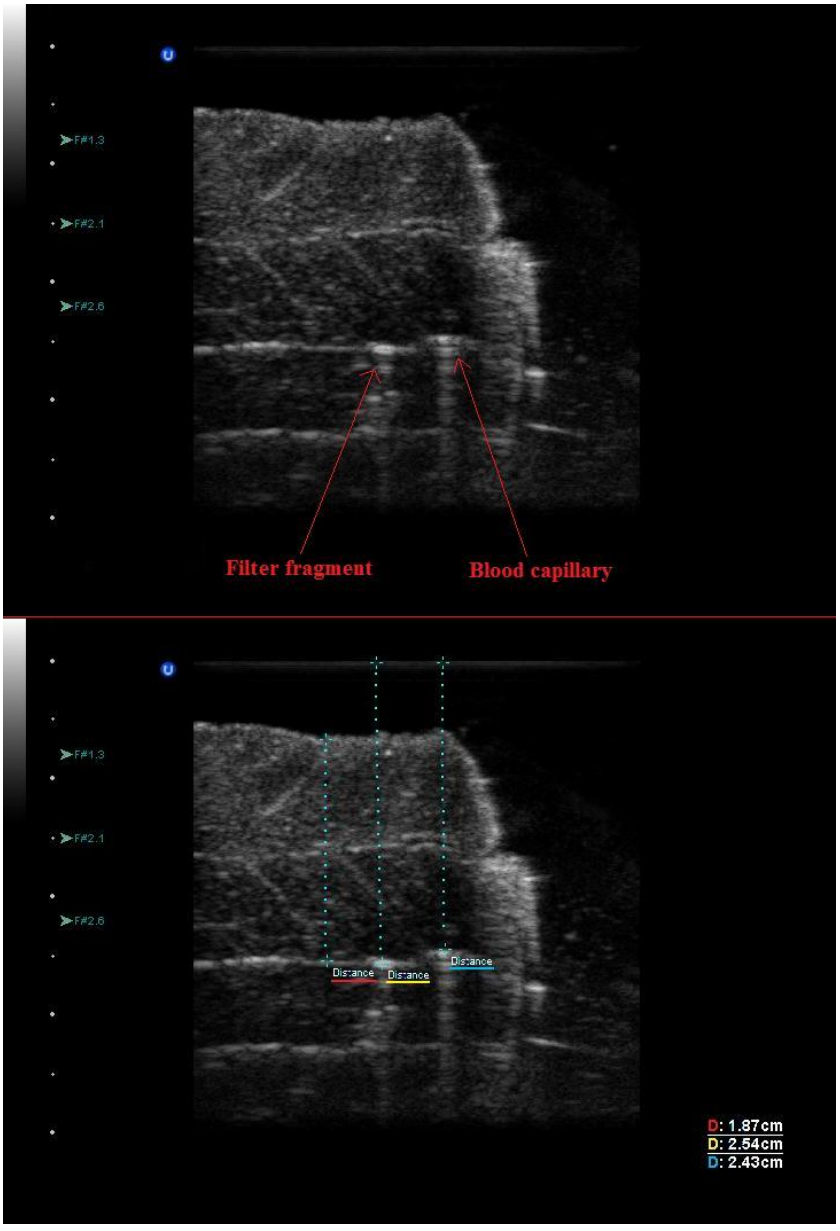

FIGURE 5.18: Ultrasonic images of the porcine meat with blood capillary and filter fragment inside. On top, there is the image without indication of distances to identify the targets. On the bottom, instead, main distances are indicated.

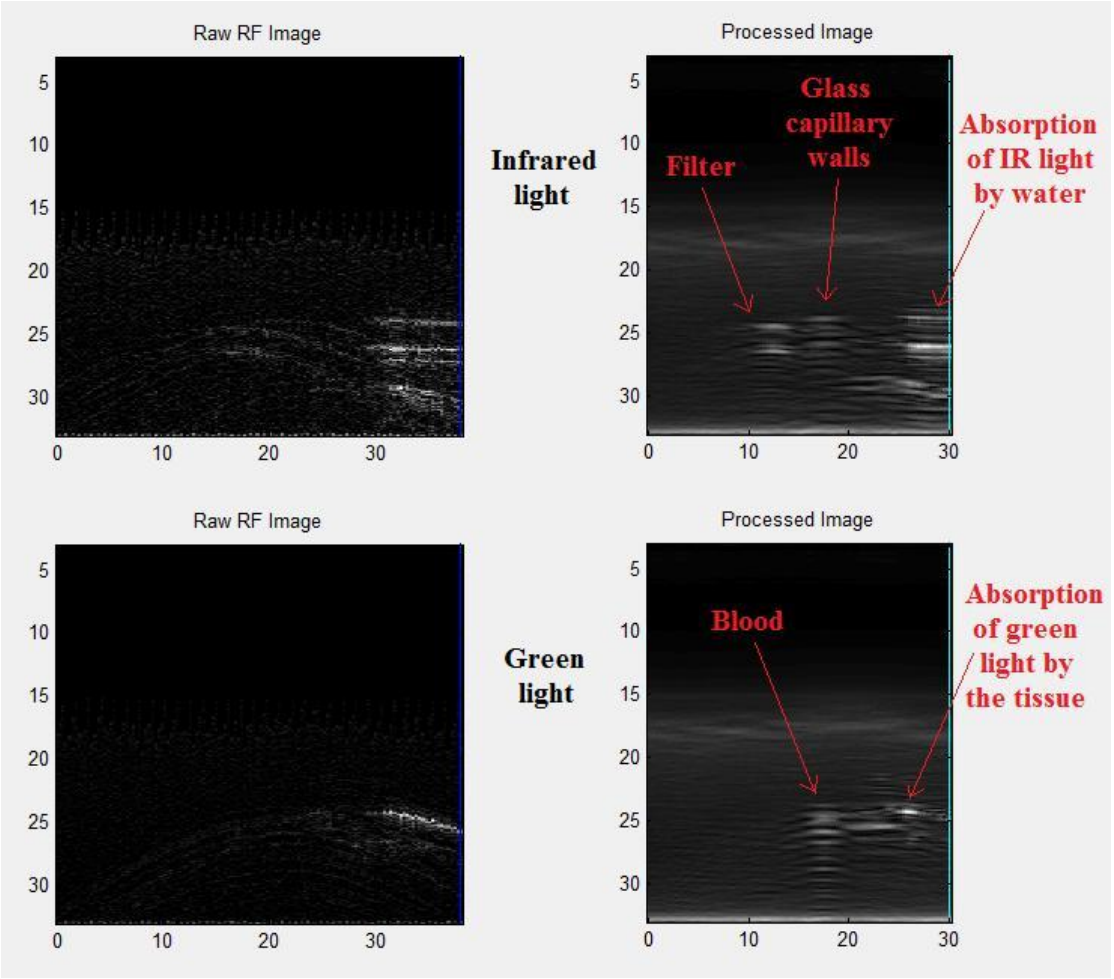

FIGURE 5.19: Photoacoustic images of the porcine meat with blood capillary and filter fragment inside, performed with IR light (top) and green light (bottom). Descriptions of the signals are also provided.

Consider now the image obtained by shedding green light. The problem is that the tissue itself greatly absorbs this wavelength. Indeed, an horizontal line, which corresponds to the laser beam path, is visible in the very first part of the tissue. This fact seems to happen especially at its surface, where a very bright spot is present. However, if we disregard this strong signal, we can note that there is another spot with $SNR = 10.9$ dB. This corresponds to blood absorption. Notice that the round spot associated to blood is enveloped by the two surfaces of the glass capillary, which also create the artifacts, due to the multiple reflection phenomenon, already mentioned in Section 5.3.3. Nevertheless, it is important to note that the filter is not visible anymore.

As clearly shown by these experiments, it is difficult to interpret photoacoustic images when tissues are employed, without previous knowledge of the structure to be imaged. This suggests that a combination of US and PAM is preferable. Moreover, green light can be only used to perform measurements of superficial blood vessels, because, due to

the absorption of light by the tissue itself, this wavelength cannot penetrate as much as the IR one.

However, the contrast between an IR absorber and pure blood seems to be very good. This justifies the use of gold nanoparticles as contrast agents, since their peak in absorption is about at $\lambda = 800\ nm$ [32], [41].

Chapter 6

Conclusions

6.1 Discussion of Results

The present thesis is a survey about the feasibility of a photoacoustic microscopy system, which employs a common commercial ultrasonic scanner for signal detection.

In the previous chapters, we have seen how the work has been carried out and the results of its characterization. In this concluding section, they will be discussed and compared to those obtained by other research groups.

6.1.1 Axial Resolution

Axial resolution, estimated in Section 5.3.1 as the FWHM of the signal coming from a point source, is less then 300 μm.

Park et al., in their article "Beamforming for photoacoustic imaging using linear array transducer", show that, for a similar setup, the signal coming from a 100 μm radius spherical absorber can be detected with a FWHM of about 400 μm [30]. As we can see, these two values are not so different.

Moreover, the axial resolution Δz can be calculated by the following formula [40]:

$$\Delta z \approx 0.88 \, \frac{v_s}{\Delta f}, \tag{6.1}$$

which shows that only the one-way acoustic bandwidth of the detector Δf plays a role in determining this value.

Knowing that the ultrasonic transducer, used in the present project, has a Δf of about 8 MHz [30], it results that:

$$\Delta z = 0.88 \frac{1540\ m/s}{8 \cdot 10^6\ \text{Hz}} \approx 0.2\ mm. \tag{6.2}$$

We can see that the experimental value is similar to the calculated one. This means that the setup is characterized by having an axial resolution which is close to the maximum theoretical limit.

6.1.2 Lateral Resolution

Lateral resolution, in contrast with the axial one, depends not only on the transducer frequency features, but also on the NA associated to the effective detector aperture, used for signal focusing.

Indeed, it can be expressed by the following formula [20]:

$$\Delta r \approx 0.71 \frac{\lambda_0}{\text{NA}} = 0.71 \frac{v_s}{f_0\,\text{NA}}, \tag{6.3}$$

where λ_0 is the central acoustic wavelength and f_0 is the central acoustic frequency of the transducer.

Since we use 32 elements for each scanline, that corresponds to a total aperture of $x = 9.8\ mm$, focusing at a representative depth of $D = 25\ mm$, we find that:

$$\theta = \arctan\left(\frac{x/2}{D}\right) = \arctan\left(\frac{4.9\ mm}{25\ mm}\right) = 0.1935\ rad, \tag{6.4}$$

$$\text{NA} = \sin\theta = \sin(0.1935\ rad) \simeq 0.2. \tag{6.5}$$

Substituting Eq. 6.5 into Eq. 6.3, knowing that $f_0 = 4$ MHz for our detector in listening mode [30], we obtain:

$$\Delta r = 0.71 \frac{1540\ m/s}{4 \cdot 10^6\,\text{Hz} * 0.2} \simeq 1.4\ mm. \tag{6.6}$$

As we can see, the result is in contrast with the experimental estimation of 4 mm. In fact, the measured lateral resolution is worse than what expected by, more or less, a factor of 3.

Even if, within the project, the solution of this problem has not been found yet. Probably, it is due to some errors hidden in the codes, that allow the Sonix RP scanner to collect the rough data from the transducer. Otherwise, it could be a problem of the transducer itself.

6.1.3 Temporal Resolution

As explained in Section 4.4.1, the temporal resolution of the developed system is of 0.08 $frames/sec$, which seems very low if compared to the state-of-the-art ones of about 50 $frames/sec$ (see Chapter 1). Nevertheless, it is necessary to note that our result is obtained with a laser PRF of 10 Hz, as the ANSI standards require, while the other groups have used PRFs of 1 kHz to speed up the measurement. With such a PRF, our temporal resolution would be of 8 $frames/sec$, which is one order of magnitude below the state-of-the-art level. This depends on the employed ultrasonic scanner, though, once the laser PRF as been chosen.

Unfortunately, with an actual temporal resolution of 0.08 $frames/sec$, one frame is realized in 12.5 s, which is a prohibitive time for real-time applications.

6.1.4 Contrast

We have seen that, in the performed experiments, the contrast between the target and the surrounding medium is usually high enough to distinguish them clearly.

However, since the used targets are very different from the real ones, it is not significant to compare their contrast values. Only in the last measurement, though, the contrast between bovine blood and porcine tissue can be calculated as:

$$C = \frac{I - I_b}{I_b} = \frac{130 - 40}{40} = 2.25, \tag{6.7}$$

where I is the target peak value and I_b is the background signal one. This result is very low if compared with the one found by Zhang et al., which is of 10 [15]. However, it strongly depends on the used excitation wavelenght, on the depth of the target and on the features of the transducer. As a result, it can greatly vary.

6.1.5 Signal-to-Noise Ratio

It is possible to infer, from the measurements in Section 5.3.3, that it is necessary to have an SNR higher than $\sim$6 dB in order to detect the signal distinctly. This depends

very much on the light amount that reaches the target and on the sensitivity of the transducer.

Although the detector used in the project was not developed for revealing photoacoustic signals, which are much smaller in magnitude than normal US pulses, they are still high enough to be measured. It happens even if the ANSI limit is respected: this is a great result.

6.1.6 Selectivity

Selectivity is a very important parameter of PAI systems. Indeed, it allows the discrimination of different targets. Within the project, two wavelengths, namely $\lambda = 1064\ nm$ and $\lambda = 532\ nm$, are used to detect IR absorbers and blood, respectively.

Selectivity is important because golden nanorods are often used to label cancer cells or to increase the target contrast in PAM [41]. Since these rods only absorb in the near-infrared spectrum of light, it can be useful to distinguish them from blood vessels, which can reveal some interesting information too, about the location of the cancer or the morphological structure of tissues.

The experiments made to test selectivity, in which the blood-filled capillary is employed, show that it is possible to see different targets separately. The drawback is that green light is not able to propagate in tissues as much as infrared radiation, which means that only superficial vessels can be clearly seen with PAI techniques.

6.2 Future Prospects

The summary presented in the previous section, about the characteristics of the developed PAM system, shows that there is still room for improvements.

First of all, the lateral resolution must be improved by understanding which is the problem that makes it so poor. This is a bad limitation, even if it could be solved by using more elements within one scanline and translating the transducer along its axis. As a consequence, the virtual aperture should allow a greater lateral resolution than the real one. The drawback consists in handling the translation with a slider and an appropriate code for elaboration. In addition, the temporal resolution would decrease.

Secondly, it could be helpful to change the setup by using a bundle of fiber optics to deliver light on the tissue surface. In this way it would be possible to place the fibers around the transducer, following a regular pattern, and to shed light on the same

surface of the ultrasonic investigation. As a result, it could be possible to think about real applications of the system, where it is not feasible to send the radiation laterally on the target. Moreover, this would homogenize the illumination, while avoiding the strong photoacoustic signal, that would arise from the direct surface irradiation under the transducer. The resulting device would be more compact and user friendly, without the need to align the system every time.

Thirdly, a necessary step to take, in order to image targets at different depths simultaneously, is to implement the dynamic focus in the beamforming elaboration code. The easier first version made, indeed, is only useful for the system characterization, where mainly one target at a time is employed.

In addition, it is important to see how the system behaves with a laser wavelength of about 800 nm. This radiation, as a matter of fact, should penetrate deeper into the tissue, increasing the relative spatial resolution (see Eq. 1.1 in Section 1.1), that is now limited by light attenuation in turbid biological media. At the moment, for $\lambda = 1064\, nm$, it is about 67, while it should be at least more than 100.

After these changes have been made to the setup, it is possible to think about real applications by using golden nanoparticles. They are usually employed to increase the contrast and the selectivity of PAM systems. Moreover, if real-time applications are needed, it is necessary to find a way to increase the temporal resolution, even if this mainly depends on the chosen ultrasonic scanner.

Appendix A

Texo Code for Sonix RP

This is the Texo code written in order to use the Sonix RP scanner in photoacoustic applications. It allows the user to choose the maximum depth of scanning and to save the data in the ".rf" format.

```
1  // This is a Texo program for recollecting photoacoustic data written
2  // by Luca Fieramonti - 15/04/2010
3  // The program is a recollection of instructions taken from the Texo
4  // Demonstration Program of Ultrasonix
5  // Medical Corporation (2007) edited by Tony de Souza-Daw
6  //
7  // Description: this program collects frames of single channel raw RF
8  // data without transmission and focusing.
9  // The scanlines are acquired according to the trigger signal.
10
11 // header files
12 #include <cstdio>
13 #include <cstdlib>
14 #include <conio.h>
15 #include <cstring>
16 #include <texo.h>
17 #include <texo_def.h>
18 #include <cmath>
19
20 using namespace std;
21
22 // constants
23 #define NUMCHANNELS         32
24 #define MAXELEMENTS         128
25 #ifndef DATA_PATH
26     #define DATA_PATH       "../../dat/"
27 #endif
```

```
28
29 // prototypes
30 bool selectProbe(int connector);
31 bool createSequence(int sequence);
32 bool run();
33 bool stop();
34 bool newImage(void *, unsigned char *, int);
35 bool sequenceSingleChannel();
36 void printStats();
37 bool saveData();
38 void wait();
39
40 // global variables
41 texo tex;
42 bool running = false;
43 bool validprobe = false;
44 bool validsequence = false;
45 int depth = 50;
46 /*Tony de S-D: make lineSize global to access it everywhere*/
47 int lineSize = 0;
48 int width = 0;
49 texoTransmitParams tx;
50 texoReceiveParams rx;
51 char selRF[4];
52
53 /* use the same header structure so it is compatible with the
54 *.rf files */
55 struct uFileHeader {
56 int type; // data type (can be determined by file extensions)
57 int frames; // number of frames in file
58 int w; // width (number of vectors for raw, image width for
59 //processed data)
60 int h; // height (number of samples for raw, image height
61 //for processed data)
62 int ss; // data sample size in bits
63 int ulx; // roi - upper left (x)
64 int uly; // roi - upper left (y)
65 int urx; // roi - upper right (x)
66 int ury; // roi - upper right (y)
67 int brx; // roi - bottom right (x)
68 int bry; // roi - bottom right (y)
69 int blx; // roi - bottom left (x)
70 int bly; // roi - bottom left (y)
71 int probe; // probe identifier - additional probe information
72 //can be found using this id
73 int txf; // transmit frequency in Hz
74 int sf; // sampling frequency in Hz
75 int dr; // data rate (fps or prp in Doppler modes)
```

```
76 int ld; // line density (can be used to calculate element
77 //spacing if pitch and native # elements is known
78 int extra; // extra information (ensemble for color RF)
79 };
80 // program entry point
81 int main()
82 {
83         char sel;
84     // initialize and set the data file path
85     if(!tex.init(DATA_PATH, 2, 2, 0, 0, 0))
86         return -1;
87     // set the new frame callback
88     tex.setCallback(newImage, 0);
89     // initialize global parameters
90     tex.setPower(0, 0, 0); // To be sure the transducer
91                                // is not transmitting!
92     tex.addTGC(1.00);      // Flat gain
93         tex.setSyncSignals(1, 0, 0);  // This adds the trigger
94                                // input signal for each scanline!
95
96                 printf("make a selection:\n");
97         printf("\n");
98         printf("(1) select probe connector 1\n");
99         printf("(2) select probe connector 2\n");
100        printf("(3) select probe connector 3\n");
101        printf("\n");
102        scanf("%c", &sel);
103                switch(sel)
104                {
105                        case '1': selectProbe(0); break;
106                        case '2': selectProbe(1); break;
107                        case '3': selectProbe(2); break;
108                }
109                wait();
110                createSequence();// load the single channel sequence
111                wait();
112                for(;;)
113    {
114        printf("make a selection:\n");
115        printf("\n");
116                printf("(R) run sequence\n");
117        printf("(S) stop sequence\n");
118        printf("\n");
119        printf("(D) store data to disk\n");
120        printf("(X) exit\n");
121        printf("\n");
122        scanf("%c", &sel);
123       switch(sel)
```

```
124         {
125                         case 'r': case 'R': run(); break;
126             case 's': case 'S': stop(); break;
127             case 'd': case 'D': saveData(); break;
128             case 'x': case 'X': goto goodbye;
129         }
130         wait();
131     }
132 goodbye:
133     if(running)
134         stop();
135     // clean up
136     tex.shutdown();
137         return 0;
138 }
139 
140 void wait()
141 {
142     printf("\npress any key to continue");
143     while(!kbhit());
144     getch();
145     fflush(stdin);
146     system("cls");
147 }
148 
149 // statistics printout for after sequence has been loaded
150 void printStats()
151 {
152     // print out sequence statistics
153 printf("sequence for single channel RF data aquisition loaded\n");
154 printf("sequence statistics:\n");
155 printf("frame size = %d bytes\n", tex.getFrameSize());
156 printf("frame rate= %.1f fr/sec\n", tex.getFrameRate());
157 printf("buffer size = %d frames\n\n", tex.getMaxFrameCount());
158 }
159 
160 // selects a probe, the function will fail if the connector
161 // is invalid or if there is no probe on the specified connector.
162 bool selectProbe(int connector)
163 {
164     if(!tex.activateProbeConnector(connector))
165     {
166         connector++;
167 fprintf(stderr, "could not activate connector %d\n", connector);
168         return false;
169     }
170         connector++;
171         printf("probe connector n. %d activated\n", connector);
```

```
172     validprobe = true;
173     return true;
174 }
175 
176 // runs a sequence
177 bool run()
178 {
179     if(!validsequence)
180     {
181         fprintf(stderr, "cannot run, no sequence loaded\n");
182         return false;
183     }
184     if(running)
185     {
186         fprintf(stderr, "sequence is already running\n");
187         return false;
188     }
189     if(tex.runImage())
190     {
191         running = true;
192         return true;
193     }
194      return false;
195 }
196 
197 // stops a sequence from running
198 bool stop()
199 {
200     if(!running)
201     {
202 fprintf(stderr, "nothing to stop, sequence is not running\n");
203         return false;
204     }
205     if(tex.stopImage())
206     {
207         running = false;
208 fprintf(stdout, "acquired (%d) frames\n", tex.getCollectedFrameCount());
209         return true;
210     }
211     return false;
212 }
213 
214 bool createSequence()
215 {
216     if(!validprobe)
217     {
218   fprintf(stderr, "cannot create sequence, no probe selected\n");
219         return false;
```

```
220     }
221
222     printf("enter desired depth in mm (10 - 300):\n");
223     scanf("%d", &depth);
224     if(depth < 10 || depth > 300)
225     {
226         fprintf(stderr, "invalid depth entered\n");
227         return false;
228     }
229     // tell program to initialize for new sequence
230     if(!tex.beginSequence())
231         return false;
232     // build sequence
233         if(!sequenceSingleChannel())
234                 return false;
235         // tell program to finish sequence
236     if(tex.endSequence() == -1)
237         return false;
238    printStats();
239     validsequence = true;
240         return true;
241 }
242
243 // transmits and receives across the entire probe to acquire
244 // single channel RF data (full transmit still)
245 bool sequenceSingleChannel()
246 {
247     int i;
248         int j;
249
250     tx.centerElement = 0;
251     tx.aperture = 64;
252     tx.focusDistance = 30000;
253     tx.angle = 0;
254     tx.frequency = tex.getProbeCenterFreq();
255     strcpy(tx.pulseShape, "00"); // Zero pulse shape!
256     tx.speedOfSound = 1540*2;    // Added scaling factor!
257     tx.useManualDelays = false;
258     tx.tableIndex = -1;
259     tx.useDeadElements = false;
260     tx.trex = false;
261
262     rx.centerElement = 0;
263     rx.aperture = 32;
264     rx.angle = 0;
265     rx.maxApertureDepth = 30000;
266     rx.acquisitionDepth = depth * 1000;
267     rx.saveDelay = 0;
```

```
268     rx.speedOfSound = 1540*2;
269     rx.channelMask[0] = rx.channelMask[1] = 0xFFFFFFFF;
270     rx.applyFocus = false;
271     rx.useManualDelays = false;
272     rx.decimation = 1;
273     rx.customLineDuration = 0;
274     rx.lgcValue = 0;
275     rx.tgcSel = 0;
276     rx.tableIndex = -1;
277 
278         width = tex.getProbeNumElements();
279 
280         for(i = 0; i < tex.getProbeNumElements(); i++)
281           {
282  // add 5 to the virtual element, to make symettrical time delays
283  // we should do this because the aperture values must be even
284         tx.centerElement = (i * 10) + 5;
285         rx.centerElement = (i * 10) + 5;
286 
287         // ** for single channel receive **
288         rx.channelMask[0] = 1 << (j % 32);
289 // Adds the scanlines to the sequence. It will be started by
290 //the 'run' function.
291         lineSize = tex.addLine(rfData, tx, rx);
292 
293         if(lineSize == -1)
294             return false;
295       }
296         return true;
297 }
298 
299 // store data to disk
300 bool saveData()
301 {
302     char path[100];
303     int numFrames, frameSize;
304     FILE * fp;
305 
306         //Tony de S-D: Save data with Frame Info.
307 /*RF DATA HEADER FROM THE USER MANUAL (SOFTWARE PACKAGE OUTPUTS)*/
308         uFileHeader h;
309         h.type = 0;
310         h.frames = tex.getCollectedFrameCount();
311         h.ss = 16; /*always 16 bits */
312         h.ulx = 0;
313         h.uly = 0;
314         h.urx = 0;
315         h.ury = 0;
```

```
316         h.brx = 0;
317         h.bry = 0;
318         h.blx = 0;
319         h.bly = 0;
320         h.probe = 0;
321         h.txf = tx.frequency; /*in Hz*/
322         h.sf = 40000000/(1+rx.decimation);
323         h.dr = (int) tex.getFrameRate(); /*in fps*/
324         h.ld = 256;
325         /*Debug*/
326         h.extra = lineSize;
327         numFrames = tex.getCollectedFrameCount();
328     frameSize = tex.getFrameSize();
329         if(numFrames < 1)
330     {
331         fprintf(stderr, "no frames have been acquired\n");
332         return false;
333     }
334         /*in case of division of zero, if no frames. Put here.*/
335         h.h = lineSize/2; /*the data is 16 bits depth, 2 bytes.*/
336         h.w = width;
337         printf("height: %d   width: %d\n", h.h, h.w);
338     printf("enter a filename: ");
339     scanf("%s", path);
340         /*add the .rf to the filename*/
341         strcat(path, ".rf");
342     fp = fopen(path, "wb+");
343     if(!fp)
344     {
345         fprintf(stderr, "could not store data to specified path\n");
346         return false;
347     }
348         //write header
349         fwrite(&h, sizeof(h), 1, fp);
350         //write cine loop
351     fwrite(tex.getCineStart(), frameSize, numFrames, fp);
352     fclose(fp);
353     fprintf(stdout, "successfully stored data\n");
354     return true;
355 }
```

Appendix B

Matlab Code for Beamforming the Photoacoustic Signals

This is the Matlab *"beamforming"* function written in order to use the Ultrasonix *"GraphicUnit_export"* GUI for displaying photoacoustic focused signals. The input parameters are the "RF" matrix, that contains the raw RF data, and the desired focus distance "R" in millimetres. The function returns a new matrix with the beamformed and apodized data that can be directly displayed with the GUI.

```
1  function A = beamforming (RF, R)
2  %
3  %beamforming: Reads an image as a matrix (RF) and return the beamformed
4  %image with fixed focus (R). Works properly with depth=30 mm.
5  %
6  %19/04/2010 - Luca Fieramonti
7  %
8  [h,w] = size(RF);
9  R=20; %desired focal distance in mm. Comment this line if you want to
10 %choose the focal distance from outside the function.
11 R1=R*1000; %conversion to microns
12 x=304.8;%distance between the centers of two adiacent elements in microns
13 x1=x/2; %virtual distance of the first pixel from the center of the
14 %transducer in microns
15 d=zeros(1,16); %empty delay vector
16
17 A=zeros(h,97); %empty matrix of dimensions h*97
18 u=ones(h,1);
19 e=ones(32,1);
20 k=(hanning(32))'; %row hanning vector
21 K=u*k; %matrix for apodization
22
```

```
for n=0:15 %cicle for creating the array d of delays
    xn=x1+n*x; %actual element displacement
    d(n+1)=R1*((sqrt(R1^2+xn^2)/R1)-1); %delay in microns from the
    %central element to the last element in the right
end
d=d./77; %delay conversion to pixels
d=int16(d); % to round the numbers to the nearest integer in order to
%describe pixels

for j=0:96 %main cicle in which, at the end, the beamformed scanline is
    %stored in matrix A
    B=RF(:,(1+j):(32+j)); %submatrix with 32 channels
    C=slideMatrixElements(B, d, h); %see the declaration of this
    %function below
    F=C.*K; %apodization
    p=F*e; %actual column of the final image.
    A(:,(j+1))=p; %write the vector in the right position of matrix A
end

%%%%%%%%%%%%%% function to be used in the principal function %%%%%%%%%%

function M=slideMatrixElements(B, d, h)
%
%slideMatrixElements: Applies the delay to the columns of B matrix
%according to vector d
%
%
for i=0:15       %cicle to scan the columns
    r=d(16-i);

    for l=0:(h-1)    %cicle to scan the elements in a column

        if (1+r+l)<=h % actual sliding of elements
            B(1+l, 1+i)=B(1+r+l, 1+i);
            B(1+l, 32-i)=B(1+r+l, 32-i);
        else    % do this if the edge of matrix B is reached
            B(1+l, 1+i)=0;
            B(1+l, 32-i)=0;
        end

    end

end
M=B;
```

Acknowledgements

First of all, I would like to thank prof. Rinaldo Cubeddu for helping me finding a project abroad about biomedical optics and for his advice about the thesis. With him, I would like to thank prof. Stefan Andersson-Engels for letting me work on the photoacoustic project at Lund University.

I would also acknowledge the enthusiastic help that prof. Magnus Cinthio and prof. Tomas Jansson gave to me with the Sonix RP scanner, the transducers and all the ultrasonic equipment. You were always available to discuss about my doubts and to teach me a lot of interesting things.

A special thanks to Pontus Svenmarker for his help in the optical lab and for reading the thesis so carefully. Your comments have been very important for me.

I have really appreciated the private lecture of prof. Andrea Bassi about ultrasounds just before the start of my erasmus and his disponibility to answer all my questions about the PhD course. I am sure that your help has been determining for my future career.

I would also thank Maria Holst for helping me in the very beginning of my experience in Lund University, Tobias Nilsson for his Matlab hints and Maria Ewerlöf for having been so friendly to me. I enjoyed so much having lunches with you. Together with all students and professors of the Electrical Measurements Department, you created a beautiful environment in which to work.

A particular thanks to prof. Anders Persson, for his help with the Nd:YAG laser, to my opponent Shazia Farooq Enayat, for reading the whole thesis and for her questions about it, and to students and professors of the Atomic Physics Department for their disponibility.

Outside the university, I feel the need to thank a lot of people who have contributed to make my erasmus experience unforgettable. First of all, I would like very much to thank Pamela Buratti and Andrea Frecassetti for being true friends and for having lead me into Lund party life. Thanks also to Michele Giunta for our coffee breaks.

I would also thank Kelly Delaney and Stanisław Wosicki for making the corridor a better and more joyful place to live in.

A special thank to all the Gudrun choir guys and, in particular, to Angela Contri and Andrea Cavalli.

Vorrei ringraziare, infine, tutti i parenti e gli amici di sempre che, nonostante la lontananza, ho sentito comunque molto vicini.

Un grazie ai miei genitori per tutto il sostegno che mi hanno dato e per i sacrifici fatti per permettermi di allargare i miei orizzonti.

Grazie a Sara e Lorenzo, ai nonni, agli zii e cugini, alla zia Mariuccia e a tutti i parenti per essere sempre stati presenti ed avermi mostrato il loro affetto.

Grazie anche alla famiglia Fontolan, per avermi sempre trattato come un membro della famiglia, per le fantastiche cene e per l'incoraggiamento.

Grazie a tutti gli amici del CDV per le emozioni che sono riusciti a farmi vivere con la loro musica, nonostante i 1500 chilometri di distanza.

Grazie a Luca per avermi accompagnato nei primi giorni della mia avventura e a Giuseppe ed Andrea per le serate passate insieme.

Grazie ad Alessandra, Chiara, Francesca, Lucia, Selena, Federico, Flavio, Luca, Matteo e Riccardo per la loro preziosa amicizia e per condividere con me bellissime esperienze.

Infine, un ringraziamento speciale va alla mia ragazza Stefania. Durante tutti i mesi dell'erasmus sei sempre stata presente con il tuo affetto e il tuo sostegno morale. Senza la tua comprensione sarebbe stato difficile sopportare la lontananza. Grazie per aver letto con molta pazienza tutta la tesi e per aver corretto i miei frequenti errori di grammatica inglese. Grazie per esserti presa cura di me durante l'operazione chirurgica e la convalescenza, trasformandoti in infermiera ed ottima cuoca. Grazie per rendermi ogni giorno una persona migliore. Se con questo lavoro ho raggiunto un qualche tipo di traguardo, lo devo in gran parte a te.

Bibliography

[1] P.C. Beard, E.Z. Zhang, and J.G. Laufer, "3D photoacoustic scanner based on an optical ultrasound-mapping system for imaging superficial vascular anatomy in vivo", in *Photoacoustic imaging and spectroscopy*, L.V. Wang, 2009, pp. 209-222, (CRC press, New York, NY).

[2] M. Xu, and L.V. Wang, "Photoacoustic imaging in biomedicine", *Rev. Sci. Instum.*, Vol. 77, No. 4, 041101, (2006).

[3] C. Li, and L.V. Wang, "Photoacoustic tomography and sensing in biomedicine", *Phys. Med. Biol.*, Vol. 54, No. 19, R59-R97, (2009).

[4] Y. Sun, E. Sobel, and H. Jiang, "Three-Dimensional quantitative photoacoustic tomography of osteoarthritis: initial clinical results in the finger joints", in *Digital Holography and Three-Dimensional Imaging*, OSA Technical Digest (CD) (Optical Society of America, April 11, 2010), paper JMA50.

[5] L.V. Wang, "Photoacoustic tomography and microscopy", *OPN*, Vol. 19, No. 7, 36-41, (2008).

[6] L.V. Wang, and H. Wu, "Photoacoustic tomography", in *Biomedical optics: principles and imaging*, L.V. Wang, 2007, cap. 12, pp. 283-321, (Wiley & Sons, Hoboken, NJ).

[7] Z. Guo, L. Li, and L.V. Wang, "On the speckle-free nature of photoacoustic tomography", *Med. Phys.*, Vol. 36, No. 9, 4084, (2009).

[8] L.V. Wang, "Tutorial on photoacoustic microscopy and computed tomography", *IEEE Journal of selected topics in quantum electronics*, Vol. 14, No. 1, January/February, (2008).

[9] J.C. Ranasinghesagara, H. Lu, K.W. Mathewson, T. Harrison, and R.J. Zemp, "Dual-mode Fast Scanning Ultrasound-Photoacoustic System for Preclinical Molecular Imaging", in *Advances in Ultrasonic Imaging and Drug Delivery*, (Montreal, CND), paper 0106, (2009). URL `http://www.wmicmeeting.org/abstracts/data/papers/0106.html`.

[10] A.G. Bell, "On the production and reproduction of sound by light", *Am. J. Sci.*, Vol. 20, No. 118, 305-324, (1880).

[11] M. Xu, and L.V. Wang, "Universal back-projection algorithm for photoacoustic tomography", in *Photoacoustic imaging and spectroscopy*, L.V. Wang, 2009, pp. 37-46, (CRC press, New York, NY).

[12] M. Li, J.T. Oh, X. Xie, G. Ku, W. Wang, C. Li, G. Lungu, G. Stoica, and L.V. Wang, "Simultaneous molecular and hypoxia imaging of brain tumors in vivo using spectroscopic photoacoustic tomography", in *Proc. of IEEE*, Vol. 96, No. 3, 481-489, (2008).

[13] C. Li, A. Aguirre, J. Gamelin, A. Maurudis, Q. Zhu, and L.V. Wang, "Real-time photoacoustic tomography of cortical hemodynamics in small animals", *J. Biomed. Opt.*, Vol. 15, 010509, (2010).

[14] H.Z. Zhang, K. Maslov, and L.V. Wang, "Dark-field confocal photoacoustic microscopy", in *Photoacoustic imaging and spectroscopy*, L.V. Wang, 2009, pp. 267-280, (CRC press, New York, NY).

[15] H.F. Zhang, K. Maslov, and L.V. Wang, "In vivo imaging of subcutaneous structures using functional photoacoustic microscopy", *Nature Protocols*, Vol. 2, 797-804, (2007).

[16] L. Song, K. Maslov, and L.V. Wang, "Section-illumination photoacoustic microscopy for dynamic 3D imaging of microcirculation in vivo", *Optics Letters*, Vol. 35, No. 9, 1482-1484, (2010).

[17] K.H. Song, and L.V. Wang, "Deep reflection-mode photoacoustic imaging of biological tissue", *J. Biomed. Opt.*, Vol. 12, 060503, (2007).

[18] OptoSonics Inc., "Human applications", (2010), URL `http://optosonics.com/human-applications.html`.

[19] L.V. Wang, "Microwave-induced acoustic (thermoacoustic) tomography", in *Photoacoustic imaging and spectroscopy*, L.V. Wang, 2009, pp. 339-347, (CRC press, New York, NY).

[20] L.V. Wang, slides from conference "Photoacoustic Tomography: Breaking through the Optical Diffusion Limit", presented in *Inverse Transport Theory and Tomography* at Banff International Research Station (BIRS), Banff AB, Canada, on 5/17/2010. URL `http://labs.seas.wustl.edu/bme/Wang/presentations.html`.

[21] J.M. Yang, K. Maslov, H.C. Yang, Q. Zhou, K.K. Shung, and L.V. Wang, "Photoacoustic endoscopy", *Optics Letters*, Vol. 34, No. 10, 1591-1593, (2009).

[22] L.V. Wang, and H. Wu, "Introduction", in *Biomedical optics: principles and imaging*, L.V. Wang, 2007, cap. 1, pp. 1-15, (Wiley & Sons, Hoboken, NJ).

[23] L.V. Wang, and H. Wu, "Radiative transfer equation and diffusion theory", in *Biomedical optics: principles and imaging*, L.V. Wang, 2007, cap. 5, pp. 83-118, (Wiley & Sons, Hoboken, NJ).

[24] L.V. Wang, and H. Wu, "Rayleigh theory and Mie theory for a single scatterer", in *Biomedical optics: principles and imaging*, L.V. Wang, 2007, cap. 2, pp. 17-35, (Wiley & Sons, Hoboken, NJ).

[25] R. Cubeddu, Politecnico di Milano, Italy, (2008), (private handouts).

[26] T. Spott, and L.O. Svaasand, "Collimated light sources in the diffusion approximation", *Appl. Opt.*, Vol. 39, No. 34, 6453-6465, (2000).

[27] T. Jansson, Electrical Measurements Department, Lund University, (2010), (private discussion).

[28] B. Cox, and P.C. Beard, "Modeling photoacoustic propagation in tissue using k-space techniques", in *Photoacoustic imaging and spectroscopy*, L.V. Wang, 2009, pp. 289-297, (CRC press, New York, NY).

[29] G.J. Diebold, "Photoacoustic monopole radiation: waves from objects with symmetry in one, two, and three dimensions", in *Photoacoustic imaging and spectroscopy*, L.V. Wang, 2009, pp. 3-17, (CRC press, New York, NY).

[30] S. Park, S.R. Aglyamov, and S.Y. Emelianov, "Beamforming for photoacoustic imaging using linear array transducer", in *IEEE Ultrasonics Symposium*, 2007, 856-859, (New York, NY).

[31] M. Jaeger, and M. Frenz, "Combined ultrasound and photoacoustic system for real-time high-contrast imaging using a linear array transducer", in *Photoacoustic imaging and spectroscopy*, L.V. Wang, 2009, pp. 289-297, (CRC press, New York, NY).

[32] S. Mallidi, P.P. Joshi, K. Sokolov, and S. Emelianov, "On sensitivity of molecular specific photoacoustic imaging using plasmonic gold nanoparticles", in *Engineering in Medicine and Biology Society, 2009. EMBC 2009. Annual International Conference of the IEEE*, 3-6 September 2009, 6338-6340, (Minneapolis, MN).

[33] Ultrasonix Medical Corporation, "SONIX service manual", 2006, (Burnaby, DC Canada). URL `http://www.ultrasonix.com`.

[34] R.J. Zemp, L. Song, R. Bitton, K.K. Shung, and L.V. Wang, "Realtime photoacoustic microscopy in vivo with a 30-MHz ultrasound array transducer", *Opt. Expr.*, Vol. 16, No. 11, 7915-7928, (2008).

[35] Ultrasonix Medical Corporation, "Texo SDK Guide". URL `http://ultrasonix.com/wikisonix/index.php?title=Texo`.

[36] Ultrasonix Medical Corporation, "Sonix RP Guide". URL `http://ultrasonix.com/wikisonix/index.php?title=Working_with_Data#Coding_Information`.

[37] I. Driver, J.W. Feather, P.R. King, and J.B. Dawson, "The optical properties of aqueous suspensions of Intralipid, a fat emulsion", *Phys. Med. Biol.*, Vol. 34, No. 12, 1927-1930, (1989).

[38] J.O. Smith, "Mathematics of the Discrete Fourier Transform (DFT) with Audio Applications", second edition, online book, (2007). URL `https://ccrma.stanford.edu/~jos/r320/Analytic_Signals_Hilbert_Transform.html`.

[39] Y. Xu, L.V. Wang, G. Ambartsoumian, and P. Kuchment, "Limited view thermoacoustic tomography", in *Photoacoustic imaging and spectroscopy*, L.V. Wang, 2009, pp. 61-73, (CRC press, New York, NY).

[40] M. Xu, and L.V. Wang, "Analysis of spatial resolution in photoacoustic tomography", in *Photoacoustic imaging and spectroscopy*, L.V. Wang, 2009, pp. 47-60, (CRC press, New York, NY).

[41] A. Agarwal, S.W. Huang, M. O'Donnell, K.C. Day, M. Day, N. Kotov, and S. Ashkenazi, "Targeted gold nanorod contrast agent for prostate cancer detection by photoacoustic imaging", *J. Appl. Phys.*, Vol. 102, 064701(1-4), (2007).